University of Rhode Island
DigitalCommons@URI

SURFO Technical Reports | Graduate School of Oceanography

2004

SURFO Technical Report No. 2005-01

SURFO

Follow this and additional works at: http://digitalcommons.uri.edu/surfo_tech_reports

Recommended Citation
SURFO, "SURFO Technical Report No. 2005-01" (2004). *SURFO Technical Reports.* Paper 8.
http://digitalcommons.uri.edu/surfo_tech_reports/8

This Periodical is brought to you for free and open access by the Graduate School of Oceanography at DigitalCommons@URI. It has been accepted for inclusion in SURFO Technical Reports by an authorized administrator of DigitalCommons@URI. For more information, please contact digitalcommons@etal.uri.edu.

Papers from
the

SUMMER UNDERGRADUATE RESEARCH FELLOWSHIP PROGRAM IN OCEANOGRAPHY

at

THE UNIVERSITY OF RHODE ISLAND
Graduate School of Oceanography
and
Department of Ocean Engineering

NARRAGANSETT, RHODE ISLAND

June - August 2004

This program was funded by Grant OCE-0243794 from the National Science Foundation.

GSO Technical Report No. 2005-01

PARTICIPANTS IN THE 2004 SUMMER UNDERGRADUATE RESEARCH FELLOWSHIP PROGRAM IN OCEANOGRAPHY

FELLOWS

Katherine Banahan	Fairfield University, Fairfield, CT
Daniel Dean	Gonzaga University, Spokane, WA
Kelly Hanks	University of Rhode Island, Kingston, RI
Kristofer Karlson	Worcester Polytechnical Institute, Worcester, MA
Sam Kelly	Carleton College, Northfield, MN
John Mischler	Augustana College, Rock Island, IL
Sean Poche	University of New Orleans, New Orleans, LA
Rachelle Richmond	University of California, Davis, CA
Lori Schultz	Austin Peay University, Clarksville, TN
Maya Stevens	California PolytechnicUniversity, San Luis Obispo, CA
Xaymara Serrano	University of Puerto Rico, Rio Pedras, PR

ADVISORS

Jeremy Collie
Isaac Ginis
Alfred Hanson
John Merrill
Robert Pockalny
Tom Rossby
Yang Shen
David C. Smith
Art Spivack

PROGRAM ASSISTANTS

Rich Viso, Kim Carey & Rhonda Kenny

PREFACE

This report presents the papers written by the 11 participants in the 2004 Summer Undergraduate Research Fellowships in Oceanography (SURFO) program at the Graduate School of Oceanography (GSO), University of Rhode Island (URI). This past summer represented the 19th year in which the program has been coordinated and extended through the several disciplines in oceanography and ocean engineering at URI's Narragansett Bay Campus. The 2004 program continued excellence beyond the official duration of the program with at least one project resulting in a manuscript to be submitted for publication. In addition, five presentations were made at national meetings, including AGU and ASLO.

During the fall of 2003 advertisements were sent to physics, chemistry, biology and geology departments, including faculty advisors at a number of minority colleges.. Flyers and overheads were provided to colleagues presenting invited talks at various undergraduate institutions. The SURFO web site has continued to be updated and more useful links describing possible research programs at GSO/URI have been added. We received 76 applications for the program, and about two-thirds of these applicants used the electronic application form. This represents the third consecutive year that about two-thirds of thestudetns have used the SURFO website to apply electronically. Eleven students were selected for the program with a breakdown by oceanographic discipline as follows: 2 Geological, 3 Physical, 2 Chemical, 2 Biological, 2 Astrobiological. The gender break-down returned to a female majority (6 female, 5 male) and two participants were from under-represented groups in science.

The timeline of the 11-week program was adjusted slightly this year to provide students with an extended orientation period during the first two weeks. This orientation period began with a breakfast to welcome the new students and introduce them to the GSO campus community, and was followed by a tour of the campus and facilities. For the next 5 work days, daily background/introductory seminars were presented by graduate students from the various sub-disciplines of oceanography, including: biological oceanography, marine and atmospheric chemistry, marine geology & geophysics, physical oceanography, and ocean engineering. A cruise on the Narragansett Bay to introduce students to oceanographic tools and several team-building workshops were also held during the first two weeks. During the remainder of the program weekly seminars (on Tuesdays) on “hot topics” in oceanography were presented by a GSO faculty member or marine scientist. On Thursdays of each week, a professional development workshop or discussion was held to round-out the students experience. Topics such as “learning/research styles”, “scientific writing and effective presentations”, and “hands-on modeling methods” were provided..

We continued an informal round-table meeting with several faculty members, graduate students and SURFOs to discuss how to get into graduate school and what will be expected of them. We also instituted a similar round-table format to discuss possible careers in oceanography. Our exit questionnaires revealed that students found these seminars interesting and very useful, and the exposure to a wide range of disciplines/research topics helped students identify additional areas of interest. Other undergraduates (NOT affiliated with the SURFO program) working at EPA or NOAA labs on the Bay Campus and even graduate students at GSO also attend many of these seminars.

Included in the summer events was our annual day of kayaking on the Narrow River, led by Bob Sand, to investigate the flora and fauna of an estuary. A subset of SURFOs also participated in a series of field days funded by other projects where water sampling and fish trawls were made at several locations in Narragansett Bay and Rhode Island Sound. We also continued with our tradition of having an informal noon-time barbecue each Friday for the SURFOs on the veranda at the Horn Lab. This provided the SURFOs with a taste of graduate-student life in an informal setting where they were able to meet with GSO faculty, graduate students and staff. The annual SURFOs vs ADVISORS softball game was won by the advisors, and continued the advisors undefeated streak.

One measure of success of our program is if fellows continue on with graduate studies in science and, specifically, in oceanography or ocean engineering. The exit questionnaire and follow-up conversations indicate that 10 of 11 the students definitely plan to continue on with graduate studies in science/engineering. Of these, 6 said they are seriously considering oceanography. Three of the students have applied to GSO for the fall 2005 semester.

The participants in the 2004 SURFO program are grateful to the National Science Foundation for its support of the program through grant OCE-0243794. The NASA Astrobiological Institute at GSO/URI (Steve D'Hondt, David Smith and Art Spivack) also provide supplemental funds for Kelly Hanks and Kristofer Karlson. The SURFO participants and I would like to thank all of those individuals at URI who contributed to the program's success including those who advised the students and who gave SURFO seminar presentations. In addition, our thanks to Rhonda Kenny and Kim Carey for their assistance in the preparation of this report as well as the administrative, financial and recruitment tasks. Finally, we would like to thank Rich Viso who served as a graduate coordinator for the program, Friends of Oceanography for providing seminar refreshments, and Bob Sand for running the kayak trip.

Robert A. Pockalny
SURFO Site Director

TABLE OF CONTENTS

Resource partitioning between four species of flounder in Narragansett Bay

Kathryn Banahan,[1] and Jeremy Collie

Graduate School of Oceanography, University of Rhode Island, Narragansett, Rhode Island

Abstract. In this study, we investigated the diets of four species of flounder in Narragansett Bay: summer flounder (*Paralichthys dentatus*), winter flounder (*Pseudopleuronectes americanus*), fourspot flounder (*Paralichthys oblongus*), and windowpane flounder (*Scophthalmus aquosus*). These four species are abundant in Narragansett Bay during the summer months and are therefore likely to be important components of the benthic food web. Living in the same region, these flounder share the same resources and may therefore directly compete. We investigated whether the four flounder species partition the resources by means of their diets and spatial area. Flounder were collected at weekly intervals at two stations in the bay from June to August of 2004. Stomach contents were sorted to the lowest taxonomic level possible, counted, and weighed. While there was some prey overlap, diet composition analysis by weight showed that each species of flounder had a different prey preference. The dominant prey categories in summer flounder were fish and mantis shrimp, winter flounder preferred worms and amphipods, fourspot flounder ate squid, and windowpane flounder ate mostly *Crangon*. The only significant prey overlap between summer, fourspot, and windowpane flounder was for *Crangon*, however, the high abundance of this prey in the summer makes competition unlikely. The diet of summer flounder varied between station, reflecting the prey available at each location; in contrast, the winter flounder diet was the same at both stations. Fourspot and windowpane flounder were not collected at the mid bay site, therefore their diets were not analyzed by location.

1. Introduction

Weekly bottom trawls sampled over the past 40 years have indicated that summer flounder (*Paralichthys dentatus*), winter flounder, (*Pseudopleuronectes americanus*), fourspot flounder (*Paralichthys oblongus*), and windowpane flounder (*Scophthalmus aquosus*) are the most common flounder species present in Narragansett Bay (GSO Fish Trawl). The abundance of these species suggests that they may consume a large amount of prey and play an important role in structuring the community. Their contribution to maintaining an ecological balance in the bay warrants further investigation to understand how they interact with each other and to determine their means for acquiring resources. These four species are typically summer residents that migrate into the bay during the warmer months (GSO Fish Trawl).

The four common species share a similar morphology of a flattened body, pale underside, and binocular vision (Link, 2002) that make them well adapted to living in the benthic region of the water column (Figure 1). This benthic habitat renders them likely to utilize the same resources, which potentially leads to direct competition for those resources. According to Gause's Competitive Exclusion Principle, if two or more species share the same ecological requirements, ultimately the less dominant species will be eliminated by another that out competes it (Gause, 1934; Begon, 1986). In a similar study investigating different species of warblers, MacArthur (1958) determined that in order for all species to coexist in the same community they must partition their resources. Resources could be divided in a number of ways such as varying their diets, living on different substrates, or feeding at different times of the day (MacArthur, 1958).

The general feeding ecology of flounder is well documented in the northwest Atlantic, (Bowman, 2000; Bigelow & Schroeder, 2002; Link 2002) however, little is known about the diets of flounder in Narragansett Bay. This study focuses on resource partitioning between the four species of flounder by means of their diets as well as by living in different areas on different substrates. Toward this goal, a weekly bottom trawl survey was used to collect the species, and stomach contents were analyzed to observe the similarities or differences in their diets.

2. Methods and Materials

2.1. Data Collection

This study was conducted for an eight-week period between June and August of 2004. Sampling was performed at two stations, (Fox Island and Whale Rock) in Narragansett Bay in Rhode Island Sound (Figure 2). Each week a research otter trawl was towed for 30-minutes at both stations, as described by Jeffries (1974). Fox Island is located in the mid bay of the west passage (41°34.439 N, 71°24.310 W). The sample depth ranged between 6.10 m and 9.14 m. Whale Rock is located at the mouth of the west passage (41°26.256 N, 71°25.488 W) which has a sample depth ranging between 18.29 m and 24.38 m. Towing speed is approximately 2 knots. Each of the four species for this experiment (*Paralichthys dentatus*, *Pseudopleuronectes americanus*, *Paralichthys oblongus*, and *Scophthalmus aquosus*) were collected and subsequently examined in the lab. Five fish of each species at the two stations were collected, all of varying sizes. Tows containing less than five fish of a certain species were still used in the analysis.

Immediately upon returning to the lab, the total body wet weight, total body length and gape width was measured for each fish. Stomachs were removed by an

[1]Now at Fairfield University

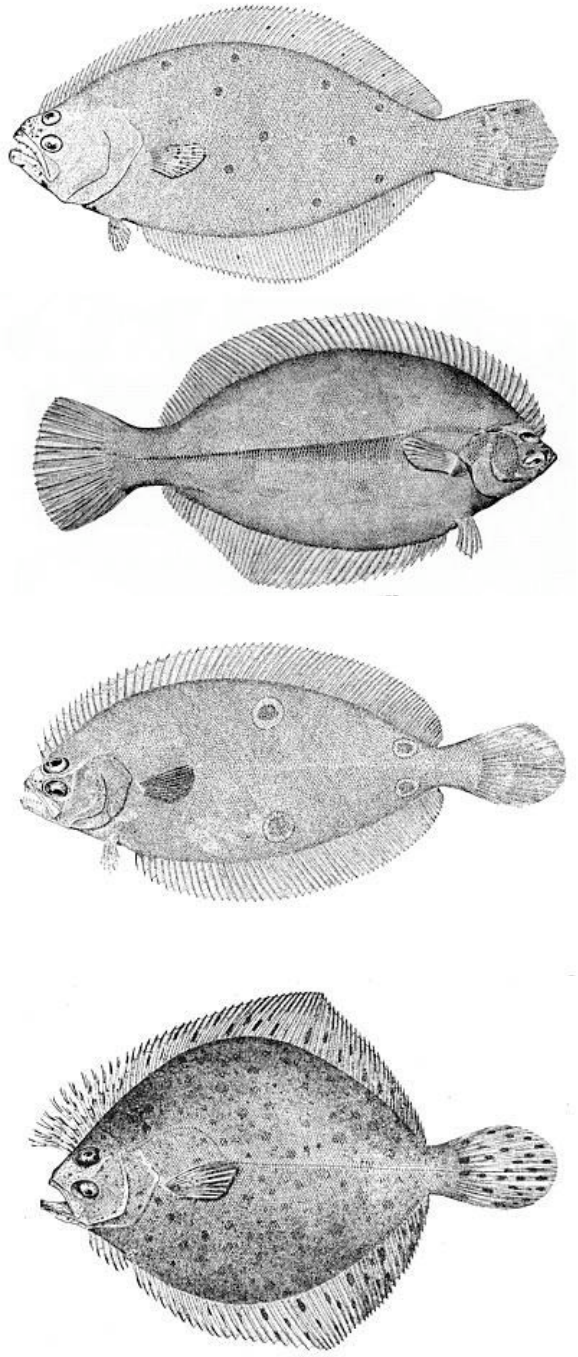

Figure 1. Depictions of the four species of flounder used in this study. Drawings from National Marine Fisheries Service (NEFSC): http://www.nefsc.noaa.gov/lineart/. (a) Summer Flounder (*Paralichthys dentatus*), (b) Winter Flounder (*Pseudopleuronectes americanus*), (c) Fourspot Flounder (*Paralichthys oblongus*), (d) Windowpane Flounder (*Scophthalmus aquosus*).

incision at the base of the esophagus as well as at the beginning of the small intestine. After the stomach was removed it was cut open and the mass of the contents was obtained to the nearest 0.001g with a Mettler PM200 balance. Once weighed, the contents were

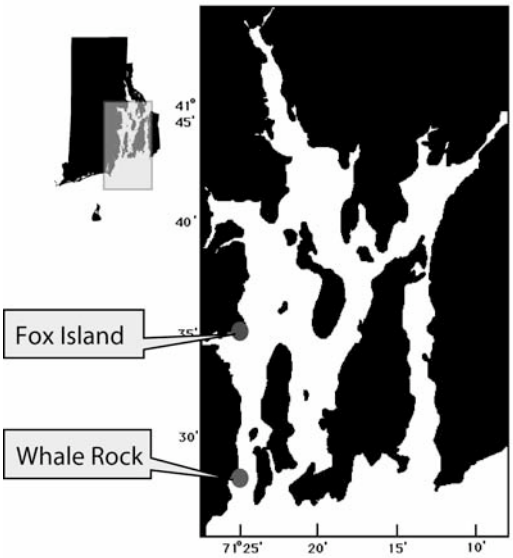

Figure 2. Locations of the two stations sampled during the weekly bottom trawl in Narragansett Bay.

placed in a properly labeled jar and kept on ice in order to hinder the digestion process. The material found in the stomachs of each species was then examined in a Petri dish under a dissecting microscope. This procedure followed a related approach performed by Jeffries (1974) and Link (2002). Stomach contents were identified to the lowest possible taxa and separated into taxonomic groupings. These groupings were then individually weighed for each stomach.

2.2. Data Analysis

For each of the four species of flounder, a total stomach-content weight as well as total prey abundance was calculated in order to present the most complete depiction of their diet compositions. Total weight was computed by adding the weights of each individual prey category together. The total abundance for each category was determined in the same manner. Once a total was obtained for each particular species, prey were grouped into eight general categories: fish, squid, crab, clam, amphipod, *Crangon*, mantis shrimp, and worm. Each category was then computed as a percentage of the total stomach-content weight for all individuals of a single species of flounder. Although both weight and abundance are presented in this paper, the primary analysis for this study utilizes the prey biomass in comparisons rather than abundance. This is due to the fact that the fish obtain their energy from the mass of food consumed, not by the number of prey they consume.

The mean stomach-content weight for individual prey categories within each species of flounder was then calculated. Mean stomach contents were measured by adding the total weight of a specific prey category and then dividing that by the number of individuals for that particular species of flounder that were sampled. Fish with empty stomachs were included in the calculation of mean stomach-content weight so that every fish sampled was used in this analysis.

The mean stomach-content weight of individual prey categories was determined for Fox Island and Whale Rock separately. The two sites were then placed against each other on the same graph for comparisons. When analyzing whether flounder partitioned their diets between the two sites, only summer and winter flounder were analyzed. Both fourspot and windowpane flounder were rarely collected at Fox Island over the eight weeks (Table 1). Fourspot and windowpane flounder were not considered in comparing the difference between sites because the small sample size at Fox Island would have a stronger influence on the outcome. As in the previous analysis, only data containing weight information was used for comparisons when testing substrate partitioning.

With the software program Primer 5, a multi-dimensional scaling (MDS) technique was performed by applying the mean stomach-content weight in grams for each flounder species collected every week, each as a separate sample. The MDS method configured these samples in a way that every sample was crossed with the others and the similarity between samples were arranged in a matrix. When graphed, the samples that were most similar to each other were located the closest together, while the samples that were the least similar were the farthest apart. For example, if sample 1 had a higher similarity to sample 2 than it did to sample 3, then sample 1 would have been placed closer to sample 2 on the plot than it was to 3 (Clarke, 1994).

Unidentifiable remains were considered as a separate prey type in the analysis. The weight of unidentifiable contents only contributed in calculating the total stomach content weight, which was used when calculating the percentages of general prey categories. Even though they are not assigned to a specific prey category, nevertheless they are still part of the flounder diet and should be considered. The same approach was implemented by Link (2002). Flounder that had empty stomachs were still considered as a sample, however, did not contribute to the prey data.

Date	Stn	Summer	Winter	F'spot	W'pane
6/21/04	FI	5	5	1	1
	WR	5	5	5	0
6/28/04	FI	6	5	1	0
	WR	5	5	5	5
7/6/04	FI	4	5	0	0
	WR	5	5	5	5
7/12/04	FI	5	5	0	0
	WR	5	5	5	5
7/19/04	FI	5	5	0	0
	WR	4	5	5	5
7/26/04	FI	5	5	0	0
	WR	5	5	5	5
8/2/04	FI	5	5	0	0
	WR	4	5	5	5
8/9/04	FI	5	5	0	0
	WR	5	5	5	5
S FI		40	40	2	1
S WR		38	40	40	35
Total		78	80	42	36

Table 1. Number of flounder collected per week at each station.

3. Results

The original data documenting the initial measurements for each flounder collected over the eight weeks as well as the stomach-content composition for each flounder. All results will be presented in relation to the eight general prey categories in order to facilitate comparisons among species and locations.

.

3.1. Comparison by Weight

3.1.1. Summer Flounder. Summer flounder was observed to have a significantly different diet preference from the other three species. The two dominant prey categories found in their stomachs were fish and mantis shrimp, which combined represented 77.48% of their diet by weight (Table 2, Figure 3).

	Summer	Winter	Fourspot	W'pane
Fish	44.80	0	13.80	2.13
Squid	1.92	0	54.90	1.16
Crab	5,00	1.95	2.48	0
Clam	0.05	0.48	2.23	0.02
Amphipod	0.49	17.70	0.09	0.09
Crangon	14.80	0.11	25.30	25.3
Mantis Shrimp	32.60	0	0	0
Worm	0.21	31.60	0	0.36
Unknown	0.02	48.10	1.18	0

Table 2. Percent of total stomach contents by weight (g) of eight functional prey groups for four species of flounder collected in Narragansett Bay.

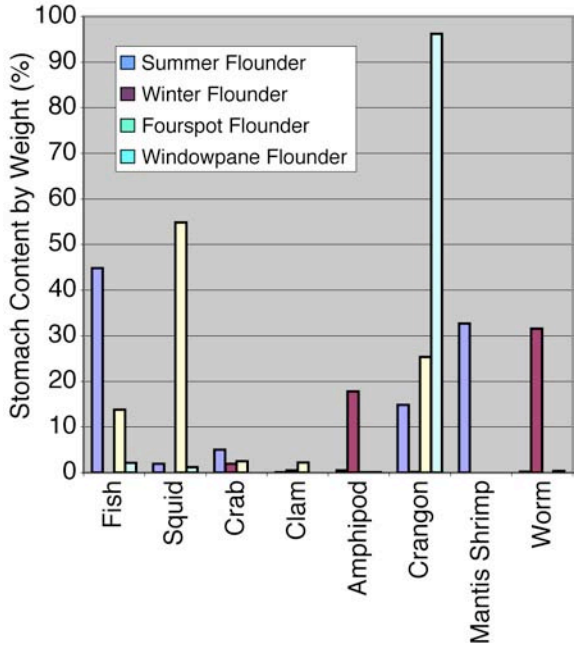

Figure 3. Graph of percent of total stomach contents by weight (g) of eight functional prey groups for four species of flounder collected in Narragansett Bay.

Different eating habits between Fox Island and Whale Rock were discovered between the two dominant prey groups in the summer flounder diet (Table 3, Figure 4). Stomachs sampled at Whale Rock resulted in a 10.22g mean weight of fish compared to a 3.14g mean weight of fish at Fox Island. Conversely, all five of the mantis shrimp present in summer flounder were collected at Fox Island while none were observed in the stomachs collected from Whale Rock. *Crangon*, however, had an approximately equal presence in stomachs at Fox Island and Whale Rock with a mean weight of 2.13g and 2.29g respectively.

3.1.2. Winter Flounder. This species is unique among the four sampled in that it is a right-eyed, small mouth flounder. It had the most distinct diet of the four flounder in this study. The majority of stomach contents consisted of worms and amphipods, both of which represented less than 0.5% by weight in the other flounder (Table 2, Figure 3).

Worms were prevalent in stomachs collected from both Fox Island and Whale Rock with mean weights of 0.488g and 0.665g respectively (Table 3, Figure 4). Similarly, amphipods were found in almost equal amounts between sites as well. Amphipods at Fox Island had a mean weight of 0.319g and at Whale Rock had a mean weight of 0.330g.

3.1.3. Fourspot Flounder. Fourspot flounder had a diet similar to summer flounder, but it had a distinguishing prey preference with 54.87% of its diet by weight consisting of squid. *Crangon* (25.33%) and fish (13.82%) were also prominent prey (Table 2, Figure 3).

3.1.4. Windowpane Flounder. This species had a significantly different diet composition compared to the other three. The major prey component found present in windowpane flounder was *Crangon*, representing 96.24% of their total diet by weight (Table 2, Figure 3).

3.2. Comparison by Abundance

3.2.1. Summer, Fourspot, and Windowpane Flounder. When comparing diet composition by the abundance of prey, *Crangon* was the dominant organism found in the stomachs of summer, fourspot, and windowpane flounder (Table 4, Figure 5). It represented 91.00% of the individual prey items found in the stomachs of summer flounder, 92.53% in fourspot flounder, and 99.62% in windowpane flounder. All other prey categories accounted for less than 5% of the abundance in these three species.

3.2.2. Winter Flounder. While both worms and amphipods were the prevalent prey groups in the diets of winter flounder by weight, amphipods dominated the diet composition over worms in abundance; 78.50% and 10.05% respectively (Table 4, Figure 5).

3.3. Multi-dimensional scaling (MDS).

Comparing the diet similarity among species dates and locations, the diet composition of winter flounder was clearly distinct from the other three species (Figure 6). Summer, fourspot, and windowpane flounder were observed to have some overlap with each other,

	Summer Flounder		Winter Flounder	
Prey Category	Fox Island	Whale Rock	Fox Island	Whale Rock
Fish	3.142	10.224	0	0
Crab	0.932	0.564	0.017	0.055
Squid	0.029	0.545	0	0
Amphipod	0	0.148	0.319	0.330
Crangon	2.135	2.294	0	0.004
Mantis Shrimp	9.758	0	0	0
Clam	0.014	0	0.006	0.011
Worm	0.062	0.001	0.488	0.666

Table 3. Mean stomach content weight (g) by site for all summer and winter flounder sampled.

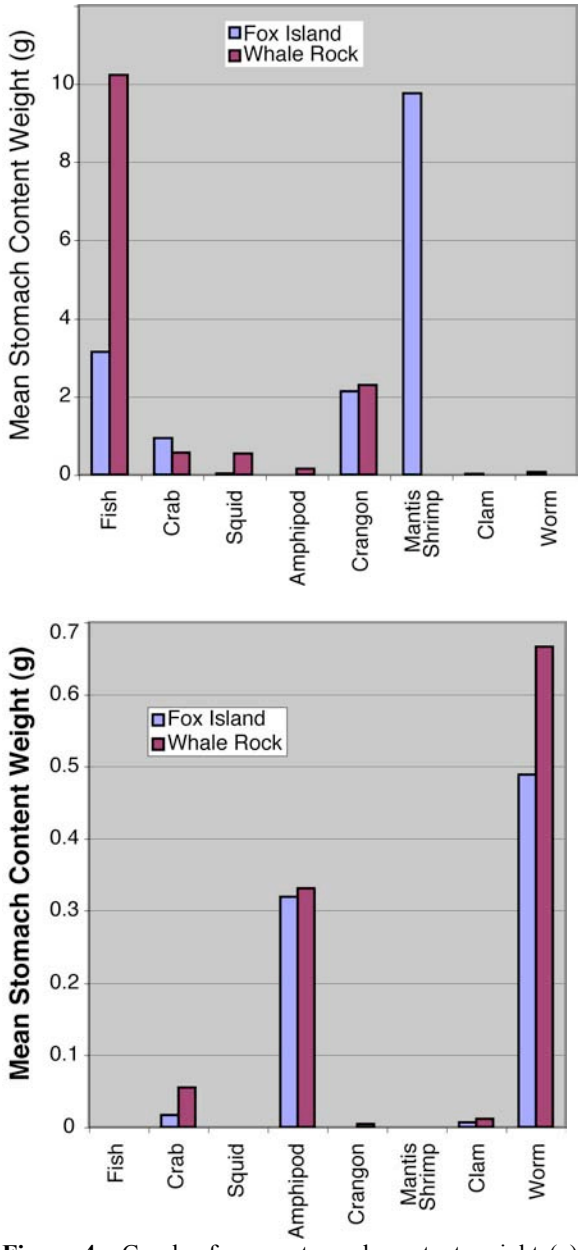

Figure 4. Graph of mean stomach content weight (g) by site for all summer flounder (top) and winter flounder (bottom) sampled.

	Summer	Winter	F'spot	W'pane
Fish	2.68	0	0.17	0.06
Squid	0.30	0	1.02	0.08
Crab	1.19	9.81	4.41	0
Clam	0.07	1.20	0.68	0.06
Amphipod	2.83	78.5	1.19	0.13
Crangon	91.0	0.48	92.5	99.6
Mantis Shrimp	0.37	0	0	0
Worm	1.56	10.05	0	0.04

Table 4. Total stomach contents (%) of functional prey groups for flounder collected in Narragansett Bay.

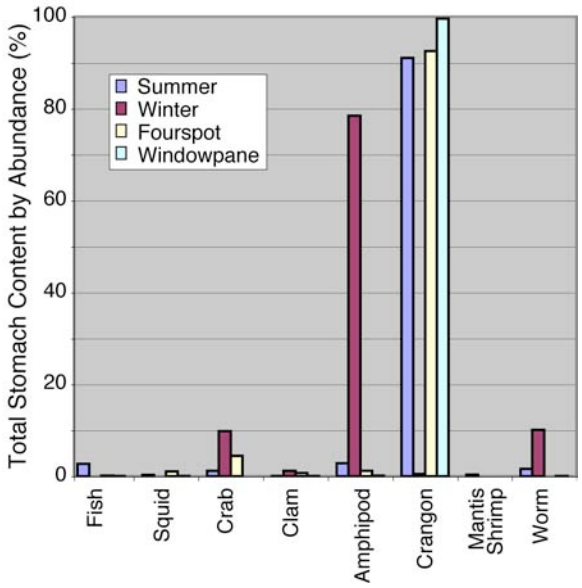

Figure 5. Total stomach contents of functional prey groups for flounder collected in Narragansett Bay.

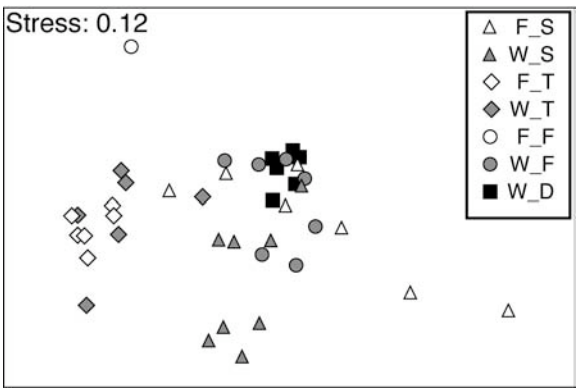

Figure 6. Primer 5 software of Multi-dimensional scaling (MDS). Mean stomach content weight of eight prey categories by date, station, and species of flounder. Displaying which species at which station eat similar prey by weight. For clarity purposes, each species and each station sampled was abbreviated in the legend. The format for each label was "Station_Species." Fox Island (F) and Whale Rock (W) are indicated. Summer Flounder (S), winter flounder (T), four-spot flounder (F) and windowpane flounder (D) are shown.

indicating a similarity in their diets. Both winter and windowpane flounder each showed an overlap in prey composition between the two stations sampled. Due to the fact that only one windowpane flounder was collected at Fox Island thisresult may not signify the overlap appropriately. Winter flounder however, showed an equal distribution of samples from the two sites, which indicates the overlap is accurate. There were a few outliers from the main cluster of winter flounder. One, located closer to the summer, fourspot, and windowpane bundle, had *Crangon* in its stomach, which was the only sample for that species to contain that prey. Summer and fourspot flounder showed little or no relation in diet between the two sites. One of the fourspot flounder sampled at Fox Island was located far from the vicinity of any other samples. Comparable to windowpane flounder, only two fourspot flounder were sampled from Fox Island for the entire period, therefore the distinct point may not present correct results. One of these fourspot had the only turbonille snail found in its stomach. Since the summer flounder had a large amount of unidentified bony fish in their stomachs, it is difficult to explain their similarities or dissimilarities in the MDS plot because the unidentified fish could actually be classified under a specified fish category.

In the overall MDS plot, a general trend can be observed where the diets of the flounder are organized in three major prey groups; fish, *Crangon*, and worms. The cluster of winter flounder on the left side of the figure represents the worm eaters, the closely spaced bunch of windowpane, fourspot, a few summer, and one winter flounder located in the middle of the plot are the flounder which ate *Crangon*, and the remaining summer and fourspot flounder in the right and bottom middle are the ones that ate fish. By following this trend, the x-axis can then be interpreted as the size of prey with smallest to largest going from the left to the right of the plot.

4. Discussion and Conclusion

In this study, resource partitioning was investigated between the four most common species of flounder sampled in Narragansett Bay. I examined whether the flounder partition resources through their diets or by feeding in different areas. The important role of flounder in the ecosystem, as well as the lack of data concentrating on flounder's diets in the Narragansett Bay area provided justification for this investigation.

In terms of biomass, the four species of flounder were observed to eat different types of prey; or if they ate the same type, ate them in different amounts. As shown in Table 2 and Figure 3, each species had its "own" dominant prey category in its stomach contents. Reasons to explain and validate these results will be further discussed in this section.

The occurrence of *Crangon* in the summer, fourspot, and windowpane flounder diets can be accounted for by previous data confirming its abundance in the benthic environment (Grassle, 1986; Whitehouse, 1994; GSO

benthic sampling). Furthermore, Whitehouse (1994) and Grassle (1986) affirm that this arthropod is found in plentiful amounts during the summer months, which was when this study occurred. As a result, we cannot deduce that summer or fourspot flounder have a preference for *Crangon* or if they simply eat it because of its abundance. Such an ample amount makes it much easier to find and consume. Moreover, *Crangon* was not the dominant prey type observed in the stomachs of summer or fourspot flounder. It only represented 14.8% and 25.3% of their diets by weight respectively. Windowpane flounder however, had 96.2% of their stomach contents consisting of *Crangon*. Since almost all of their diets contained *Crangon*, it is most likely they do prefer this prey.

The two stations sampled vary by depth as well as substrate composition. ROV footage by Jeremy Collie, as well as a number of other sources have shown that Fox Island, located in the mid bay, consists of silt and mud, while Whale Rock, at the edge of the west passage, has a sandier bottom (McMaster, 1960; Grassle 1986). Since these two sites are clearly different, it can be tested whether flounder partition their diets by feeding in other areas. Unfortunately, only summer and winter flounder were regularly collected at both stations. The lack of fourspot and windowpane flounder at Fox Island however, presents interesting speculations. It is possible these two species have partitioned their habitat with summer and winter flounder by living in deeper waters. Since temperature decreases with depth, they could also prefer to live in lower temperatures during the summer. Even though *Crangon* is readily found throughout the bay in the summer, Whitehouse (1994) had discovered that it had one of the greatest densities and abundance at Whale Rock. This could be due to the fact that *Crangon* favor sandier sediments in order to bury themselves. Even though *Crangon* did not represent the greatest prey amount by weight in fourspot flounder, it did represent a quarter of their stomach contents by weight. Along with the fact that *Crangon* dominated the diets of windowpane flounder, another possibility for the two species of flounder to be found only at Whale Rock could be the location of this prey.

From Table 3 and Figure 4, it can be inferred that summer flounder do vary their diet between stations. The most prevalent prey category in their diets was fish. It can be seen that silver hake was the most dominant fish and represented 41% of the mean stomach weight in summer flounder. Unidentified bony fish were the second most common in the stomachs of summer flounder (33%), however, some of these unidentified fish could have been silver hake. Data from the GSO Fish Trawl from June to August of 2004 showed that silver hake are more prominent at Whale Rock than Fox Island. Knowing it is more abundant at Whale Rock, and that by weight was found more in summer flounder sampled from Whale Rock, it can be proposed that this species has a variable diet and consumes prey that is most abundant. Link (2002) also stated that the diet composition of summer flounder generally tracks the abundance of forage fish. Similarly, mantis shrimp were only sampled in the GSO Fish Trawl at Fox Island throughout the summer. Likewise, they were only observed in the diets of summer flounder collected from Fox Island which further indicates that the diet of this species reflects prey availability.

Winter flounder on the other hand seem to eat the same types of prey at both Fox Island and Whale Rock (Table 3, Figure 4). Worms and amphipods represented the majority of their diet (Table 2), and both categories were observed in similar amounts by mean weight (Table 3) at the two stations. This suggests that while winter flounder have very different diets than the other species, they do not vary their diet by living in different areas.

Additionally, the gape width of the mouth of each flounder for a given species was plotted against the body length and can be found in the appendix as Figure 7. Five points were omitted from the fourspot flounder data because they came from the first week and were deemed unreliable. For each species there was a positive correlation between the two measurements; as body length increased, so did the gape width. It was found that the gape width of summer flounder was on average 12% of the body length. Winter flounder however, had an average gape width of only 4% compared to their body length. Both fourspot and windowpane flounder had an intermediate gape-width size of approximately 7% of the body length. Therefore, it can be further implied that winter flounder will have different diets compared to the other three since they would not be able to fit large prey items such as fish, squid, or mantis shrimp in their mouths.

This investigation demonstrates the separation of diets among summer (*Paralichthys dentatus*), winter (*Pseudopleuronectes americanus*), fourspot (*Paralichthys oblongus*), and windowpane (*Scophthalmus aquosus*) flounder in Narragansett Bay. Each species has an individual prey preference, but there is a slight overlap that could potentially be due to prey abundance and availability. Summer flounder favor fish, winter flounder fancy worms, fourspot flounder enjoy squid, and windowpane flounder prefer *Crangon*. From collection and analysis, summer, fourspot, and windowpane flounder also vary their diets by location. By utilizing this adaptation, these four species, which are similar in body structure and habitat, are able to comfortably coexist in Narragansett Bay. Since winter flounder have such a smaller body and gape size than the other three flounder, there is no need to partition their diets by substrate. They are physically unable to eat the same organisms that the other flounder eat.

Due to the lack of benthic data, it is unclear if the flounder are selective predators or simply consume the most abundant organisms. For further investigation to present the most accurate results of this study, prey abundance and biomass information for each station should be sampled. A correlation between the prey sampled in the bay and the prey sampled in the stomachs of the flounder could then be made which would clarify if flounder eat selectively or just eat the most abundant prey that is available.

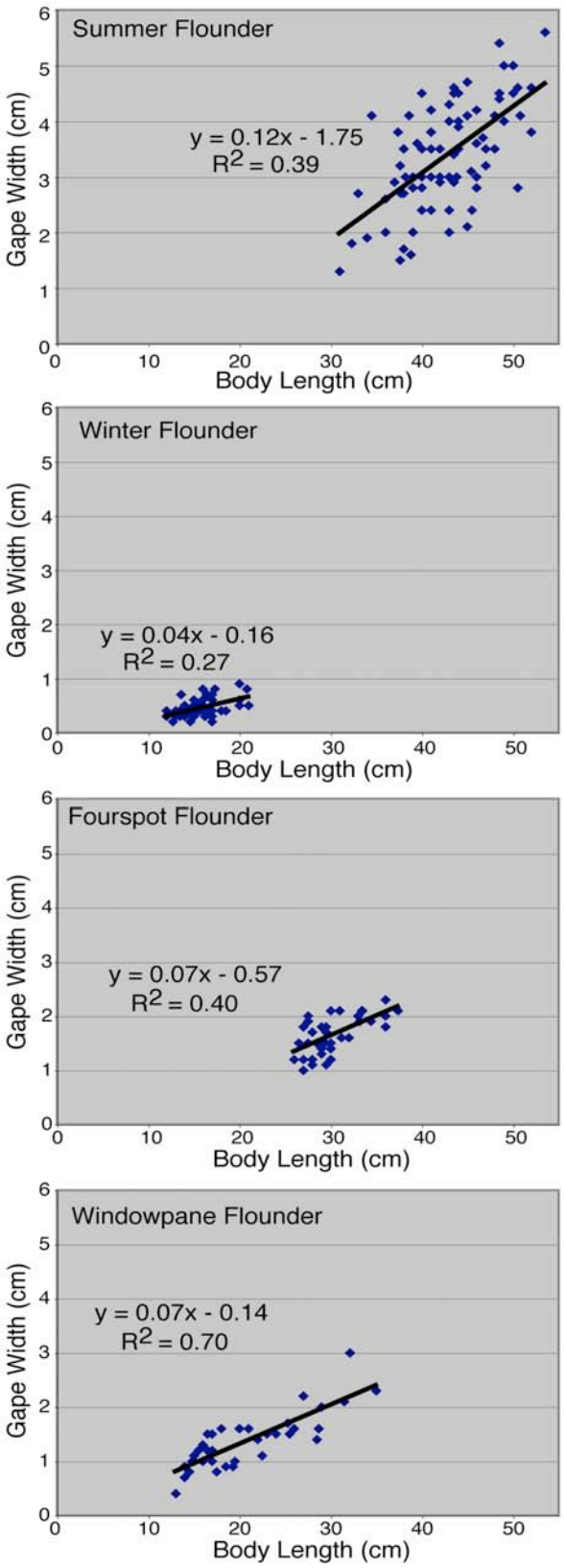

Figure 7. Gape width vs. body length for four species of flounder. (a) Summer Flounder, (b) Winter Flounder, (c) Fourspot Flounder, (d) Windowpane Flounder.

Acknowledgments. Thanks are due to Jeremy Collie and Rich Bell. Both have been extremely kind and patient, and always made me feel comfortable in their lab. Even if they were busy, they always made themselves accessible to me. Their positive attitudes and constant encouragement allowed me to have such a wonderful experience. Jeremy introduced me to the field of biological oceanography, helped me organize and analyze my results, and improved my knowledge of statistics. Rich helped me collect the flounder on the Cap'n Bert, gave me fascinating field experience, and expanded my knowledge of ecological concepts. Also, thank you to Rebecca Asch for allowing me to borrow her foul-weather gear so that I could stay clean and dry while collecting my samples on the trawl. Lastly, thank you to Rob Pockalny, Rich Viso, and Kim Carey for this amazing opportunity and the other SURFO's for a great time this summer.

References

Begon, M., J. L. Harper, and C. R. Townsend. 1986. Ecology. Sinauer Associates, Inc.: Massachusettes. p. 259-260.

Bigelow & Schroeder. 2002. Fishes of the Gulf of Maine. Smithsonian Institution Press: Washington, p. 548-550, 554-558, 559-560, 579-585.

Bowman et al. 2000. Food and Northwest Atlantic Fishes and Two Common Species of Squid. *NOAA Tech. Memo,* NMFS-NE-155.

Clarke, K. R., and R. M. Warwick. 1994. Change in Marine Communities: An Approach to Statistical Analysis and Interpretation. Plymouth Marine Laboratory: UK. p. 5.1-5.2.

Gause, G. F. 1934. The struggle for existence. Baltimore: Williams and Wilkins.

Grassle, J. F. et al. 1986. Subtidal Macrobenthos of Narragansett Bay. Field and Mesocosm Studies of the Effects of Eutrophication and Organic Input on Benthic Populations. *Mar. Biol. Of Polar Regions and Effects of Stress on Mar. Organisms*.

GSO benthic sampling. 2000-2002. Monitoring the Benthic Community of Narragansett Bay. Advisor: Dr. Candace Oviatt. http://www.gso.uri.edu/benthos/

GSO Fish Trawl. 1959-2004. Narragansett Bay Fish Trawl. Advisor: Dr. Jeremy Collie. http://www.gso.uri.edu/fishtrawl/

Jefferies, P. H., and W. C. Johnson. 1974. Seasonal Distributions of Bottom Fishes in the Narragansett Bay Area: Seven-Year Variations in the Abundance of Winter Flounder (Pseudopleuronectes americanus). *J. Fish. Res. Board Can.*, **31** (6): 1057-1066.

Link, J. S., K. Bolles and C. G. Milliken. 2002. The Feeding Ecology of Flatfish in the Northwest Atlantic. *J. Northw. Atl. Fish. Sci.*, **30**: 1-17.

MacArthur, R. H. 1958. Population Ecology of Some Warblers of Northeastern Coniferous Forests. *Ecology,* **39** (4): 599-619.

McMaster, R. L. 1960. Sediments of Narragansett Bay System and Rhode Island Sound, Rhode Island. *J. of Sedimentary Petrology*, **30** (2): 249-274.

Whitehouse, S. T. 1994. The Abundance and Distribution of *Crangon septemspinosa* in Narragansett Bay. PhD Dissertation: University of Rhode Island. Narragansett, RI, p. 1-25.

K. J. Banahan and J. S. Collie, Graduate School of Oceanography, University of Rhode Island, Narragansett, RI 02882. (05_kbanahan@stagweb.fairfield.edu, jcollie@gso.uri.edu)

Copyright 2004 by the Graduate School of Oceanography/University of Rhode Island, SURFO program

First steps to acoustically tracking fish and floats in shallow water

Daniel Dean[1], and Thomas Rossby

Graduate School of Oceanography, University of Rhode Island, Narragansett, Rhode Island

Abstract. Oceanographers have used acoustics extensively to study deep ocean currents and to track fish over short ranges, but the use of acoustics to study shallow water (depth less than 1000m) currents and to track fish over long distances is still in its infancy. This project is part of a greater venture to use passive acoustic sensors to monitor fishes' movements. Such sensors are modeled after existing RAFOS (SOund Fixing and Ranging spelled backwards) technology and promise greater precision and range in locating the tagged fish species. This project also assists in the development of new RAFOS floats to be used to study currents on the continental shelf by determining the transmission range for the acoustic signal used by current RAFOS float technology. To determine the possible range for tracking passive acoustic fish tags and floats, we used a numerical model. There exist many numerical models for the propagation of sound in the shallow seas, but they have not been used to evaluate the feasibility of long-range acoustic tracking techniques in shallow waters. Using the acoustic signal incorporated in current RAFOS float and fish tracking technologies, we compared the transmission loss predicted by the Monterey Miami Parabolic Equation (MMPE) numerical model of wave propagation to the transmission loss determined experimentally. Our results have given us confidence in the relative transmission losses, but more testing must be done to quantify the amplitude of the expected transmission loss. We also ran the MMPE model for the area of a proposed fish study in Georges Bank. Although the results look promising, little can be said about the expected transmission ranges there without first knowing the accuracy of the model.

Introduction

Currently, oceanographers use acoustics extensively to study deep ocean currents and to track fish. Physical oceanographers use RAFOS floats to track currents over thousands of kilometers. These floats were named after their predecessor, the SOFAR float (SOund Fixing and Ranging). The name was reversed because in the RAFOS system an acoustic signal is transmitted in the opposite direction to the SOFAR system. The RAFOS float is an autonomous, isopicnal float that receives and records an acoustic signal from an anchored sound source. When the float reaches the end of its mission at sea, it rises to the surface by dropping a ballast weight and transmits its data to a satellite. By looking at the signal arrival times from two or more sound sources, one can track the float's location (Rossby et. al., 1986). Oceanographers are able to track the floats over long distances in the deep ocean because the floats take advantage of the sound channel created by the sound speed gradient with depth. RAFOS floats have not been adapted to study shallow water currents because the density structure and sound speed gradient of shallow water are not as well defined as they are in the deep ocean.

As with Lagrangian methods for studying deep-ocean currents, existing methods for tracking fish over long distances are limited by a lack of familiarity with the long-range acoustic properties of the shallow seas. Current fish tracking methods use tags that collect data about the fish's physical environment or send high-frequency acoustic signals to anchored hydrophones. The tags that collect data on the fish's depth, the surrounding water temperature, or the ambient light are unable to precisely locate fish. The current acoustic tags can precisely locate fish, but they only operate at ranges up to one kilometer and are limited by their battery life and size (Welsh et al., 2002). These acoustic tags are limited in range because the tags transmit at high frequencies and because they are not able to produce a very strong signal.

This project is part of a larger venture to adapt RAFOS floats to study shallow water currents and enable acoustic fish tracking to extend to long ranges. To adapt RAFOS floats to shallow water, we must first characterize the acoustic properties of the water to ensure that we will have an adequate transmission range. If the transmission range is long enough to study shallow water currents, we can use the same technology to acoustically track fish. We can extend the range at which we can track fish by using tags that act like RAFOS floats. By using tags that record sound signals from anchored sound sources, the signal used could be more energetic and of a lower frequency (Lee et. al., 2002). This would allow us to significantly improve the range over which we could track fish and to use the same transducer array to track both fish and floats. This project is the first step to developing such a system of transducers because it gives us a familiarity with the model that is proposed for use in determining the expected transmission range.

Methods

The method of this project was formed around the idea of creating an active transducer array in Georges Bank to study the currents and fish populations there. Specifically, this research targets the yellowtail flounder, an important commercial fishery in Georges Bank. Preliminary results from a currently ongoing study of yellowtail flounder indicate that tagged flounder are recaptured an average of 23km from their release point and that they tend to move East across the

[1]Now at Gonzaga University

northern edge of Georges Bank (Cadrin et al., 2004). Thus, a transducer array should cover a distance of at least 23 km from the fish release point and should extend from East to West on the Northern edge of Georges Bank.

To get a feel for the possible transmission distances that we could obtain in the northern area of Georges Bank, we modeled the area using a parabolic equation numerical model. We tested the accuracy of the model for shallow water applications by comparing the transmission loss calculated for an area in Narragansett Bay to a measured transmission loss. To model the transmission loss expected in Georges Bank and Narragansett Bay we used the 2D Monterey-Miami Parabolic Equation developed by Kevin Smith. We chose this model because it gave us transmission loss as a function of range, because it is efficient in long-range shallow water applications, because it was easily accessible, and because the program creator has been helpful in the past studies involving his model. This model has seven input files that characterize the environmental data and the output characteristics. To run the model we input environmental data defining the sound speed profile in the water column, the bathymetry of the ocean bottom, the acoustic characteristics of the sediment, the bathymetry of the acoustic basement, and the acoustic characteristics of the acoustic basement.

When gathering the information to model the transmission losses in the West Passage of Narragansett Bay and in Georges Bank, we had to make several approximations. First, when creating the sound speed profiles, we used CTD data that were taken as close as possible to the area of study during the months of July and August. Since the sound speed profile in shallow water changes significantly over the cycle of a year and varies extensively from place to place, the expected transmission range would change with time and place. If this model is going to be used to assess the transmission range in a study lasting more than the scale of seasonal change, the experimenter should evaluate acoustic propagation for all seasons of interest rather than a single period as we have in this study. Second, we used sediment characteristics derived from Edwin Hamilton's 1980 paper on geoacoustic modeling of the sea floor. As a result, the sediment characteristics are generalized values that may not exactly match those of the area of study. Third, the model does not account for more than two vertical layers of sediment. In area such as Georges Bank where the surface layer is fairly homogenous, this does not cause problems as it would in sediment that had many layers with reflecting boundaries and varied sediment properties. Fourth, we were unable to obtain information on the bathymetry or properties of the acoustic basement in the Georges Bank area, so we assumed it had a sediment thickness similar to the glacial moraines in Rhode Island and Block Island Sounds (McMaster, 1968; Needell and Lewis, 1984).

To test the accuracy of the MMPE model and to get a feel for the possible transmission ranges, we measured the transmission loss in the area we modeled in the West Passage of Narragansett Bay. We used the same signal currently used by RAFOS technology: a 1.5 Hz bandwidth sinusoidal signal centered at 260 Hz lasting for 80 seconds. We generated this signal using Matlab on a laptop computer, amplified it using a Clarion APX 200.2 audio amplifier, and we projected the signal into the water using a Clark Synthesis AQUA 229ABS underwater pool speaker. To receive and record the acoustic signal we used a Benthos AQ-18 hydrophone attached to another laptop computer. We hung the hydrophone into the water off the eastern edge of the GSO dock at 3 meters depth. We then sent a signal using the underwater pool speaker from five locations East and North of the GSO dock using a sailboat provided by University of Rhode Island faculty member Conrad Recksiek. The first three transmission tests were directly East of the GSO dock, and the other two were to the North of Dutch Island.

To ensure that the AQ-18 hydrophone and underwater pool speaker were calibrated correctly, we tested them at the GSO dock using an ITC-8212 hydrophone. We placed the pool speaker at two meters depth off the northern end of the dock, and we placed the two hydrophones at the same depth 1 meter from the pool speaker. We then transmitted a 260hz signal as before and monitored the signal received by both hydrophones with an oscilloscope.

Results

From the transmission tests run in Narragansett Bay, we obtained a strong signal across the West Passage. We lost the signal as we moved between 2.14 and 2.85 km Northeast of the GSO dock because the transmission path over much of the distance was less than two acoustic wavelengths deep. From the calibration test, we determined that the pool speaker and hydrophone setup used to test transmission loss in Narragansett Bay gave a received signal strength 2dB too high. This makes the measured transmission losses 2dB higher than measured when corrected for the measured calibration.

For the same transect of Narragansett Bay in which we tested the transmission loss directly, the MMPE model gave values for the transmission loss at 609m and 1.044km of 35 and 40 dB re 1μPa. See table 1 for a list of all positions, the measured transmission loss, and the transmission loss predicted by the MMPE. Surprisingly, the measured and calculated transmission losses are different by 22 dB. This difference may be due to incorrectly setting the gain on the computer recording the signal. At the time of recording, we did not realize that the computer's input gain is controlled from two

Longitude (deg)	Latitude (deg)	Distance from GSO dock (km)	Measured Loss (dB re 1μPa)	MMPE Loss (dB re 1μPa)
-71.41831	41.49267	0.0253	37	n/a
-71.41133	41.49239	0.6086	57	35
-71.40611	41.49269	1.0440	62	40
-71.40386	41.50836	2.1370	78	n/a
-71.39989	41.51411	2.8510	n/a	n/a

Table 1. Transmission loss in the West Passage of Narragansett Bay.

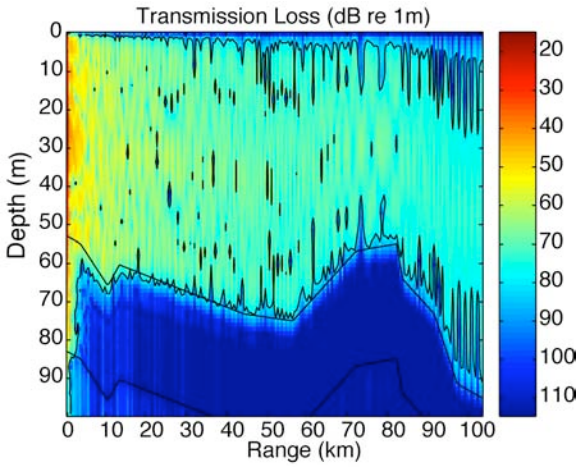

Figure 1. Output from MMPE model for a 100km transect of Georges Bank from 41°40.5'N -68°24.5'W to 42°5.55'N -67°30.0'W.

independent locations: on the keyboard and in internal settings. It is possible that the measured transmission losses could be as much as 15-20 dB less, but we can't be sure that this is our source of error.

Running the MMPE model for the chosen section of Georges Bank gave transmission loss at 100km to be 80 dB re 1μPa. See Figure 1 for the output from the MMPE model used in this study. If we assume that the source transmits at 180dB re 1μPa at 1m, a transmission loss of 80 dB would yield a sound pressure level at 100 km of 100dB. If we further assume that ambient noise is 70dB re 1μPa, we would have a signal to noise ratio of 30dB. This strikes us as too large, but at this juncture we do no know why. One the one hand, a shallow sea may act as a duct for sound reducing losses from those expected by spherical spreading (100dB). On the other hand, losses to the bottom sediment at low frequencies would increase the losses expected from cylindrical spreading (50dB). Clearly these effects will require further study.

Discussion

The results from the transmission test in the West Passage of Narragansett Bay indicate that the MMPE model reliably predicts the relative transmission loss from one distance from the sound source to another, but we are unable to determine if the amplitudes of these values are accurate. Before using the MMPE model to design a sound source array for an area like Georges Bank, it would be best to test the model more thoroughly at long ranges. Since the data we compared included only two data points over a distance of only 1 km, more tests at ranges comparable to 100km must be made. Furthermore, the calculated transmission losses were 22 dB lower than the measured values, indicating that there is either a flaw in our experimental method or in the numerical model.

Even if further study shows that the transmission losses in Georges Bank are 20-30 dB higher, transmission to 100km may be possible. We must keep in mind that the detection threshold for the type of FM signal used in RAFOS floats is S/N = -6dB. If the ambient noise is 70 dB and if we used the currently available 180 dB sources, we could have a transmission loss of 116 dB and still detect the signal.

If the MMPE model is later proven to be accurate in long-range, shallow water applications, the estimated transmission range of at least 100km would allow us to adequately cover the area of interest in studying yellowtail flounder, the northern half of Georges Bank, using only three sound sources. As a result, a yellowtail flounder tracking project utilizing acoustic archival tags would not require excessively more funds or time than currently ongoing fish tagging studies (Cadrin et. al., 2004). Such a study would improve the current knowledge of yellowtail migration patterns in Georges Bank because it would allow a biologist to track a flounder's movements over a long range with a spatial resolution of around 150 meters.

The estimated transmission range of over 100km would also allow oceanographers to study shallow water currents using RAFOS floats. The study of small currents such as the outflow from bays would be a perfect target for such technology. The current RAFOS float design would not work in shallow water because the density structure is too mixed. However, the results from this study can serve as motivation for the development RAFOS floats that could change their density so as to stay at a certain depth or distance from the bottom.

Conclusion

Testing and modeling the transmission loss experienced in the West Passage of Narragansett Bay have shown that the MMPE model gives predictions that suggest that further study of its application to long-range shallow water studies is warranted. The results to date serve as a first order approximation in the characterization of sound in Georges Bank. The MMPE model predicts transmission ranges far enough to economically enable the use of RAFOS floats and passive acoustic fish tags to study Georges Bank.

Acknowledgments. Thank you to all members of the URI faculty and students who made the 2004 SURFO project possible.

References

Cadrin, S., Yellowtail flounder tagging study 2005, *Northeast Consortium proposal*, 2004.

Georges Bank and Nantucket Shoals. U.S. Department of Commerce Map 13200, 33rd Ed., National Oceanic and Atmospheric Administration, Washington D.C., 2002.

Hamilton, E. L., Geoacoustic modeling of the sea floor, *J. Acoust. Soc. Am.* 68(5), 1313-1339, Nov. 1980.

LeBlanc, L.R., Mayer, L., Rufino, M., Schock, S.G., and King, J, Marine sediment classification using chirp sonar, *J. Acoust. Soc. Am.*, 91(1) 107-115, 1992.

Lee, S., Fischer, G., Obara, M., Recksiek, C.W., and Rossby, T.H., An Acoustic data storage tag for long range fish tracking in the ocean, *World Congress of Korean and Korean-ethnic Scientists and Engineers*, Korea, June 2002.

Limeburner, R., Process study CTD data, Gulf of Maine/Goerges Bank, 1997. Endeavor Cruise 269, CTD data station 14 1995. <http://globec.whoi.edu/jg/dir/globec/gb/>

McMaster, R. L., Bedrock surface and overburden at the Jamestown bridge, West Passage, Narragnsett Bay, Rhode Island based on seismic reflection profiling, University of Rhode Island, 1979.

McMaster, R. L. , Lachance T. P. and Grrison L. E. Seismic-reflection studies in Block Island and Rhode Island Sounds, *American Association of Petroleum Geologists Bulletin* 52(3) 465-474, 1968.

McMaster, R.L. and Peck, J., The geology beneath the new Jamestown Verrazano bridge, *Maritimes*, 34(3) 4-6.

Needell, S. W. and Lewis, R .S., Geology of Block Isand Sound, Rhode Island and New York, U.S. Geological Survey Miscellaneous Field Studies Map MF-1621, 1984 <http://woodshole.er.usgs.gov/openfile/of02-002/htmldocs/bissum.htm>.

Pockalny, R., Data from SURFO summer cruise 2003.

Poppe, L.J., Surifcial sediment data from the Gulf of Maine, Georges Bank, and vicinity: a GIS compilation, Woods Hole Field Center, Woods Hole, MA, 2003. http://pubs.usgs.gov/of/2003/of03-001/data/seddata/mcmaster60/mcmaster60.zip

Poppe, L.J., 2003, DEC41_GOM: NODC Lithologic Descriptions:, U. S. Geological Survey, Coastal and Marine Geology Program, Woods Hole Field Center, Woods Hole, MA. <http://pubs.usgs.gov/of/2003/of03-001/htmldocs/data.htm>

Rossby, T., Drorson, D., Fontaine, J., The RAFOS system. *J. Atmospheric and Oceanic Technology*, 3(4), 672-679, 1986.

Welch, D.W., Boehlert, G.W., Ward, B.R., POST-the Pacific Ocean salmon tracking project, *Oceanologica Acta*, Nov. 2002 <http://www.postcoml.org/research/technical-papers.php>.

D. Dean and T. Rossby, Graduate School of Oceanography, University of Rhode Island, Narragansett, RI 02882. (ddean1@gonzaga.edu, trossby@gso.uri.edu)

Copyright 2004 by the Graduate School of Oceanography/University of Rhode Island, SURFO program

Assessing the abundance of a potential energy source (Radiolytic H_2) for subsurface life

Kelly Hanks[1], Steven D'Hondt, Arthur Spivack
Graduate School of Oceanography, University of Rhode Island, Narragansett, Rhode Island

Abstract. Molecular hydrogen (H_2) and oxidants (e.g., H_2O_2, O_2) produced from the radioactive splitting of water may provide a renewable energy source for subsurface microbial communities. We provide a first-order quantitative approximation by numerically modeling how much chemical "fuel" for life is produced from the radiolysis of water in deep subsurface sediments and rocks. Decay of the series of ^{238}U, ^{235}U, ^{232}Th, and ^{40}K provide the radiation (α-particles and β-particles) that split the water into a sequence of hydrogen peroxide, hydrogen radicals and oxygen compounds. The in situ H_2 production rates in the representative rock types (granite, shale, basalt, and ocean sediment) are compared to other biological metabolic rates.

1. Introduction

1.1. Purpose

Geomicrobiology is an interdisciplinary field that integrates geology, chemistry, physics and microbiology to understand the interdependence of microbial activity and geochemical processes. This research explores the geochemical plausibility of a radiolysis-derived hydrogen-based microbial biosphere. We specifically addressed the question: are subsurface hydrogen production rates occurring at levels comparable to other biological activity rates? The research objective was to create a quantitative model to calculate biochemical "fuel" (H_2) production rates from the radiolysis of water in deep, subsurface environments.

1.2. Background Information

1.2.1. Extremophiles and alternative fuel

There is a vast ecosystem of microorganisms underground. Several hundred species of subsurface microbes have been found to date and some are found more than 3 km beneath the Earth's surface (*Onstott et al.*, 2000). Recent findings show that subsurface life makes as much as 1/3rd of Earth's total biomass (*Whitman et al.,* 1998). In this environment, some of the microorganisms may live off the rocks and interstitial water that house them. It has been speculated that these microbes may use energy created from recombining hydrogen and oxygen into water for their energy source and bonding hydrogen with carbon dioxide, where H_2 and O_2 may be the products of the radiolysis of porewater.

1.2.2. Synopsis of the radiolysis of water

Water radiolysis is the decomposition of water by irradiation into a series of ions and compounds. In the subsurface environment, this occurs along the interface between a radioisotope-bearing rock or mineral and porewater. The types of radiation accounted for in these calculations are α-particles (helium ion) and β-particles (high energy electrons) emitted from the rock/sediment. Gamma radiation also causes the radiolysis of water; however it was not included in our calculations for this report. These types of radiation interact with the porewater primarily by an ionization process and facilitate the chemical reactions between substances dissolved in the water; we focus solely on the dissolved gases that are created by splitting H_2O. The end product results in the oxygen binding with another oxygen atom to form O_2 and the hydrogen recombining to for H_2 (eq. 1; *US Department of Energy [DOE]*, 1993). Radiolysis involves several reaction pathways, some very complex, but we are only concerned with the overall, observable effects (Table 1).

$$2H_2O + \text{radiation} \leftrightarrow 2H_2 + O_2 \qquad (1)$$

1.3 Relevance of Research

Other planetary surfaces in our solar system do not teem with life like we see on Earth. However, we know almost nothing about life beneath the surfaces of other planets and we have only begun to explore life underground on Earth. Studies report microbes beneath the Earth's surface represent a large portion of total biomass (*Pedersen*, 1996) and yet little is understood about how these organisms live in these environments, that is, how they obtain their energy. Detrital organic material, derived from the surface, may be rare in this subsurface biosphere and its energy may be largely independent of photosynthesis. If so, the subsurface of water-rich planets, asteroids, and satellites might be home to a rich diversity of microorganisms; life on Mars may still exist, perhaps in water-bearing rocks below the surface.

Radioisotope	Natural Isotopic Abundance %	Primary Decay Modes
^{40}K	0.012	beta, EC, gamma
^{232}Th	100.00	alpha, beta, gamma
^{238}U	99.27	alpha, beta, gamma
^{235}U	0.72	alpha, beta, gamma

Table 1. The minor and major products from water radiolysis. (*Pastina & LaVerne*, 2001)

[1]Now at the University of Rhode Island

2. Data and Methods

2.1. Geologic Setting and Parameters

The numerical model was applied to four rock types, which represent a wide variety of physical parameters: granite, basalt, shale and ocean sediments (Table 2). Relative densities for each geologic medium were taken from Klein and Hurlburt (1977), all approximately 3.0 gcm^{-3}, it is assumed that the porewater has a density of 1.0 gcm^{-3}. In addition, both the low and high porosities for each rock/sediment type were included as physical factors, ranging from 0.0% in shale to 60.0% in ocean sediments (*Fetter*, 2001, *Domenico & Schwartz*, 1990; *Freeze & Cherry*, 1979). It was assumed that every pore was completely filled with water and that the rock/sediment is completely homogeneous, including the distribution of the radioisotopes, with the mineral grains and pores smaller than the traveling distance of an alpha particle (*Hofmann*, 1992).

2.2. Radiation Source

A number of naturally-occurring radionuclides are primordial, associated with the formation of the earth. The four primordial series of major interest for this project are the decay series: uranium, actinium, thorium and potassium. Uranium, Th and K are the main elements contributing to natural terrestrial radioactivity (*Plant et al.*, 1999). Uranium has two primary isotopes, ^{238}U and ^{235}U, that occur at the present time in the proportion of roughly 99.3% ^{238}U to 0.7% ^{235}U (*Roger & Adams*, 1969). Both have long and complex decay series, in contrast to Th which has only one relatively simple decay chain, from ^{232}Th. Secular equilibrium was assumed for the U and Th decay series. Of the three naturally-occurring isotopes of potassium (^{39}K, ^{40}K, and ^{41}K), only ^{40}K is radioactive; the respective isotopic abundances are 93.08, 0.012 and 6.9% (*Roger & Adams*, 1969). Radioactive potassium has two decay paths, where ^{40}Ca is the stable daughter of one and ^{40}Ar for the other. For two branches of decay for a daughter species, the energy value was obtained after multiplying by the fractional probability. The isotopes ^{238}U, ^{235}U, ^{232}Th and ^{40}K decay with half lives so long (ranging from $7.04x10^8$ yr for ^{235}U to 1.39×10^{10} yr for ^{232}Th) that significant amounts remain in the Earth in constant proportion. The average abundance of U, Th and K in the crust is 2.6 ppm, 10 ppm and 1% respectively (*Taylor & McLennan*, 1985), Table 2 details concentrations in representative rock types. At each decay step in the series, radiation is released primarily in the form of alpha particles, beta particles and/or gamma rays, with an associated energy release. Gamma radiation was not accounted for in these calculations for a two main reasons: 1) γ-rays emitted in the decay series are by-products of an alpha- or beta-particle and therefore the energies are highly variable (*Browne et al.*, 1978). 2) As outlined by Dubessy et al. (1988), γ-rays absorbed dose is much lower than α-particles. For fission products with more than one potential energy level release, that is a fraction of radioactive particle at varying energies, the primary decay was used with the corresponding energy emitted, taken from Aitken (1985).

2.3. Radiolysis of Porewater Numerical Model

The calculated hydrogen (H_2) yield is essentially the product of a given chemical radiation yield for a given species and the radiation dose absorbed in the porewater (eq. 3*a*; *Hofmann*, 1992). The H_2 production is represented by the variable "P_{H2}", the total hydrogen

Rock Type	Concentration Category	**Description**	**Radioisotopic Concentration (ppm)**			
			^{40}K	**^{232}Th**	**^{235}U**	**^{238}U**
Granite	Lower Limit (LL)	all	2.97	8.00	$1.58x10^{-2}$	2.18
	Mean (M)	>70% SiO2	4.09	$1.80x10^{+1}$	$2.88x10^{-2}$	3.97
	Upper Limit (UL)	Triassic & alkalic	4.96	$5.60x10^{+1}$	$1.08x10^{-1}$	$1.49x10^{+1}$
Basalt	LL	oceanic tholeiitic	$1.08x10^{-1}$	$1.80x10^{-1}$	$7.20x10^{-4}$	$9.93x10^{-2}$
	M	all	1.51	4.00	$3.82x10^{-3}$	$5.26x10^{-1}$
	UL	alkali	1.68	5.40	$7.13x10^{-3}$	$9.83x10^{-1}$
Shale	LL	red & yellow	$9.96x10^{-3}$	$1.00x10^{+1}$	$1.44x10^{-2}$	1.99
	M	gray & green	2.4	$1.20x10^{+1}$	$2.30x10^{-2}$	3.18
	UL	black	8.48	$1.31E^{+1}$	$1.44x10^{-1}$	$1.99x10^{+1}$
Ocean Sediments	LL	oozes & sand	$9.76x10^{-1}$	1.20	$5.33x10^{-3}$	$7.35x10^{-1}$
	M	siliceous/calcareous deep-sea sediment	1.29	5.50	$8.64x10^{-3}$	1.19
	UL	Argillaceous (clayey muds)	2.82	$3.00x10^{+1}$	$2.59x10^{-2}$	3.57

Table 2. (Data taken from *Wedepohl*, 1978) The four represented rock/sediment types are divided into classification classes based on radionuclide abundance.

yield (# H_2 molecules per second per gram of water). The escape or radiation chemical yield (G_{H2}=1.2) is a literature number for the amount of H_2 molecules produced per 100 eV in pure water from radiolysis by a 5 MeV helium ion (α- particle; *Pastina & LaVerne*, 2001). As Hofmann (1992) elaborates, the G-*value* is the source of largest uncertainty, and suggests that the true value, thus true yield, may be larger than expected.

$$\frac{A_x}{M_R} = \lambda_x \frac{N_x}{M_R} \quad (2)$$

The radionuclide activity per unit of representative rock was calculated using Eq. 2, where A_x/M_R is the mass normalized activity, λ_x is the decay constant in years and N_x/M_R is the number of atoms of the radionuclide per unit rock (*Spivack*, pers. comm). We calculated the radiation dose emitted from the rock (_T) by multiplying the mass normalized activity (_, atomsg^{-1}s^{-1}), determined using the radionuclide abundance in the representative rocks/sediment, by the sum of decay energies (E_ or E_) for each series to numerically model *in situ* H_2 production rates (eq. 3*b*; *Spivack & Hanks*, pers. comm.). Decay branches with less than 1% occurrence were omitted. If there are two branches of decay for a daughter species, the energy value was obtained after multiplying by the fractional probability. Total alpha energy emitted = total alpha energy absorbed (dose). Beta particles have a continuous spectrum of energies from zero to a maximum. The average energy is used instead (approx. 1/3 maximum). The mass stopping power (S_, S_) is a ratio between the ability for quartz (SiO_2, general mineral constituent in rocks) and water (H_2O) to stop a given radiation force (α- or β-particles; *Aitken*, 1985; *Hofmann*, 1992). This value is multiplied by the mass ratio of water to rock, derived from the porosity and density data (R=rock, w=water, ρ=density, ϕ=porosity; eq. 4). These equations assume a rock homogeneous in grain size (<30 μm), pore size (<30 μm), porosity and isotopic distribution, with every pore filled with water (ρ =1.0 g cm^{-3}; *Hofmann,* 1992). No fractures are considered in porosity except in granite-high porosity which pertains to a weathered granite with fractures. The final radiolytic hydrogen yield is per unit volume of water. The equation (eq. 3*b*) behaves with realistic limits: the yield stabilizes with low porosity (M_w/M_R =1) and if the system is completely water (M_w/M_R =0), then no radiolytic hydrogen is generated.

$$P_{H_2} = G_{H_2} \overline{D}T \quad (3a)$$

$$\overline{D}T = \left(\frac{\overline{A} \sum E_\alpha}{S_\alpha \frac{M_W}{M_R} + 1} \right)_\alpha + \left(\frac{\overline{A} \sum E_\beta}{S_\beta \frac{M_W}{M_R} + 1} \right)_\beta \quad (3b)$$

$$\frac{M_W}{M_R} = \frac{\rho_W}{\rho_R} \left(\frac{\phi}{1-\phi} \right) \quad (4)$$

3. Results and Discussion

3.1. Hydrogen Yields and Implications

Where appropriate mineralogic and physical conditions exist, H_2 production from the radiolysis of porewater is comparable to other metabolic-pathway activities. Figures *1a* and *1b* represent moles of hydrogen generated (log scale) in volcanic rocks (granite and basalt) and sedimentary species (shale and ocean sediment) respectively for a range of radioisotope concentrations and porosities. Total yields for ^{238}U, ^{235}U, ^{232}Th and ^{40}K were added together by concentrations classes, i.e. low with low, mean with mean, etc., because U, Th and K are large-ion elements that do not fit readily into the structures of main high-temperautre rock-forming minerals thus are compartmentalized into low temperature melts and become increasingly more concentrated together (*Rogers & Adams*, 1969). The third graph (Fig. 1*c*) corresponds to data from D'Hondt et al. (2002) on hydrogen equivalents of biological activity, measured by sulfate (SO_4^{2-}) reduction flux in deep sea sediments from various locations. Every one SO_4^{-2} can be used to oxidize four H_2. If granite and basalt met the models assumptions, then low porosity granite (6.41 x10^{-6} mols cm^{-2} yr^{-1}) and basalt (2.73 x10^{-7} mols cm^{-2} yr^{-1}) have hydrogen yields (Fig. 1*a*) greater than sulfate reduction rates at open-ocean sites (5.20 x10^{-8} mols cm^{-2} yr^{-1}) and roughly the same order of magnitude at ocean-margin sites (5.20 x 10^{-6} mols cm^{-2} yr^{-1}, Fig. 1*c*) where there is a great deal of organic material. It is unlikely that granite and basalt meet the homogeneous parameters because both are highly permeable due to large fractures. Only a small fraction of granites and basalts are hairline fractures that would support the conditions for the hydrogen yields calculated. Nevertheless, Pedersen (1996) found microbes living more than 800 m deep in granite formations and granite is one of the most abundant rocks of the continents. Low porosity granite is still one of the highest yielding rocks is (3.84x10^{-6} to 6.41 x10^{-6} mols cm^{-2} yr^{-1}), suggesting that radiolytic hydrogen might be a vital energy source for microbial residents of granite.

Radiolysis per unit water is more effective at low porosities for all rock/sediment types, except in the case of shale which had a low porosity of zero. Gross hydrogen from low porosity ocean sediments, ~1 to 4 x10^{-8} mols cm^{-2} yr^{-1}, is a few orders of magnitude less than low porosity granite and basalt, ~4 to 6 x10^{-6} and ~2 x10^{-7} respectively, due to lower concentrations of the radioisotopes. Nonetheless, low porosity, clay-rich ocean sediments yield hydrogen at rates equal to and greater than biological equivalent hydrogen yields measured by sulfate flux at open-ocean sites (low porosity o.s: ~1 x10^{-8} to 3 x 10^{-8} mols cm^{-2} yr^{-1} versus open-ocean rates of ~8 x 10^{-9} and ~1 x10^{-8} mols cm^{-2} yr^{-1}). Subsurface microorganisms in clay-dominated areas

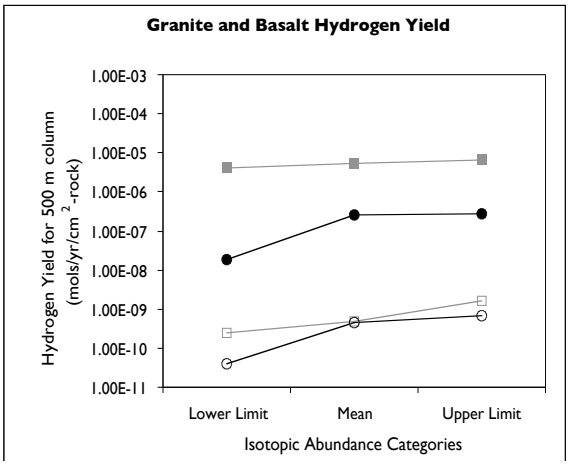

Fig. 1*a* The hydrogen yield for granite (squares) and basalt (circles) for both low (closed symbols) and high (open symbols) porosity.

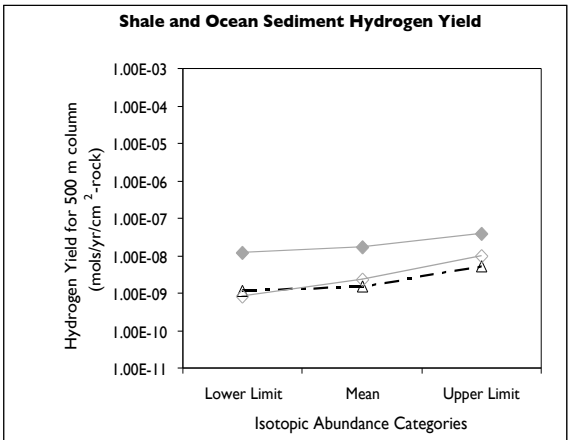

Fig. 1*b*. The hydrogen yield for shale (triangles) and ocean sediments (diamonds) for both low (closed symbols) and high (open symbols) porosity.

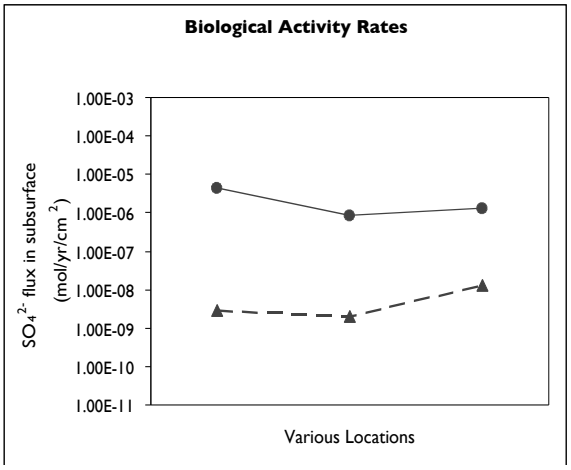

Fig. 1*c*. (Data taken from *D'Hondt et al.*, 2000) The biologic sulfate flux for granite (squares) and basalt (circles) for both low (closed symbols) and high (open symbols) porosity.

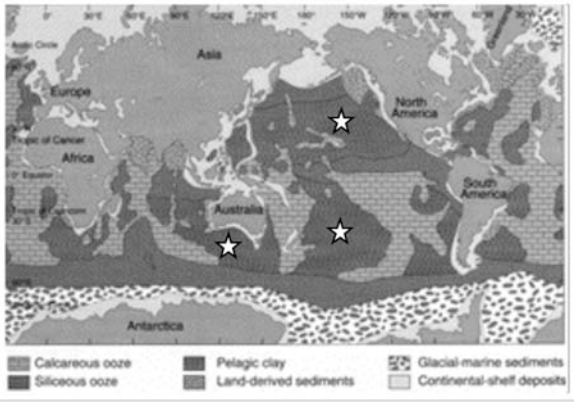

Figure 2. Sediment distribution in world's oceans. Stars show large open-ocean clay deposits (*Klement*, 1982).

highlighted on the map of global sediment distribution (Fig. 2), may rely more heavily on energy produced from radiolysis than that from organic material. Hydrogen generated from nuclear geochemistry has previously not been quantified or represented in a per unit water yield. These results show that rates have the capacity to solely support mircroorganisms.

3.2. Future Direction

Further calculations will strengthen this argument by accounting for heterogeneity in the rocks, including interactions along the rock-water interface, accounting for surface area of the minerals/grains and the radioisotope distribution along the boundary. Additional applications include expanding this to a regional scale, like the clayey substrates of the open-ocean, and the cosmic scale, like Mars. Radiolysis could be occurring at great depths on Mars, where high pressures and temperatures above 0˚ C restrict water to the liquid phase and there is the presence of cosmogenic radionuclides (K, Th, U), that might sustain a biosphere independently of photosynthesis.

4. Conclusions

An entire buried microbial biosphere may be supported by prevalent, radiolytic hydrogen production, where the system thrives independently of sunlight and photosynthetic products. H_2 production rates are indeed occurring at amounts that could sustain microbial communities and are comparable to and in some cases, exceed rates of other metabolic pathways. There are three main conclusions from this research: 1) In some environments radiolysis in porewater creates H_2 at rates comparable to metabolic utilization of SO_4^{2-}; 2) This process may become more important deeper in the substrate due to decreasing sulfate reduction rates with depth due to lack of organic matter; 3) In deep open-ocean (clay-rich) regions, radiolysis might be a more effective fuel source than photosynthetically-derived material. By understanding these extreme, bionutrient-limited systems on Earth, we may be able to apply these methods to other planets to assess their potential for subsurface life.

Acknowledgments. I want to thank Rob Pockalny and staff for providing the SURFO program. In addition, my mentors for providing an exciting research project and a learning experience.

References

Aitken, MJ. 1985. *Thermoluminescence Dating*. New York: Academic Press.

Browne, E, Dairiki, JM, Doebler, RE, Shibab-Eldin, A., Jardine, LJ, Tuli, JK, and Buyrn, AB. 1978. *Table of Isotopes* (7th ed.). New York: John Wiley & Sons, Inc.

D'Hondt, S, Rutherford, S, and Spivack, AJ. 2002. Metabolic activity of subsurface life in deep-sea sediments. *Science*, 295: 2067-2070.

Domenico, PA and Schwartz, FW. 1990. *Physical and Chemical Hydrogeology*. New York: John Wiley & Sons, Inc.

Dubessy, J, Pagel, M, Beny, J, Christensen, H, Hickel, B, Kosztolanyi, C, and Poty, B. 1988. Radiolysis evidenced by H_2-O_2 and H_2-bearing fluid inclusions in three uranium deposits. *Geochimica et Cosmochimica Acta*, 52:155-1167.

Fetter, CW. 2001. *Applied Hydrogeology* (4th ed.). New Jersey: Prentice-Hall Inc

Freeze, RA and Cherry, JA. 1979. *Groundwater*. New Jersey: Prentice-Hall, Inc

Hofmann, BA. 1992. Isolated reduction phenomena in red beds: A result of porewater radiolysis? *In* YK Kharaka and AS Maest (eds.), *Proceedings of the 7th Intl. Syposium on Water-Rock Interaction* (pp. 503-506). Vermont: A.A Balkema.

Kennett, JP. 1982. *Marine Geology*. New Jersey: Prentice-Hall, Inc.

Klein, C, and Hurlburt, C. 1977. *Manual of Mineralogy* (19th ed.). New York: John Wiley & Sons, Inc

Klement, AW. 1965. Natural Radionuclides in Foods and Food Source Materials. *In* E.B. Fowler (ed.), *Radioactive Fallout, Soils, Plants, Foods, Man*. (pp. 113-155). New York: Elsevier Publishing Co.

Onstott, TC, Moser, DP, Takai, K, Fredrickson, JK, Pfiffner, SM. and White, DC., 2000. Monitoring subsurface microbial activity, in situ, by instrumenting boreholes in ultradeep South African Au mines, *ASLO International Conference*, Copenhagen, Denmark, June, abstr.

Pastina, B and LaVerne, JA. 2001. Effect of molecular hydrogen on hydrogen peroxide in water radiolysis. *Journal of Physical Chemistry, A*, 105 (40): 9316-9322.

Pedersen, K. 1996. Microbial life in granite rock. Presented at the 1996 *Intl. Symposium on Subsurface Microbiology*. Davos, Switzerland.

Plant, JA, Simpson, PR, Smith, B and Windley, BF. 1999. Uranium Ore Deposits-Products of the Radioactive Earth *In* PC Burns and R Finch (eds.), *Uranium: Mineraology, Geochemistry and the Environment*. Mineralogical Society of America, vol. 38. 1999., Washington, DC. pp.255-319

Rogers, JJW and Adams, JAS. 1969. Geochemistry of uranium. *In* KH Wedepohl (ed.), *Handbook of Geochemistry*. (Vol. 2, 5), (pp. 92-E1 to 92-E5). Berlin: Springer-Verlag.

Taylor, SR and McLennan, SM. 1985. The *Continental Crust: its Composition and Evolution*. Oxford: Blackwell.

U.S. Department of Energy. 1993. DOE Fundamentals Handbook: Chemistry Vol. 2. (DOE-HDBK-1015/2-93). Washington, D.C: U.S. Government Printing Office.

Wedepohl, KH (ed.). 1969-1978. *Handbook of Geochemistry*. (Vols. 1-2). Berlin: Springer-Verlag.

Whitman, WB, Coleman, DC and Wiebe, WJ. 1998. Prokaryotes: The unseen majority. *Proceedings of the National Academy of Sciences of the United States of America*, 95: 6578-6583.

A new method for the extraction of microbes from sediments.

Kristofer D. Carlson[1], David C. Smith and Bruno Soffientino
Graduate School of Oceanography, University of Rhode Island, Narragansett, Rhode Island

Abstract. Current studies indicate that between 10 and 30% of the Earth's biomass resides within deeply buried sediments. Studies of these microbial communities focus on their species composition, total numbers, and activity. While effective methods exist for studying the composition and activity of such communities, current methods for studying the relative abundance of species or the total size and breadth of these communities are not satisfactory. In this paper we propose to modify an existing method of extraction—functional group recognition by activated microbeads-- to extract cells from sediment. Based on the assumption that cell membranes have sugars and glycoproteins on their surface, many of which include one or more cis-diols in their structures, we hypothesized that bacteria would bind to boronic-acid conjugated beads and be recovered by elution from the beads. To explore the feasibility of our new extraction method, we chose to use synthetic beads coated with n-aminophenylboronic acid (PBA) to extract microbes from a simple buffer system. Our model system for this technique works. By increasing the ratio of beads to bacteria in our model, we were able to achieve a 50% binding efficiency and a 23% elution efficiency (with respect to bound activity). In the process, we have developed a technique to label cells strongly enough to be seen at higher dilutions.

Introduction

There are large microbial communities living in deeply buried sediments. It has recently been estimated that 10-30 % of the Earth's biomass can be found living in these deeply buried sediments (Whitman et al, 1998; Parkes et al, 1994). Studying these communities is important to understand their effects on the geochemical cycling of carbon and other elements. These ecosystems could also be used as analogs for extraterrestrial environments. Studying these communities provides information about what types of microbes exist in them, how many there are, how diverse the populations are, and what niche each microbe occupies in the ecosystem.

DNA phylogenetic research provides one method for studying the microbial populations in the sediments. These studies inform us on the different types of bacteria present and their evolutionary relationship one another. They do not, however, provide information on the relative abundance of each species or the total number of the bacteria.

It has long been recognized that studying sediment and soil microbial communities would be facilitated by an efficient method of extracting cells from the surrounding medium. Several established methods for the extraction of bacteria from soils and sediments exist. The most common method for extraction is sonication (to loosen the cells from the matrix), and centrifugation, to separate sediments from microbes in solution. Estimates of the size of the communities are based largely on direct cell counts using acridine orange as a dye (Parkes et al., 2000). Bacteria often attach securely to soil and sediment particles, which makes them more difficult to see by blocking the dye's fluorescence, infringing on counting accuracy (Schallenburg et al, 1989). Using sonication for the removal of bacteria from the sediment matrix answers the problems of particles masking fluorescence for direct counting, but can kill cells, making accurate counts impossible (Tso and Taghon, 1997).

Other techniques for cell extraction from other media, such as food, involve antibodies linked to magnetic beads for the extraction of a specific organism. Some are used for the analysis of E. coli 0157:H7 levels in meats (Parham et al., 2002), but cannot be used to extract whole microbial communities. Based on this type of technique, using magnetic beads coated with antibodies, we chose to test a non-specific, bead-based extraction technique that targets structural similarities of microbial cells —the presence of sugars and glycoproteins on the cell wall.

Boronic acids react with cis-diols to form a diester. Since cis-diols are present in many sugars (e. g. mannitol, sorbitol, catechol (Barker et al., 1972; Springsteen and Wang, 2002), boronic acids have been used for the extraction and purification of sugars, and glycosylated hemoglobins by liquid column chromatography (Middle et al., 1982), as recognition molecules for saccharides, nucleotide transporters, and antibody mimics for cell-surface carbohydrates (Springsteen and Wang 2002).

Using boronic acid bound to acrylic beads, we plan to explore the feasibility of these reagents for bacterial extraction, and to establish the physicochemical conditions that affect the cell-bead binding process.

Materials and Methods

We used radiolabeled Escherichia coli as a means of rating the effectiveness of our method of extraction. The bacteria were labeled with 3H-Leucine before undergoing attachment. We compared the amount of activity in our samples after extraction and after elution to calculate the percent of successfully extracted bacteria from the solution.

Experimental Design

The basis for our experimentation was creating a simple and easily evaluated model for examining the

[1]Worcester Polytechnic Institute, Worcester, MA 01609

feasibility of using PBA coated beads as a means for extracting bacteria from sediments. Furthermore, we sought to establish which assay variables affect the binding and elution efficiencies. We examined pH and concentration of bacteria, because studies by Barker et al. (1973), Middle et al (1983), and Springsteen and Wang (2002) indicated that pH plays an important role in the reaction between boronic acids and cis-diols. The initial pH we chose was based on the work of Springsteen and Wang (2002), which supported previous research that a pH above the pKa of the boronic acid typically resulted in the most efficient binding. The boronate ester is more stable at pH levels near this point (Springsteen and Wang, 2002). The pKa of m-aminophenylboronic acid was estimated to be 7.8 from the pH of structurally related arylboronic acids for which literature values were available.

Preparation of Beads

Acrylic beads coated with m-Aminophenylboronic acid (Sigma) were used in this study, because of low cost and availability. Phosphate buffered saline (PBS), 0.1 M K2HPO4, pH 8.0 and chloramphenicol (5 µL, 20 mg/mL in methanol) was added to the dry beads, which were then allowed to incubate at 6°C overnight. The PBS was used because it has an ideal pH range (7.5-9.5) without containing any cis-diols. Ready-to-use, 300 µL aliquots of beads were transferred to 2-ml Eppendorf tubes, and stored at 6 °C until use.

Labeling the Culture

E. coli cells taken from an overnight culture in LB Broth (Difco) were labeled with 3H-Leucine. An aliquot (1 mL) of culture was centrifuged at 15,000 G for 10 minutes, the supernatant was poured off, and the culture was resuspended in clean LB broth (1mL). 200 µL of this culture was then added to 800 µL of LB broth and 7.50 µL 3H-l-leucine (40 nM final concentration; Perkin-Elmer, 173 Ci/mmol) in a 2 mL eppendorf tube. This was incubated for 1 hour at 37°C. The concentration of bacteria was reduced before incubation to give the cells a chance to reenter their log growth phase and incorporate the maximum amount of radiolabel into their cells.

This method was not effective for experiments requiring dilutions of more than 1:10, (overnight culture:PBS). An alternate method of labeling was developed: The pellet was resuspended in PBS with 10 mM glucose, and a 200 µL aliquot of this culture was then added to 800 µL of PBS with 10 mM glucose and 7.5 µL 3H-Leucine. This solution provided the E. coli with their minimal requirements. The bacteria were forced to use the radiolabeled Leucine as their only nitrogen source, and were labeled more intensely.

After incubation, the bacteria were rinsed twice via centrifugation and resuspension in PBS. Two washes eliminated most of the remaining unincorporated radiolabel from the suspension. This was confirmed by quantifying the radioactivity in a third wash. Finally, the pellet was resuspended in PBS with the growth inhibitor chloramphenicol (1 µL, 20 mg/mL in methanol), and an aliquot was scintillation-counted to determine the extent of radiolabeling.

Attachment and Elution

After the bacteria were labeled, they underwent attachment to the beads. To each prepared tube of beads in PBS, 100 µL of the labeled cell suspension was added. These tubes were incubated on a shaker for two hours at room temperature. The contents were mixed at a speed high enough to keep the beads in suspension, to allow for the greatest amount of bacteria-bead interaction.

After incubation, the supernatant was drawn off using a filtering pipette tip, and transferred to a scintillation vial for counting. The filtering tip was modified by gluing a piece of nitex filter (20 µm) to the cut end of a 1 mL micropipette tip. 20 µm filters were chosen to allow unattached bacteria to pass through with the supernatant, but keep the beads in the tube. It was important to draw as much fluid as possible from the sample to eliminate contamination of the eluate with the supernatant from the attachment.

Elution was conducted using PBS with a 100 mM concentration of sorbitol (per manufacturers recommendations). 400 µL of the PBS-sorbitol solution was added to each tube, before they were returned to the shaker to incubate for another two hours at room temperature. It was again important to keep the beads in suspension during this incubation to maximize interaction between the beads and the solution. Following elution, the supernatant was again extracted with the modified micropipette and placed in a scintillation vial, liquid scintillation cocktail (Scintiverse BD; Fisher) was added and the samples were counted in a liquid scintillation counter (Beckman Model 3801).

Calculations

We based our calculations of extraction and elution efficiency on the comparative levels of radioactivity in the samples. The total amount of radioactivity remaining in solution after the extraction was compared to the total amount of radioactivity in the initial culture. This percentage represented the amount of bacteria not attached to the beads (the Remainder) after extraction. The percent bound to the bacteria is represented by the difference between this and 100%, (Equation 1).

$$\%A_{Bound} = 100(1 - \frac{A_{\text{Re } mainder}}{A_{Total}}) \quad (1)$$

The amount of radioactivity in solution after both the extraction and the elution were completed was likewise compared to the total amount of radioactivity added initially, (Equation 2).

$$\%A_{Bound} = 100(1 - \frac{A_{\text{Re } mainder}}{A_{Total}}) \quad (2)$$

The ratio of the percent of the activity in the eluate to the percent of the activity in the bound bacteria

represents the percent of the attached bacteria that were released as part of the elution (Equation 3).

$$\%A_{Bound} = 100(1 - \frac{A_{\text{Re mainder}}}{A_{Total}}) \quad (3)$$

Results and Discussion

The bacteria were successfully extracted from solution by the aminophenylboronic acid beads. At the initial conditions of our experiments, (.4 mL total volume, pH 8.0, 100 µL culture at log growth concentration), an average of 39.9% of the bacteria in solution were extracted (Figure 1a). Of this fraction, 24.4% (9.8% of the total activity) was eluted from the beads.

Changing the concentration of the bacteria in each tube played a large role in changing the efficiency of the binding. As the dilution factor was increased from 1:1 (Figure 1a) to 1:1000 (Figure 1d), the average binding efficiency increased logarithmically (Figure 2).

The data exhibit wide margins of error, with points ranging from between up to 20% above and below the average (Figure 3).

Increasing the factor of dilution of the bacteria increases the binding efficiency. To achieve higher efficiencies by way of dilution would require further dilutions. Based on the logarithmic regression relating dilution and efficiency (Figure 2a), each 10% increase requires a further thousand-fold dilution (Table 1).

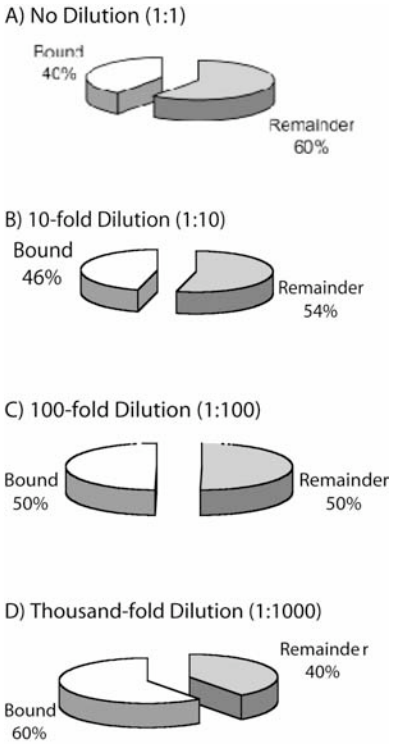

Figure 1. Fraction of bacteria bound with a) no dilution of the culture (1:1), b) a 10-fold dilution of the culture (10:1), c) a 100-fold dilution of the culture (100:1), and d) a 1000-fold dilution of the culture (1000:1).

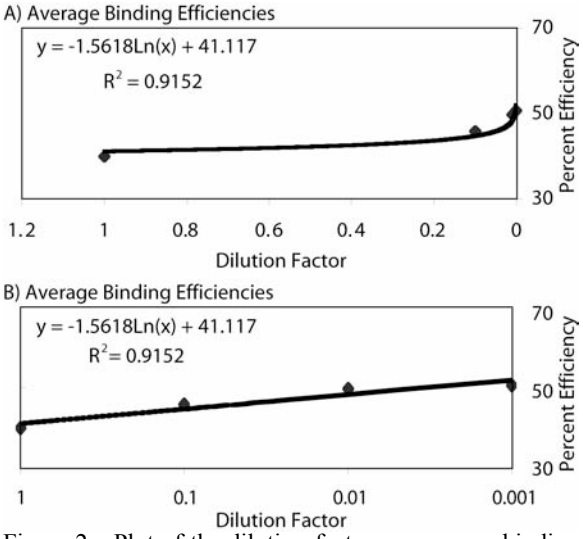

Figure 2a: Plot of the dilution factor vs. average binding efficiency; a) arithmetic scale and b)vlog scale.

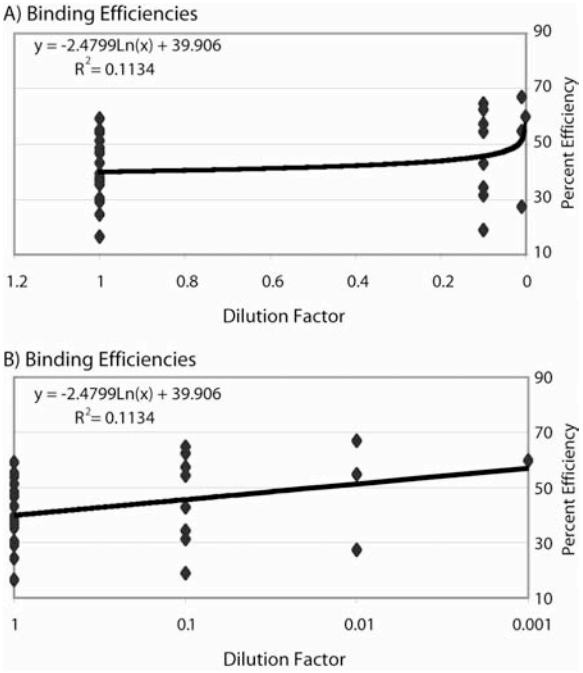

Figure 3a: Plot of the dilution factor vs. binding efficiencies; a) arithmetic scale and b) log scale.

Dilution Factor	% Bound
1.00x1000	41.12
1.00 x10-02	48.31
1.00 x10-03	51.91
1.00 x10-06	62.69
1.00 x10-09	73.48
1.00 x10-12	84.27
1.00 x10-15	95.06

Table 1. Characterizing the relationship of dilution factor and binding efficiency. Dilution factors upwards of 1.00x10^-15 would supply maximum efficiency.

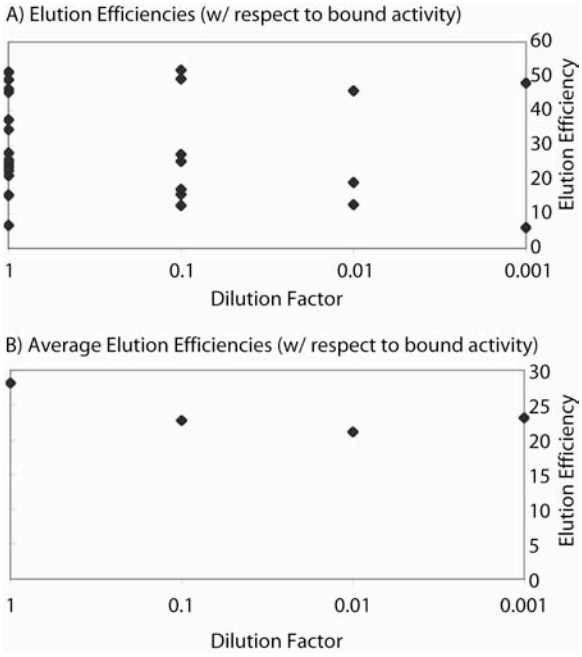

Figure 4. a) Plot of the dilution factor vs. elution efficiencies; log scale. b) Plot of the dilution factor vs. average elution efficiencies; log scale.

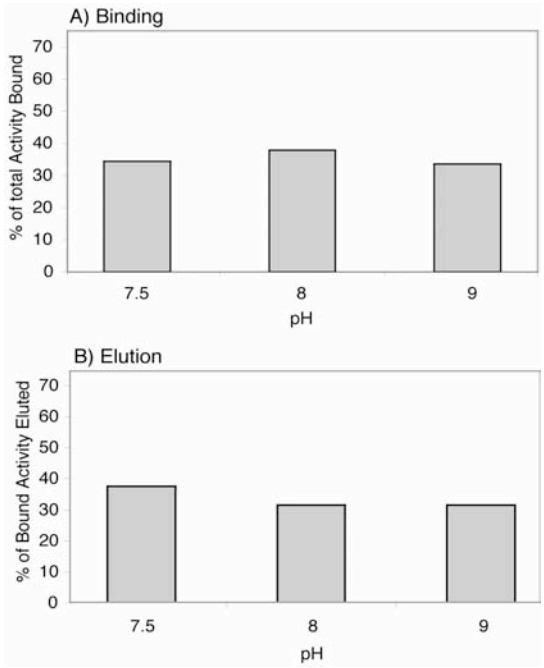

Figure 5. a) relationship between pH and binding efficiency. b) relationship between pH and elution efficiency (with respect to bound activity).

Dilution Factor	% Bound (Total Activity)	% Eluted (Bound Activity)	% Eluted
1	39.93	11.25	28.16
0.1	45.79	10.42	22.75
0.01	49.67	10.49	21.12
0.001	50.64	11.74	23.18

Table 2. Comparison of average binding efficiencies (% Bound), and elution efficiencies with respect to both total activity (% Eluted (Total)) and bound activity (% Eluted (Bound)).

	Bound	Eluted (Total)	Eluted (Bound)
1 M Sorbitol (tube a)	29.06	10.86	37.37
1 M Sorbitol (tube b)	16.51	8.47	51.30
100 mM Sorbitol	39.94	11.24	28.16

Table 3. Data relating the tubes with increased concentrations of sorbitol (1 M Sorbitol (a) and 1 M Sorbitol (b)) to those with normal concentrations of sorbitol (100 mM Sorbitol).

	Bound	Eluted (Total)	Eluted (Bound)	% Diff.
1 mL Tube (a)	37.23	8.83	23.72	28.40
1 mL Tube (b)	37.79	8.00	21.17	29.79
0.4 mL Tube Ave.	39.94	11.25	28.16	29.41

Table 4. Data concerning the effect of increasing the experimental volume of .4 mL to 1 mL.

Unlike binding, elution efficiencies were weakly affected by changes in the concentration of the bacteria (Figures 4a; 4b). When taken with respect to the amount of bound activity, the elution efficiencies varied between 21.1% (1:100 Dilution and 28.16% (1:1 Dilution) without any apparent trend following concentration (Table 2, Figures 4a; 4b). In an attempt to increase the efficiency of elution, a prepared solution of PBS (pH 8.0, .1 M) with 1 M Sorbitol was created to replace the elution buffer (PBS with 100 mM Sorbitol). The higher concentration of sorbitol displayed an increase in elution efficiency of 9.21% and 23.14% (Table 3), but was not implemented during the study.

Based on the results of studies by Barker et al. (1973), Middle et al (1983) and Springsteen and Wang (2002), which showed dramatic changes in efficiency with small changes in pH, we expected this parameter to have an impact on the efficiency of the binding reaction. Our data do not indicate pH as an important variable of either our binding reaction (Figure 5a), or our elution reaction (Figure 5b), at least with the PBS buffer used in this work.

In this research, the calculated radioisotope mass-balance (the sum of the Remainder activity and the Elution activity) numbers did not add up to the total amount of activity initially added to each tube. In the samples, there was an average of 28.31% difference, with minimum values at 5.59% and maximum values at 50.00%. This loss of this activity is significant with respect to the validity of this research because by the above calculation processes, we have included this activity as the bound activity. In an attempt to improve recovery of radioactivity, we increased the total volume

of the tubes to 1 mL from 0.4 mL (Table 4). If the loss of activity occurred during the transfer of the supernatants, it stands to reason that a larger volume would be affected to a lesser extent than a smaller volume. There was no decrease in the difference between the mass balance and the total measured radioactivity in the tubes, indicating that the methods used to pipette the supernatant from the tubes were effective.

In one experiment, the beads were counted in the scintillation counter after elution. The activity left on the beads should have been representative of the bacteria not eluted by the elution buffer. In these experiments, 50 - 75% of the initial activity was left on the beads after elution. This confirms other data that only a fraction of the bacteria are eluted, but implicates a higher elution rate than that calculated from the remainder activity. It also explains the discrepancy between the total activity in the culture and the activity represented by the mass balance. Activity remaining on the beads was measured neither in the remainder nor in the elution, and would be part of the missing activity.

Conclusions

The procedure of extracting bacteria from a solution or sediment is feasible. Our method works acceptably well in a simple system using a single buffer and a single bacterium. A sediment slurry is a much more complex system than a phosphate buffer system and could introduce inhibitors to the binding process. Additionally, to confirm the hypothesis that this method of extraction is non-specific, further experimentation needs to include a wider variety of bacteria. Important groups to consider when expanding this technique include archaea as well as bacteria, and dormant cells as well as active cells. Some of the bacteria and archaea living in deeply buried sediments lie dormant or metabolize very slowly. Many of these organisms are adapted for metabolic rates up to five orders of magnitude lower than those at Earth's surface (D'Hondt et al., 2002). If these microbes change the structure of their cell membranes and walls in order to reach these slow rates of metabolism or be fully dormant, the procedure might only extract more active cells from the sediments.

Higher factors of dilution increase binding efficiencies. To achieve the best efficiencies require still further dilutions. Each 10% increase requires a thousand-fold further dilution (Table 1). Other ways of increasing efficiency of extraction might be found in the exploration of other assay variables including other buffers and ionic strength. The research of Middle et al. described the optimizing effect of divalent cations on the binding of a boronic acid to hemoglobins (1983). When we tried to incorporate $MgCl_2$ into our own assay, the result was a precipitate $Mg_3(PO_4)_2$. In another buffer such as taurine, this addition would be possible and could impact the binding very favorably.

The most challenging part of achieving dilutions of a thousand-fold or greater was labeling the cells strongly enough to be counted at that low number, and therefore improvements in the labeling method are necessary for further research in this extraction technique. The approach that seemed to work approximately down to 1:1000 dilution involved growing E. coli on a minimal medium of PBS, 10 mM glucose and 40 nM radiolabeled Leucine. The combination of these resources provided the growing bacteria with only one source of nitrogen—the Leucine—and forced them to take in the labeled amino acid to a greater extent than normal in order to grow and reproduce. The amount of label incorporated into the cells was also dependent on time. An incubation period of 2.5 hours at 37^{o}C provided a bacteria culture labeled at 300,000 DPM. For dilutions of more than 10-3, even stronger labeling would be necessary. A label with higher specific activity used the same way could achieve this.

The efficiencies of the elution procedure were generally very low. Conducting an extraction procedure where between 25 and 30% of the bound cells are eluted is not very efficient. Ideally, all of the bacteria on the beads would be eluted, but further research needs to be conducted to reach this point. Exploring higher concentrations of sorbitol in elution buffers, or using other sugars containing cis-diols as the elution agent would be well-reasoned explorations. A tenfold increase in sorbitol produced a noticeable increase in elution efficiency, (Table 3); it stands to reason that further increases in the concentration of a cis-diol bearing elution agent would increase the elution reaction. Another feasible method for increasing overall elution efficiencies would be to conduct the elution more than once, replacing used elution buffer with new buffer.

Acknowledgments. I would like to thank Steve D'Hondt and Art Spivack for their support and assistance. I am grateful to Rob Pockalny for coordinating the 2004 SURFO program with assistance Rich Viso, Rhonda Kenny and Kim Carey.

References

Barker, S. A., A. K. Chopra, B. W. Hatt and P. J. Somers. 1973. The Interaction of Areneboronic Acids with Monosaccharides. Carbohydrate Research. 26:33-40.

D'Hondt, Steven, Scott Rutherford, Arthur J. Spivack. 2002. Metabolic Activity of Subsurface Life in Deep-Sea Sediments. Science. 295:2067-2070.

Middle, Fiona, Ann Bannister, Alastair J. Bellingham and Peter D. G. Dean. 1983. Separation of glycosylated haemoglobins using immobilized phenylboronic acid. Biochem. J. 209:771-779.

Parham, Nick, Janice Spencer, David Taylor, Helen Ternent, Giles Innocent, Dominic Mellor, Mark Roberts and Alun Williams. 2002. An adapted ImmunoMagic cell Separation method for use in quantification of Escherichia coli O157:H7 from bovine faeces. J. Microbiol. Meth. 53:1-9.

Parkes, R. John, Barry A. Cragg, Bale, S. J., Getliff, J. M., Goodman, K., Rochelle, P. A., Fry, J. C., Weightman, A. J., Harvey, S. M. 1994. Deep bacterial biosphere in Pacific Ocean sediments. Nature. 371:410-413

Parkes, R. John, Barry A. Cragg, Peter Wellsbury. 2000. Recent studies on bacterial populations and processes in subseafloor sediments: a review. Appl. Environmental Microbiol.. 55:1214-1219.

Schallenburg, Marc, Jacob Kalff and Joseph B. Rasmussen. 1989. Solutions to Problems in Enumerating Sediment Bacteria by Direct Counts. Hydrogeology Journal. 8:11-28.

Springsteen, Greg and Binghe Wang. 2002. A detailed examination of boronic acid-diol complexation. Tetrahedron. 58:5291-5300.

Tso, S. F. and G. L. Taghon. 1997. Enumeration of Protozoa and Bacteria in Muddy Sediment. Microb. Ecol. 33:144-148.

Whitman, William B., David C. Coleman and William J. Wiebe. 1998. Prokaryotes: The unseen majority. Proc. Natl. Acad. Sci. USA. 95:6578-6583.

K. D. Carlson, D. C. Smith and B. Soffientino, Graduate School of Oceanography, Univeristy of Rhode Island, Narragansett, RI 02882. (perrin@wpi.edu, dcsmith@gso.uri.edu, bruno@gso.uri.edu)

Copyright 2004 by the Graduate School of Oceanography/University of Rhode Island, SURFO program.

Effect of air-sea surface fluxes in the GFDL hurricane prediction system

Sam Kelly,[1] Isaac Ginis, Biju Thomas, and Il-Ju Moon
Graduate School of Oceanography, University of Rhode Island, Narragansett, Rhode Island

Abstract. The Geophysical Fluid Dynamics Laboratory (GFDL) hurricane prediction system has been in use by the National Weather Service since 1995. While the model consistently produces accurate track predictions, it often under-estimates wind speed in intense hurricanes. In order to achieve better intensity predictions new ways of calculating air-sea surface fluxes must be examined. One parameter that may be re-examined is the drag coefficient (C_D). The current version of the GFDL model uses a drag coefficient function that increases linearly with wind speed. This formula was derived from extrapolations of C_D at wind speeds much lower than those present in hurricanes (less than 30 m s^{-1}). Recent observations, numerical experiments, and theory have shown that C_D remains constant or decreases in hurricane strength winds. A second parameter that may be re-examined is the ratio of the heat coefficient (C_H) to C_D. Although this ratio has been shown to be important in determining hurricane intensity it has not been well defined. This paper discuses the results of sensitivity experiments conducted with the GFDL model during forecasts of Hurricane Isabel (2003). In these experiments the ratio of C_H / C_D is varied and the calculation of C_D is modified for high wind speed conditions. It is found that capping the value of C_D for winds above 35 m s^{-1} and using a larger ratio of C_H/C_D produces a more intense hurricane and a significantly better intensity prediction of Hurricane Isabel.

Introduction

Heat and momentum transfer between the sea surface and atmosphere are important in determining tropical cyclone intensity (Emanuel 1986). Hurricanes lose momentum through the creation of waves, breaking of waves, and creation of surface currents (Csanady 2001). In addition to momentum transfer, latent and sensible heat fluxes are important in providing a hurricane with a warm humid core. It is well known that hurricanes are created above warm water and typically lose intensity over cold water and land.

The GFDL hurricane prediction system, like most operation models, determines momentum flux using a drag coefficient (C_D) that increases linearly with wind speed. Recent studies suggest that this parameterization is inaccurate because the drag coefficient begins to level off or decrease in winds above 35m s^{-1}. Specifically, this idea is supported by (1) drag coefficients estimated from analysis of GPS sonde data from various hurricanes (Powell et al. 2003), (2) laboratory experiments at the University of Miami in winds up to 50 m s^{-1} (Donelan et al. 2004), and (3) simulations using a coupled wave-wind model (CWW) (Moon et al 2004a, b, c). Moon et al. (2004c) simulated actual hurricane winds in the CWW model using the same wind initialization model as the GFDL hurricane prediction system. The CWW model showed a decrease of the drag coefficient in high winds, directly opposing the calculation of the drag coefficient in the current GFDL model. This paper examines the sensitivity of the GFDL model to the parameterization of the drag coefficient.

In the GFDL model the heat coefficient (C_H), which is used to calculate sensible and latent heat flux, is derived from the parameterization of C_D. While in general the relationship between C_D and C_H is highly debated and loosely defined (especially in conjunction with the new parameterization of C_D) it has been shown to be important. In particular, hurricane intensity has been linked to the ratio of the heat coefficient to the drag coefficient (C_H / C_D) (Ooyama 1969; Emanuel 1986). Emanuel (1986) related a hurricane to a Carnot heat engine and showed that as C_H / C_D increases so should hurricane intensity. This theory has been tested in a variety of models (Emanuel 1999; Bao 2001) but its influence on the GFDL model has not been documented. In order to examine the possible effects of different drag coefficient parameterizations the ratio of C_H / C_D must first be understood.

In this paper, the sensitivity of the GFDL model to new surface flux parameterizations is examined by (1) testing several ratios of C_H / C_D and (2) capping C_D when the wind speed exceeds 35 m s^{-1}. All the experiments are conducted by making forecasts of Hurricane Isabel (2003).

The GFDL hurricane model

The model used in this study is the GFDL hurricane forecast system. The GFDL model is a primitive equation atmospheric model that has been developing since the 1970's in the NOAA Geophysical Fluid Dynamic Laboratory. The National Weather Service has used it since 1995 for operational hurricane forecasting. Major features of the model are given by Kurihara et al. (1998). The model has 42 vertical sigma layers and a doubly nested square grid. The inner grid follows the center of the hurricane and has a grid spacing of 1/6 of a degree. When forecasting a hurricane several observed parameters including wind speed, pressure, and location are used to initialize the model. Using these parameters a hurricane vortex is created in a process known as "bogusing". This process, which involves generation of a hurricane vortex through a controlled spin-up process using the prediction model, is described in detail by Kurihara et al. (1993). In order to initialize the hurricane vortex for

[1]Now at Carleton College, Northfield, MN 55057

our experiments, the observed values of wind speed, pressure, and track were obtained from the National Weather Service. Because there is an adjustment period after the bogused vortex is created, the results of the experiments sometimes show a large pressure and wind fluctuation in the first 8-12 hours.

Hurricane Isabel (2003)

Tropical depression Isabel originated off the coast of Africa as a tropical depression on 1 September. The storm moved northwestward and intensified to hurricane status on 7 September. On 10 September it turned westward on a course it would follow for several days. All of the GFDL model forecasts were initialized at 00Z 11 September. During 11 September Isabel reached Category 5 on the Saffir-Simpson scale with maximum winds of 75 m s^{-1}. Over the next four days it had consistently had an eye of 65-85 km in diameter. Isabel eventually turned northward and made landfall on 18 September near Drum Inlet, North Carolina. By landfall Isabel had weakened to a Category 2 hurricane. It was directly responsible for 16 deaths and approximately $3.37 billion dollars in damage (Beven and Cobb 2003).

Hurricane Isabel was forecasted at the National Hurricane Center (NHC) using a variety of computer models. Among the models that predicted storm track the average track error was 73 km for a 24-hour forecast. Among the models that predicted maximum wind speed the average error for a 24-hour forecast was 6 m s^{-1}. One of the major contributors to this error was an under-forecast of Isabel's rapid intensification (Beven and Cobb 2003).

Experimental Design

In order to examine the effects of changing the surface flux parameters, several experiments were conducted (Table 1). The control run was conducted using the current GFDL model parameterization. The initial time of the forecast is 11 September at 00 Z. In this parameterization the drag coefficient is calculated according to the classic Charnock relation (Charnock 1955):

$$C_D = \frac{\kappa^2}{\ln\left(z / \beta_* u_*^2 / g\right)^2} \quad (1)$$

where z is height above the sea surface, κ is the Karman constant, β_* is a constant equal to 0.0185, u_* is friction velocity, g is gravity, and the quantity $\beta_* u_*^2 / g$ is known as roughness length (z_0). The momentum flux, sensible heat flux, and latent heat flux are defined respectively as follows:

$$\tau = \rho C_D U_{10}^2 \quad (2)$$

$$H_s = \rho c_p C_H U_{10} T_{10} \quad (3)$$

$$H_l = \rho L_v C_H U_{10} q_{10} \quad (4)$$

where U_{10} is the 10-m wind speed, ρ is the density of air, T_{10} is the 10-m temperature, q_{10} is the 10-m water vapor mixing ratio, and c_p and L_v are the specific heat capacity and latent heat of vaporization, respectively. In the current GFDL model C_D increases virtually linearly with wind speed (Figure 1b). The ratio of C_H / C_D used in the current GFDL model is ~1.0 for very low wind speeds (less then 5 m s^{-1}). In moderate to high wind speeds the ratio drops to ~0.85 and becomes nearly constant (Figure 1a). In order to examine the effects of different C_H / C_D ratios several experiments were run using values of 0.7, 1.1, and 1.2 (Figure 1a). These experiments are labeled Exp. 1, Exp. 2, and Exp. 3, respectively.

In order to examine the effects of a parameterization of C_D that does not increase linearly in high winds two additional experiments were run. In Exp. 4 the original GFDL ratio for C_H / C_D was used, however the surface drag was kept at the value for 35 ms^{-1} for all wind speeds above 35 ms^{-1}. "Capping" C_D also caused C_H to keep its value for 35 ms^{-1} for all wind speeds above 35 ms^{-1}. In Exp. 5 the same parameterization for C_D was used however the ratio used for C_H / C_D was 1.2. The coefficients for these experiments are shown in Figures 1b-1d. All experiments were run for 24 hours except the control and Exp. 6, which were run for 55 hours.

Results and discussion

Intensity

Output of minimum pressure and maximum wind were compared for all the experiments to determine forecast intensity. By examining the pressure versus time graph (Figure 2a) it became evident from experiments 1 through 3 that changing the ratio of C_H / C_D had a notable effect on the intensity. The lower ratio of C_H / C_D = 0.7 showed a considerable increase in pressure (decrease in intensity) while the increased ratios produced lower pressures. The ratio of 1.2 seemed to agree best with the observations. Examining Exp. 4 where C_D has been capped and the ratio of C_H / C_D was the same as in the original GFDL model displayed an increase in minimum pressure, i.e. loss in hurricane intensity (Figure 2b). This was determined to be due to the subsequent capping of C_H and reduction of the air-sea heat flux. An increase of the C_H / C_D ratio to 1.2 in Exp. 5 led to a more intense hurricane and significantly better forecast in terms of better agreement between the simulated and observed minimum pressure (Figure 3b).

Table 1: Experimental Design

Experiment	C_D	C_D / C_H
Control	Current GFDL model	Current GFDL model
Exp. 1	Current GFDL model	0.7
Exp. 2	Current GFDL model	1.1
Exp. 3	Current GFDL model	1.2
Exp. 4	Capped at 35 m/s	Current GFDL model
Exp. 5	Capped at 35 m/s	1. 2

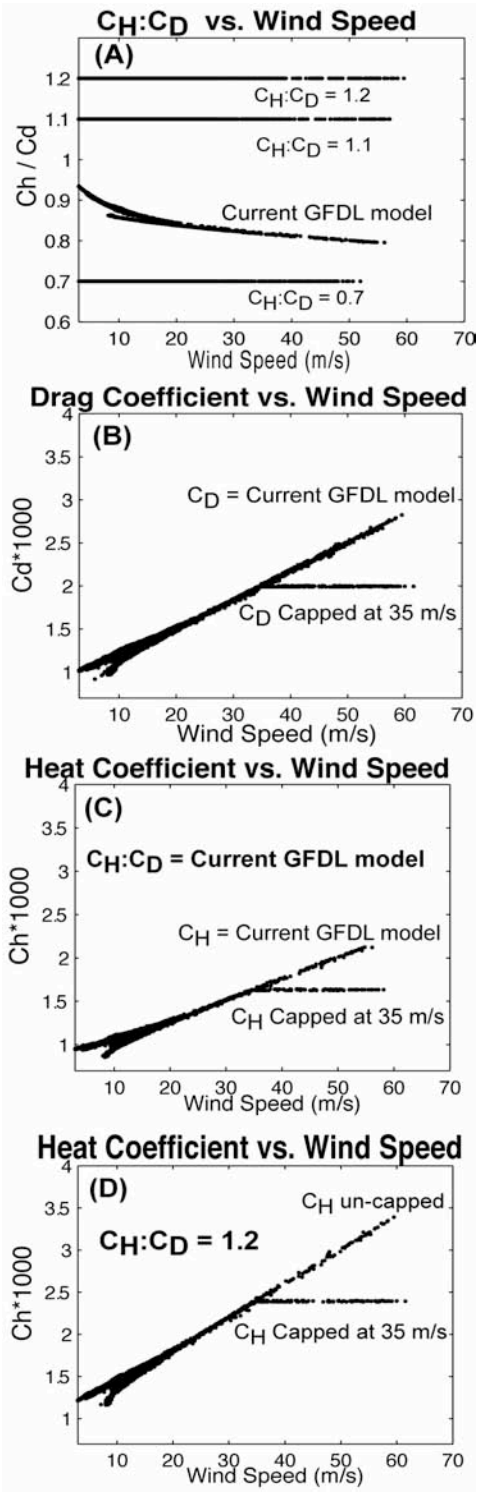

Figure 1. (A) Ratio of heat coefficient versus wind speed for the control, Exp. 1 (C_H :C_D = 0.7), Exp. 2 (C_H :C_D = 1.1), and Exp. 3 (C_H :C_D = 1.2). (B) The drag coefficient versus wind speed with the current GFDL model Charnock formula (Exp. 1-3) and with C_D capped at 35 ms^{-1} (Exp. 4 and 5). (C) The heat coefficient versus wind speed with current GFDL model C_H to C_D ratio and C_D either uncapped (control) or capped (Exp. 4). (D) The heat coefficient versus wind speed with C_H :C_D = 1.2 and C_D either uncapped (Exp. 3) or capped (Exp. 5).

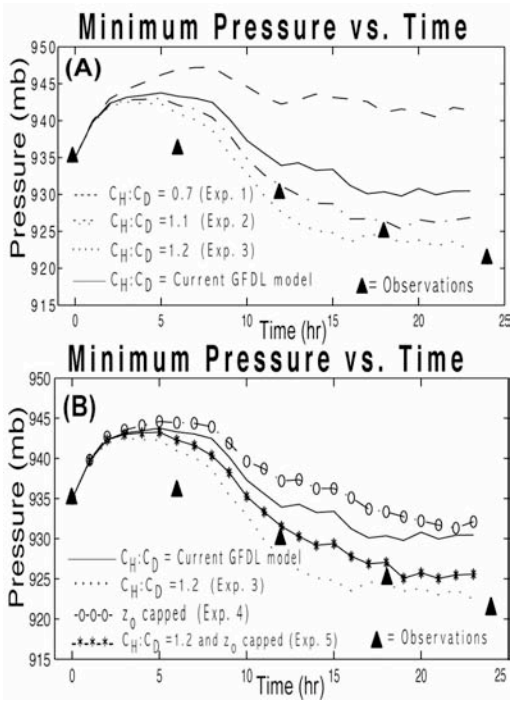

Figure 2. (A) Minimum pressure versus time for several different C_H to C_D ratios. Triangles represent National Weather Service observations. (B) Comparison of minimum pressure versus time for the two experiments with C_D capped at 35 ms^{-1} (Exp. 4 and 5) and their uncapped equivalents (control and Exp. 3).

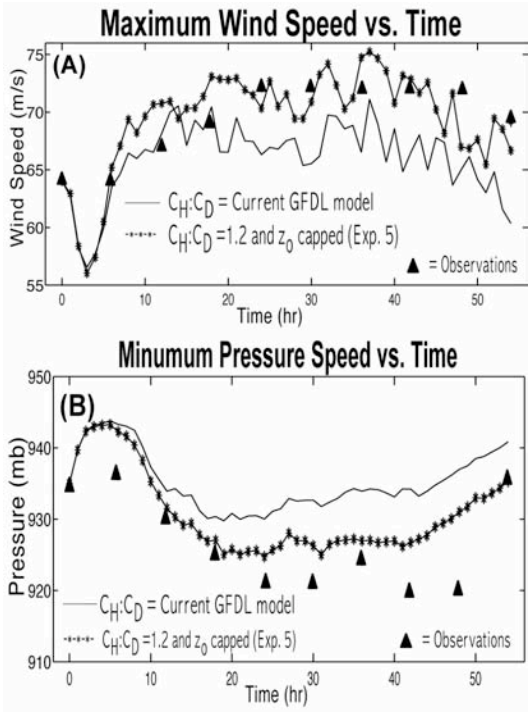

Figure 3. (A) Maximum wind speed versus time for several different C_H to C_D ratios. Triangles represent National Weather Service observations. (B) Comparison of the maximum wind speed versus time for the two experiments with C_D capped at 35 ms^{-1} (Exp. 4 and 5) and their uncapped equivalents (control and Exp. 3).

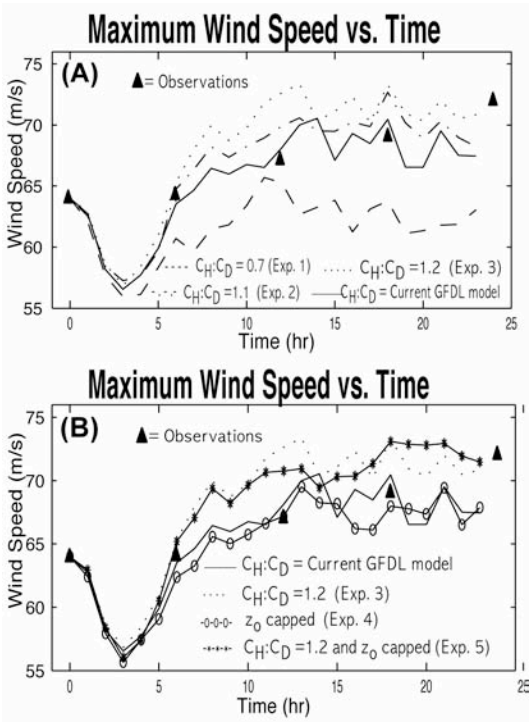

Figure 4. (A) Maximum wind speed versus time for control and Exp. 5 over a 55-hour forecast. Triangles represent National Weather Service observations. (B) Comparison of the maximum wind speed versus. time for control and Exp. 5 over a 55-hour forecast.

By examining the maximum wind versus time graph over the first 24 hours (Figure 4a) it is shown that the wind speed depends on the C_H / C_D ratio. The experiments with higher ratios produce greater winds. The graph also displays that by capping C_D (Exp. 4 and 5) there is a slight decrease in wind speed (Figure 4b). It is seen however that capping C_D has a more pronounced effect on the hurricane pressure. In several instances, such as certain points between 18 to 24 hours, the experiments where C_D has been capped actually produce higher maximum winds than their uncapped equivalents. While lower winds in Exp. 4 and 5 can once again be explained by the capping of C_H and subsequent reduction in heat flux, the instances where they produce higher winds may be explained by a decrease in momentum flux displayed in Figure 5 and discussed in section 5c.

In the first 20 hours of the forecast it appears that the experiments with the increased C_H / C_D ratio overestimate how quickly the hurricane will intensify. However, in the longer-range forecast (Figure 3a) it is evident that the wind is more accurately modeled by the new surface fluxes.

Structure

In order to examine the effect of surface fluxes on the hurricane vertical structure, wind profiles were sampled in Exp. 5 and the control run at forecast hour 36, 42, 48, and 54. In order to avoid individual fluctuations the ten points of highest wind were selected at the sea-surface

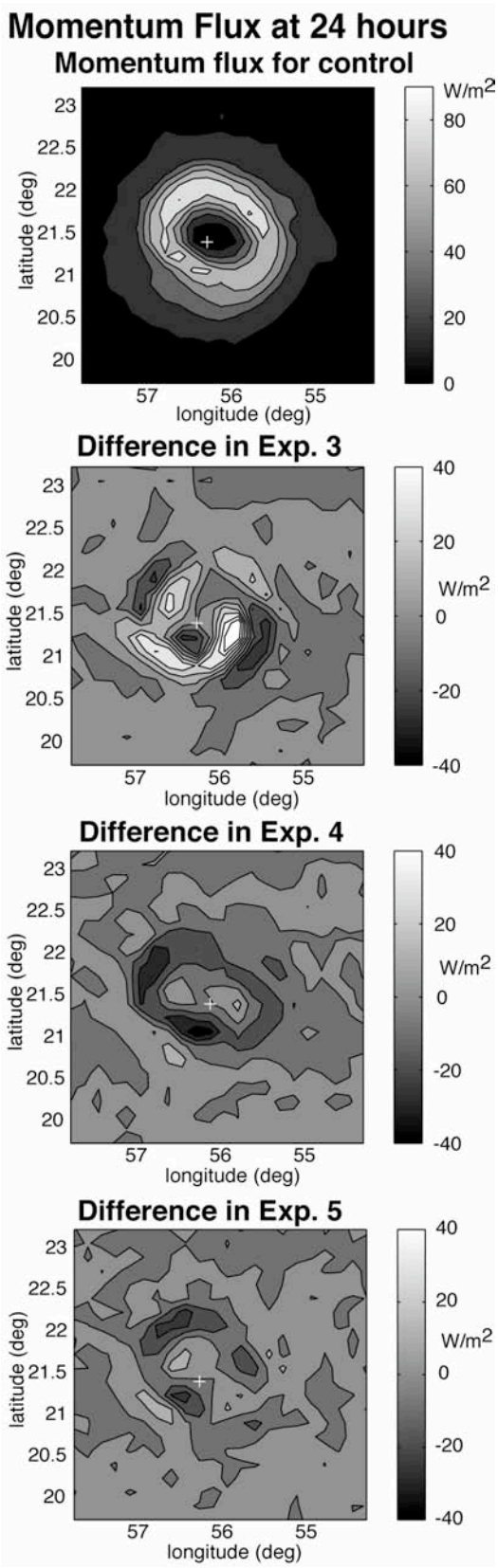

Figure 5. Altitude versus wind speed for control and Exp. 5 at 36, 42, 48, and 54 hours. Profiles are generated by averaging the profiles of the ten grid points with highest surface wind.

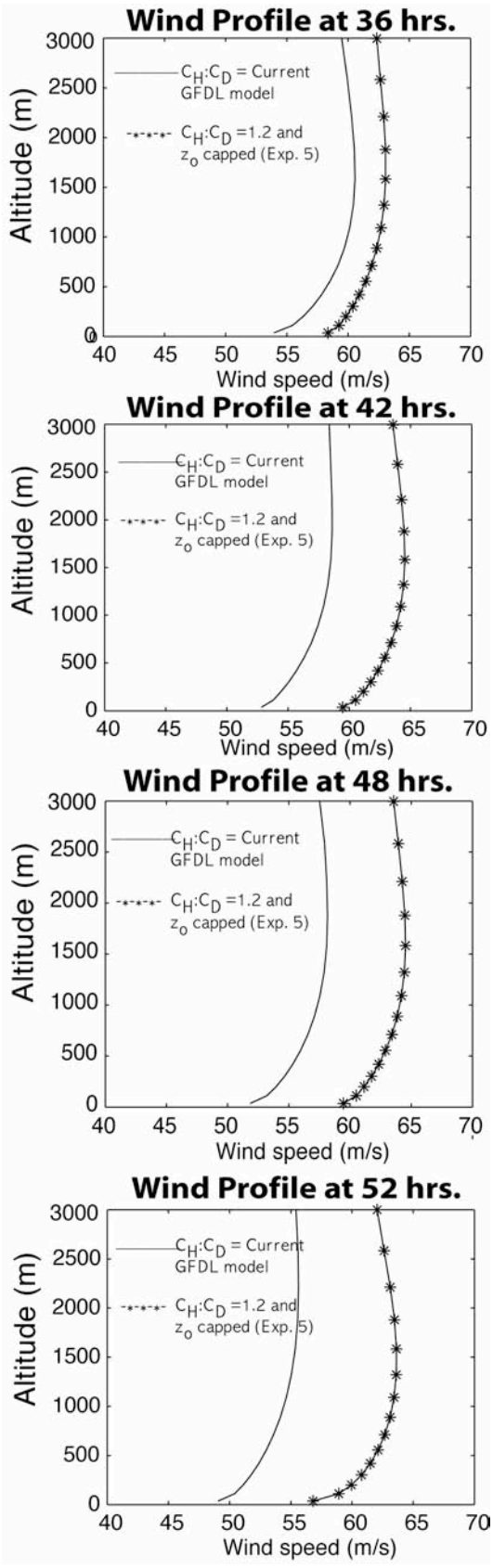

Figure 6. Momentum flux at 24 hours and the change in momentum flux for Exp. 3, Exp. 4 and Exp. 5. For the difference plots a positive value indicates an increase in flux.

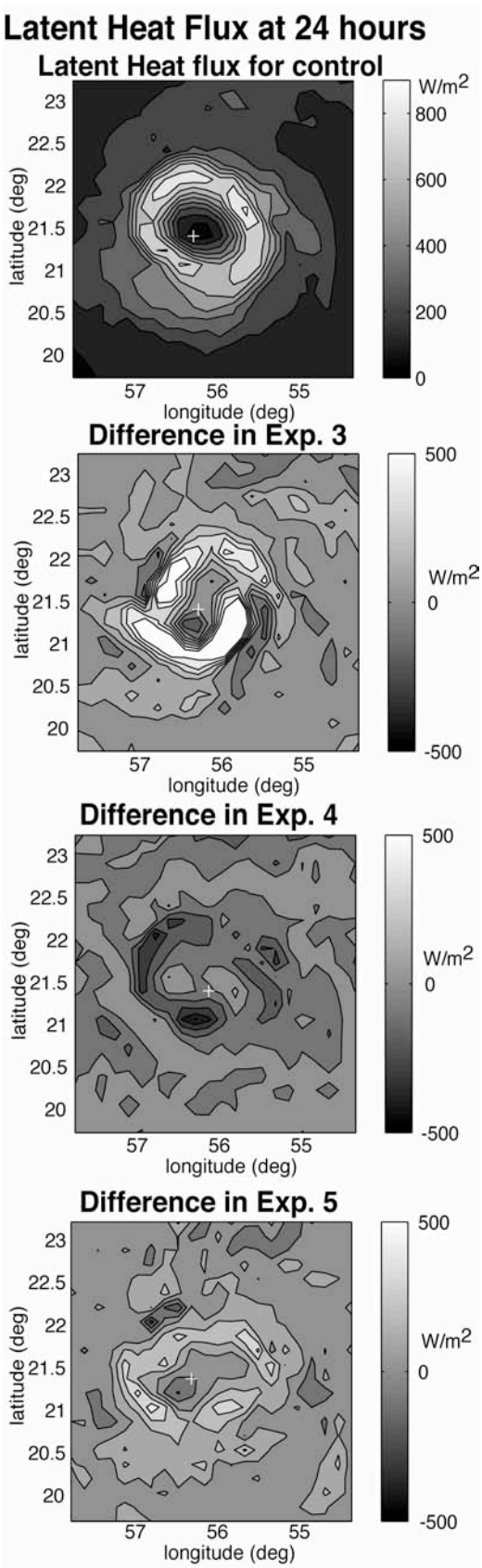

Figure 7. Latent heat flux at 24 hours and the change in latent heat flux for Exp. 3, Exp. 4 and Exp. 5. For the difference plots a positive value indicates an increase in flux.

and the associated wind profiles were averaged up to 3 km (Figure 6). In all cases Exp. 5 had a greater wind speed than the control run from the surface to 3 km. This result supports the hypothesis that the surface fluxes have a structural impact on the hurricane extending into the atmospheric boundary layer.

Momentum and heat fluxes

Snap shots were taken of the momentum and heat fluxes at the sea surface for Exp. 3, Exp. 4, Exp. 5, and the control run at forecast hour 24. Figures 5 and 7 display contour plots of the change in momentum and heat flux, respectively, from the control. Figure 5 reveals that near the eye wall Exp. 4 and 5 (where C_D has been capped) have less momentum flux than the control run. In Exp. 3, where $C_H / C_D = 1.2$ and C_D is not capped, there is a significant increase in momentum flux compared to the control run. This result can be explained by an increased heat flux, which is causing higher winds.

While the momentum flux is decreased by capping the drag coefficient, it must be noted that the heat flux is larger than the momentum flux and consequently has a larger effect on the intensity of the hurricane. In the GFDL model C_H is used to calculate both the sensible and the latent heat flux. Although both fluxes show similar trends the latent heat flux is several times larger, so only the latent heat flux is shown and discussed in this paper (Figure 7). In Exp. 3 there is a significant increase in latent heat flux over the control run. This result is due to the increased C_H / C_D ratio. In Exp. 4 where the ratio is the same, there is a significant loss in heat flux due to the capping of C_H. In Exp. 5 where the increased C_H / C_D ratio is combined with a capped C_H there is still a net increase in latent heat flux compared to the control run.

Track

The parameterization of the surfaces fluxes was found to have very little impact on hurricane track. The error in track for the 24-hour control run was 55 km, which was better than the NHC model average 24-hour forecast error during Hurricane Isabel, which was 73 km (Beven and Cobb 2003). Throughout all the 24-hour experiments the increase or decrease in track error did not exceed 4%. These results suggest that the GFDL model's track prediction is not sensitive to surface flux parameterization.

Summary and Conclusions

Recent research has shown that surface flux parameterization used in the current version of the GFDL model needs to be improved for high wind speed conditions. Several experiments were conducted to investigate the sensitivity of the GFDL model under new parameterizations of surface fluxes. The GFDL model clearly displayed sensitivity to both the C_H / C_D ratio and the capping of C_D in winds above 35 ms^{-1}. Increasing the ratio of C_H / C_D caused a decrease in minimum pressure and an increase in maximum wind speed. Capping the value of C_D in high winds caused a considerable increase in minimum pressure but only a slight decrease in wind speed. A ratio of 1.2 with C_D capped produced a more accurate forecast of Hurricane Isabel.

References

Bao J.-W., S. A. Michelson, and J. M. Wilczak, 2001: Sensitivity of numerical simulations to parameterizations of roughness for surface heat fluxes at high winds over the sea. *Mon. Wea. Rev.*, **130**,1926-1932.

Beven J. and H. Cobb, 2004: *Tropical Cyclone Report: Hurricane Isabel*. National Hurricane Center. www.nws.noaa.gov.

Charnock, H. 1955: Wind stress on a water surface. *Quart. J. Roy Meteor. Soc.*, **81**,639-640.

Csanady, G. T., 2001: *Air-Sea Interaction: Laws and Mechanisms*. Cambridge University Press.

Donelan, M., A., B. K. Haus, N. Reul, W. J. Plant, M. Stiassnie, H. C. Graber, O. B. Brown, and E. S. Saltzman 2004: On limiting aerodynamic roughness of the ocean in very strong winds, *Geophys. Res. Lett.*, in press.

Emanuel K. A., 1986: An air-sea interactio theory for tropical cyclones. Part I. *J. Atmos. Sci.*, **42**, 1062-1071.

Emanuel K. A., 2001: Thermodynamic control of hurricane intensity. *Nature*, **401**, 665-669.

Kurihara, Y., M. A. Bender, and R. J. Ross, 1993: An initialization scheme of hurricane models by vortex specification. *Mon. Wea. Rev*. **121**, 2030-2045.

Kurihara, Y., R. E. Tuleya, and M. A. Bender, 1998: The GFDL hurricane prediction system and its performance in the 1995 hurricane season. *Mon. Wea. Rev*., **126**, 1306-1322.

Moon, I.-J., T. Hara, I. Ginis, S. E. Belcher, and H. Tolman, 2004a: Effect of surface waves on air-sea momentum exchange: I. Effect of mature and growing seas. *J. Atoms. Sci.*, in press.

Moon, I.-J., I. Ginis, and T. Hara, 2004b: Effect of surface waves on air-sea momentum exchange: II. Behavior of drag coefficient under tropical cyclones. *J. Atoms. Sci.*, in press.

Moon, I.-J., I. Ginis, and T. Hara, 2004c: Effect of surface waves on Charnock coefficient under tropical cyclones. *Geophys. Res. Lett.*, in press.

Powell, M. D., P. J. Vickery, and T. A. Reinhold, 2003: Reduced drag coefficient for high wind speeds in tropical cyclones. *Nature*, **422**, 279-283.

S. Kelly and I. Ginis, Graduate School of Oceanography, University of Rhode Island, Narragansett, RI 02882. (kellys@carleton.edu, iginis@gso.uri.edu)

Copyright 2004 by the Graduate School of Oceanography/University of Rhode Island, SURFO program

Earthquake epicenter location with combined T- and P-wave waveforms

John Mischler[1] and Yang Shen

Graduate School of Oceanography, University of Rhode Island, Narragansett, Rhode Island

Abstract. In February 1999, a group of U.S. investigators deployed a 6-element hydrophone array for long term monitoring of the seismicity along the Mid-Atlantic Ridge between 15° and 35° N. During the 16th and 17th of March 2001, a large seismic swarm was detected by this array on the Lucky Strike segment of the Mid-Atlantic Ridge south of the Azores hotspot (~37° N) [Dziak 2003]. The highest frequency of events occurred at the beginning of the swarm, with activity becoming less frequent 1.5 hours afterwards [Dziak 2003]. This style of seismicity seems to be indicative of a diking event in the segment. The first determinations of the earthquake positions using T-wave records had a large degree of error and thus it is difficult to correlate the events spatially to determine the mechanism of the swarm. Here we report the results of a study to better define these locations using P-waves recorded by seismic stations in the Azores islands in addition to the T-waves. We acquired earthquake hydrophone logs indicating T-wave arrival times and P-wave arrival times from land-based seismogram logs. Each log was comprised of a list of earthquakes that occurred during the time frame mentioned. Events were then chosen from all listed events of the swarm according to the following criteria: number of stations that received the event, the magnitude of the event, and relative spacing between preceding and subsequent events. We then filtered out unnecessary frequencies and computed estimated arrival times as a guide to manually pick the T and P-wave arrival times. These arrival times were then analyzed using an iterative grid-search program that defined smaller and smaller grids to yield precise positions of the events selected for evaluation. These positions were compared to the positions determined previously. Preliminary results show that the addition of P waves has not significantly reduced the uncertainty of earthquake locations due to a poor signal to noise ratio and relatively large errors in P wave arrival times. It is thought that using the surface wave instead of the P-wave may improve the results..

1. Introduction

During the 16th and 17th of March 2001, a swarm of 128 earthquakes along the Lucky Strike segment of the Mid-Atlantic Ridge (MAR) near 37 degrees N was located by the hydrophone array in the northern MAR [Dziak, 2001]. This swarm lasted for 29 hours and almost half of the events took place in the first 1.5 hours. Following the peak of activity (42 events/hr), the event rate rapidly decreased to 5 events/hr. The swarm began at the Lucky Strike Seamount, but soon events were detected throughout the segment. The onset of seismicity was accompanied by 30 minutes of continuous, low frequency (3-15 Hz), tremor-like energy. The episode also produced 33 large enough earthquakes that were located by the global seismic network. This is the largest swarm ever recorded on the Lucky Strike Segment in the 25 years of monitoring the segment and one of the largest ever recorded on the MAR [Dziak 2003]. Field observations made at the Lucky Strike hydrothermal field by submersible dives following the swarm have indicated an increase in diffuse venting since the last measurements at the site in 1997. No evidence of recent pillow lava flows was found during these dives [Dziak 2003]. The Lucky Strike Segment is a slow spreading ridge that is dominated by the 8 km wide and 1 km high Lucky Strike Seamount. Within the summit depression of this seamount lies a vigorous hydrothermal system at about 1800 m depth. At its deepest, the segment is 3200 m from the surface [Smith 2003].

A similar seismic swarm occurred on the Juan de Fuca intermediate-rate spreading ridge on June 26 1993. This event began with low-level seismic activity and was accompanied by a seismic tremor. The seismic swarm showed clear propagation of the epicenters down segment and was accompanied by production of new pillow lavas [Dziak 1995]. Accompanying these events were hydrothermal event plumes that were emitted from the most seismically active regions of the ridge. These plumes are interpreted as being a result from the fracturing of the crust by an injection of magma [Baker 1995]. This event has been interpreted to be a lateral dike injection [Dziak 1995].

The Lucky Strike seismic swarm is selected for study due to its slow spreading rate [Smith 2003]. Observations have been made detailing diking events concerning both fast and intermediate spreading ridges, but there are no clear observations of diking events concerning slow spreading ridges. It is thought that the style of diking involved in slow spreading ridges may be different from the diking seen at intermediate and fast spreading ridges. In order to track the diking during a seismic swarm, hypocenters of events must be precisely located so as to understand the spatial and temporal distribution of events. This was done for the 1993 Juan de Fuca event [Fox 1995].

My research problem concerns the locations of the hypocenters associated with the Lucky Strike event. These locations were determined using only T-wave arrival times, which resulted in very large errors associated with the positions. Previous attempts to locate earthquakes in the Pacific Ocean carried with them less error due to the proximity of the hydrophone array to the center of seismicity [Schreiner 1995]. In the case of the Lucky Strike event, all of the earthquakes occurred well outside the hydrophone array and

[1]Now at Augustana College in Illinois.

generally in line with it. This minimized the differences in arrival times among the hydrophones and greatly increased the errors that accompany the determination of the hypocenters using only T-waves. Due to these significant errors, the spatial distribution of events cannot be known for certain. With the current location predictions, no standard propagation of hypocenters can be determined. We decided to use P-wave arrivals in addition to T-wave arrivals to locate the events. We hoped that this additional pick would add certainty to the data set and produce precise locations. Also, since these P-wave logs came from the land-based seismometers on the Azores, this data could prove to be a cheaper and more easily available source of data to locate events on the Lucky Strike Segment.

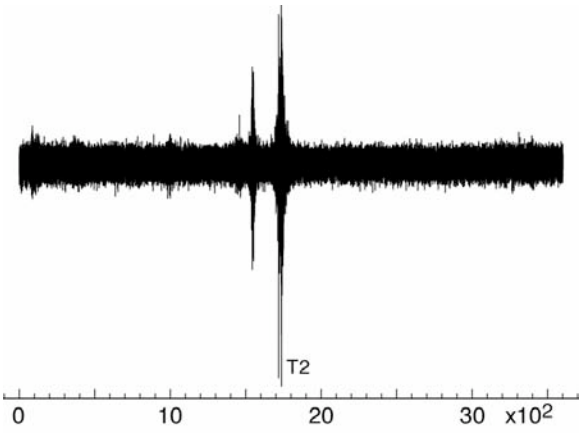

Figure 1. Example of raw hydrophone data.

2. Data Sets

In my study I dealt with two different data sets, those from the hydrophone array requested from the NOAA Vents program site and those from a seismometer array on the Azores Islands requested from the IRIS site. I was able to access four seismometer logs from the Azores. The Hydrophone array consists of six hydrophones deployed in February 1999 in the Northern Atlantic between 15 degrees and 35 degrees along the MAR. They are spaced ~1000 km apart and are centered on the ridge axis. The hydrophones receive T-wave seismic signals from events thousands of kilometers away with very low attenuation via the SOFAR channel [Dziak and Goslin 2003]. When choosing the events to be processed, I only selected events where at least 5 hydrophone stations recorded the event, the magnitude was above 209 dB, and there was sufficient spacing between the previous event and the subsequent event. This data set was then further refined by plotting the signals using the SAC (Seismic Analysis Code) program. Only events that had a reasonably clear and distinct T-phase arrival were chosen. It was also necessary for these events to have a corresponding seismogram data file form the Azores seismograph readings. After these criteria were met, 9 events were chosen for analysis.

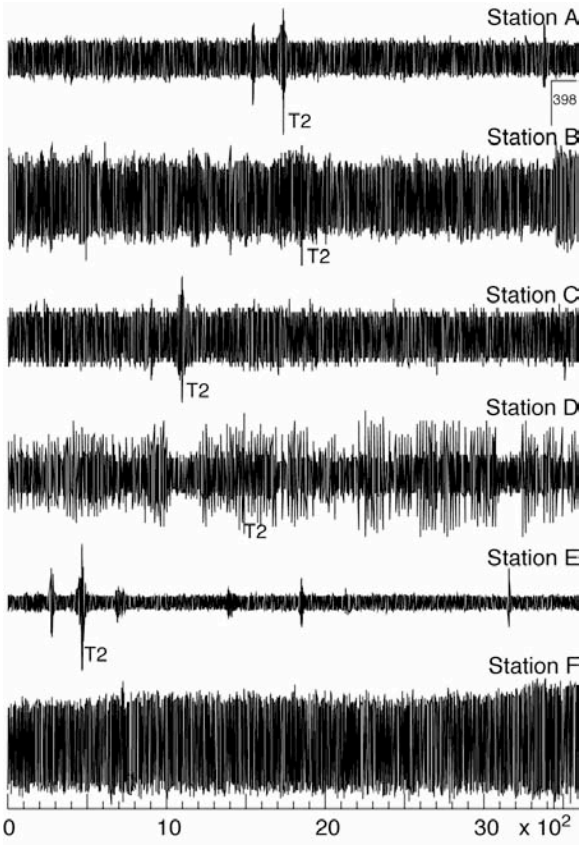

Figure 2. Hydrophone data that has been band-passed filtered leaving frequencies between 2.0 and 10.0 Hz. Hydrophone stations are located in the central North Atlantic.

3. Methods

Due to the time constraints on the project, it was decided that I would hand pick the arrival times. When manually picking the arrival times for this data, a large degree of error is possible in the pick. In order to identify the arrivals, I used a Fortran code that utilized the previous estimates of the locations of the earthquakes to produce a predicted arrival times for the T and P-phases for each event.

The hydrophone data was too noisy when first viewed (Fig. 1), so the data was filtered leaving only the frequencies between 2.0 and 10.0 Hz (Fig 2). In some cases, the frequency band had to be further narrowed to yield sufficient signal to noise ratio. Each hydrophone station was viewed separately (Fig 3) so to enable the examination of the most prominent wave packet (Fig 4) and chose the largest amplitude and the approximate center of the T-wave packet as the arrival time of the signal. This picking style was consistently used throughout the survey to ensure uniform results.

The land data was also extremely noisy when first viewed (Fig 5). We determined the optimum frequency for viewing the land-based seismogram data is between 0.05 to 0.1 Hz (Fig 6). The noise to signal ratio in the

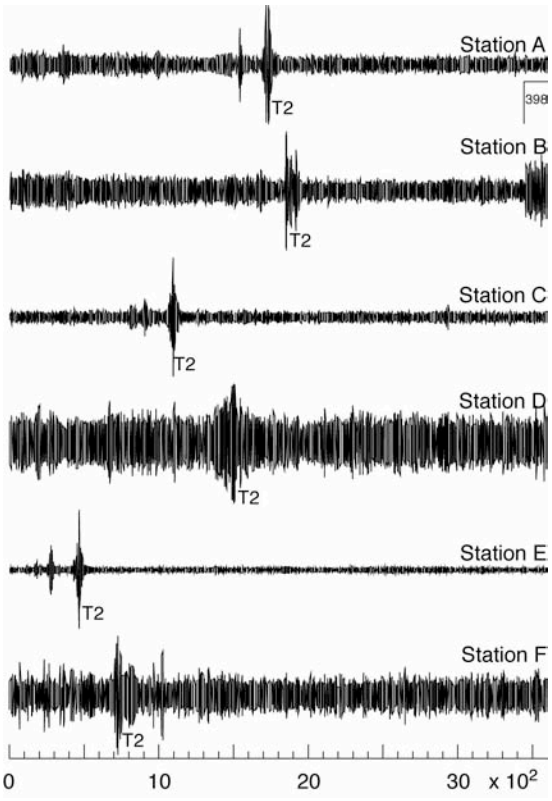

Figure 3. Hydrophone data band-passed filtered at a frequency range narrower than 2.0 and 10.0 Hz.

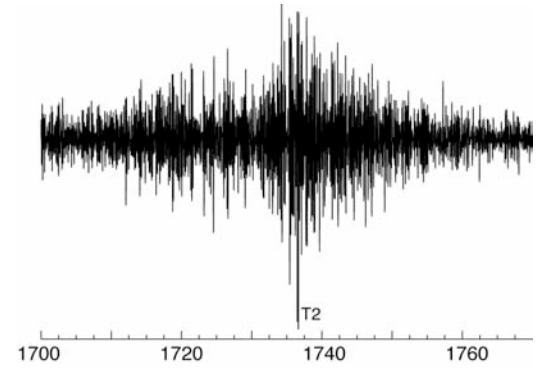

Figure 4. Selection of a prominent waveform from filtered hydrophone data.

land-based data was quite high for most of the events. I attempted to pick the P-wave arrival in some of the logs, but the pick was inaccurate due to the amount of noise present. The arrival times were then picked out of the file headers using a C-shell program. This data set was then processed by various programs to yield an output in the format needed to input into a grid search program.

We employed a non-linear grid-search method based on Rowlett and Forsyth [1984] and Wilcock and Toomey [1991] when locating the events [Shen 1997]. This program defines a grid in which each intersection in the grid represents a set of possible origin times for the events. The program searches through each set of times defined by the grid intersections until it finds the smallest misfit to the actual event times picked from the seismograph and hydrophone logs. Smaller and smaller

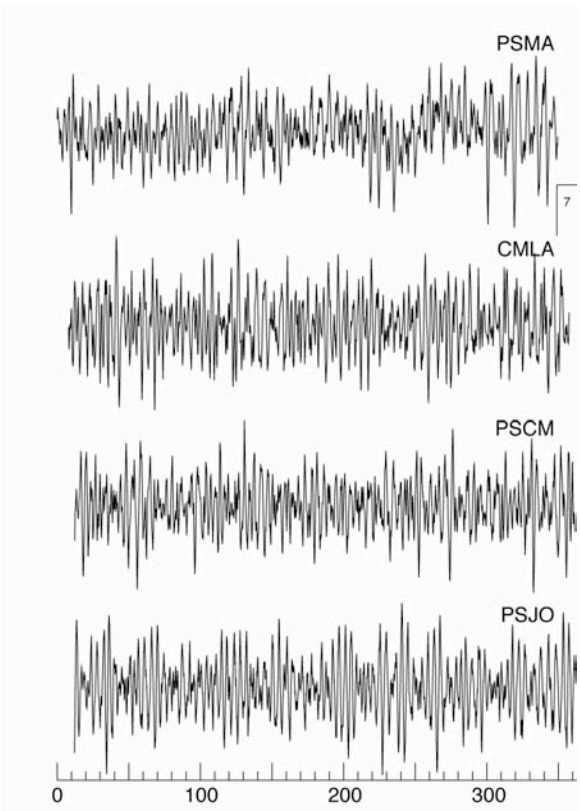

Figure 5. Raw land-based seismogram data located near the Azores in the central North Atlantic.

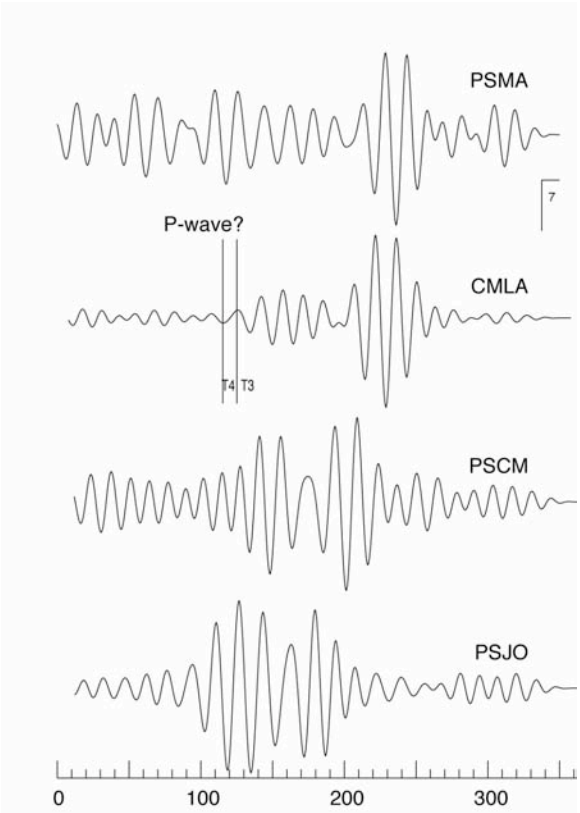

Figure 6. Land-based seismogram data band-passed filtered between 0.05 to 0.1 Hz.

grids are then implemented to refine the search and yield the lowest possible misfit for the arrival times chosen previously. When each origin time has been fitted to the single grid point with the smallest combined misfits, the program uses these times to calculate the location of the hypocenter. These locations are then mapped with bathymetry and station location (Fig 7).

4. Results

The resulting event locations were inaccurate when the picks involving the P-wave arrivals were involved. The locations involving only the T-wave arrivals were close to the previous positions, indicating that the T-wave arrivals were picked correctly. It was determined that the data was not refined enough to yield precise positions using the P-wave. The large uncertainty in event position remains and additional processing is needed to improve the results.

5. Future Work

The surface waves are more evident in the land-based seismogram data than the P-waves. We propose the use of the surface wave arrival time in conjunction with the T-wave arrival time as a possible method to determine precise positions of these events. This method is modeled after that of Forsyth and Shen used for events on the Easter-Pacific fast spreading center [Forsyth 2003]. Surface waves, like T-waves, yield excellent locations for epicentral position but poor depth constraints. We suppose that we will be able to cross-correlate the surface wave waveform of the largest event and use relative arrival times from this point for other events. It will be of interest to observe if this method, which has previously been tested on a fast spreading center, can be applied to the Lucky Strike Segment of the slow-spreading Mid-Atlantic Ridge.

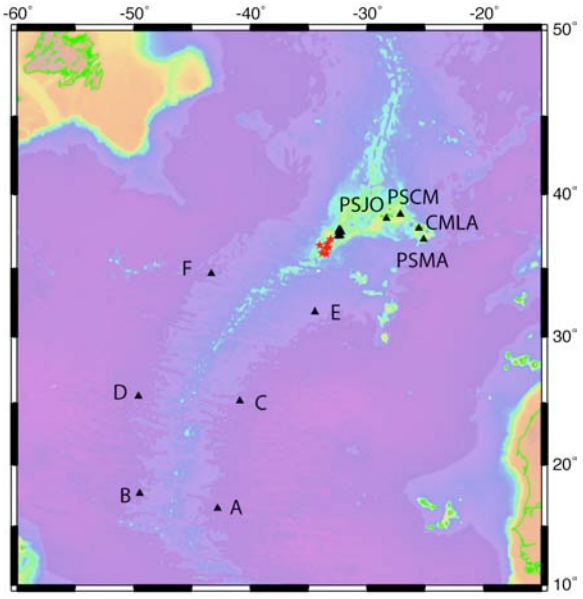

Figure 7. Location of seismic stations.

References

Baker, Edward T., Massoth, Gary J., Feely, Richard A., Hydrothermal event plumes from the CoAxial seafloor eruption site, Juan de Fuca Ridge, Geophysical Research Letters, 22, 147-150, 1995

Dziak, R., Fox, C., Smith, D., Tolstoy, M., Matsumoto, H., Bohnensteihl, D., Haxel, J., Fowler, M., Evidence of a Probable Magmagtic Episode at the Lucky Strike Segment, Mid-Atlantic Ridge, March 2001, J. Geophys. Res., in press, 2001

Dziak, R., Goslin, J., Smith, D., Lourencao, N., Bohnenstiehl, D., Matsumoto, H., Fox, C., Tolstoy, M., Luis, J., Long-Term Monitoring of Northern Mid-Atlantic Ridge Earthquake Activity Using Autonomous Hydrophone Arrays, J. Geophys. Res., 108, 2167, 2003

Dziak, Robert P., Fox, Christopher G., Schreiner, Anthony E., The June-July 1993 seismo-acoustic event at CoAxial segment, Juan de Fuca Ridge: Evidence for a lateral dike injection, Geophysical Research Letters, 22, 135-138, 1995

Forsyth, Donald W., Yang, Yingjie, Mangriotis, Maria-Daphne, Coupled seismic slip on adjacent oceanic transform faults, Geophysical Research Letters, 30, 1618-1621, 2003

Fox, Christopher G., Radford, W. Eddie, Dziak, Robert P., Lau, Tai-Kwan, Matsumoto, Haruyoshi, Schreiner, Anthony E., Acoustic detection of seafloor spreading episode on the Juan de Fuca Ridge using military hydrophone arrays, 22, 131-134, 1995

Schreiner, Anthony E., Fox, Christopher G., Dziak, Robert P., Spectra and magnitudes of T-waves from the 1993 earthquake swarm on the Juan de Fuca Ridge, Geophysical Research Letters, 22, 139-142, 1995

Shen, Yang, Forsyth, Donald W., Conder, James, LeRoy, Dorman N., Investigation of microearthquake activity following an intraplate teleseismic swarm on the west flank of the Southern East Pacific Rise, Journal of Geophysical Research, 102, 459-475, 1997

Smith, Deborah K., Escartin, Javier, Cannat, Mathilde, Tolstoy, Maya, Fox, Christopher G., Bohnenstiehl, DelWayne R., Bazin, Sara, Spatial and temporal distribution of seismicity along the northern Mid-Atlantic Ridge (15-35 degrees N), J. Geophys, Res., 108, 2167-2189, 2003

J. Mischler and Y. Shen, Graduate School of Oceanography, University of Rhode Island, Narragansett, RI 02882.

Copyright 2004 by the Graduate School of Oceanography/University of Rhode Island, SURFO program

Backscatter intensity and environmental forces in the West Passage of Narragansett Bay, RI

Sean Poche[1] and Rob Pockalny

Graduate School of Oceanography, University of Rhode Island, Narragansett, Rhode Island

Abstract. Narragansett Bay is a partially to well mixed estuary which receives salt water inflow from the Atlantic Ocean and fresh water from the Blackstone, Pawtuxet, and Taunton rivers. Acoustic Doppler Current Profiler (ADCP) data were collected at the University of Rhode Island Graduate School of Oceanography (GSO) dock approximately 100 m from shore at a depth of 10 m. A 1200 khz profiler sampled the water column in 0.5 m bins with the first (deepest) bin blanked. ADCP backscatter intensity data were corrected for time, and range, and tide related depth variation. First order observations were made by examining plots of ADCP backscatter intensity as a function of depth and time with intensity represented by color-fill. Backscatter data from 2.5 m and 7.5 m were extracted and plotted as a function of time to represent the upper and lower portions of the water column, respectively. Seasonal, fortnightly, daily and episodic variations, as well as a vertical gradient in backscatter intensity, were observed from color-fill and line plots of ADCP data. The West Passage of Narragansett Bay exhibits temporal and spatial variations in ADCP backscatter intensity. Seasonal variation is due to freshwater runoff and sediment transport while spring-neap and semi-diurnal tidal cycles producing consistent periodic variation in backscatter intensity in the lower water column due to increased water velocity and sediment re-suspension. Episodic peaks in backscatter intensity are produced by wind events that cause vertical mixing.

Introduction

Narragansett Bay is a partially to well mixed estuary that receives salt water inflow from the Atlantic Ocean and fresh water from the Blackstone, Pawtuxet, and Taunton rivers (Figure 1). Three north/south trending passages connect the bay to Rhode Island Sound, the East Passage, the West Passage, and the Sakonnet River. The East Passage is the main channel for water exchange between the bay and Rhode Island Sound, contributing approximately 80% to net exchange (Kincad et. al., 2003). It has a mean depth of 18 m, reaches a maximum depth of 46 m, and ranges in width from 1-5 km. The West passage contributes approximately 20% to net exchange (Kincad et. al.). It has a mean depth of 7.5 m, reaches a maximum depth of 15 m, and ranges in width from 1-2 km (Webster, 2001). The Sakonnet River contributes little to the circulation patterns of Narragansett Bay. The overall dynamics of Narragansett Bay are affected by fresh water runoff, well-defined spring-neap and semi-diurnal tidal cycles and episodic wind events. Fresh water runoff is highest from December to June and lowest from July to November (Kincaid et. al., 2003). A well-defined, 14-day spring-neap cycle and a 12.5 hr. semidiurnal tidal cycle with a maximum tidal variation of approximately 1-3 m has been observed in the bay. Winds affecting the bay are predominantly from the SW in the summer and from the NW during the winter; the change in direction taking place in April (Kincad et. al., 2003). The purpose of this study is to determine if spatial and temporal variability in water column backscatter intensity exists, and to qualify the effect of environmental variables on backscatter intensity.

[1]Now at University of New Orleans

Data

Acoustic Doppler Current Profiler (ADCP) data were collected in Narragansett Bay near the University of Rhode Island Graduate School of Oceanography approximately 100 m from shore at a depth of 10 m (Figure 2). A 1200 khz profiler sampled the water column in 0.5 m bins with the first (deepest) bin blanked. Data were collected from November 1999 to December 2000 at five-minute intervals with recorded values reflecting the average of 10 pings. Equipment malfunction caused several "gaps" in the data set used in this study (see Table 1). Data recorded by the ADCP include direction, velocity, and backscatter intensity. The Doppler shift measures the direction and velocity of the water column and backscatter intensity is

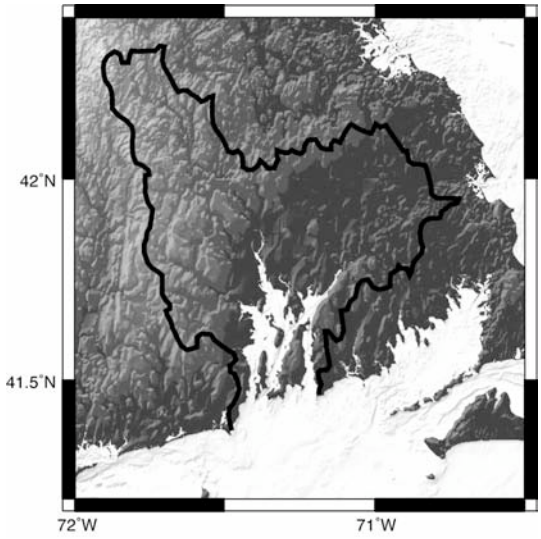

Figure 1. Map of Narragansett Bay and the drainage basins fot the Blackstone, Pawtuxet and Taunton Rivers.

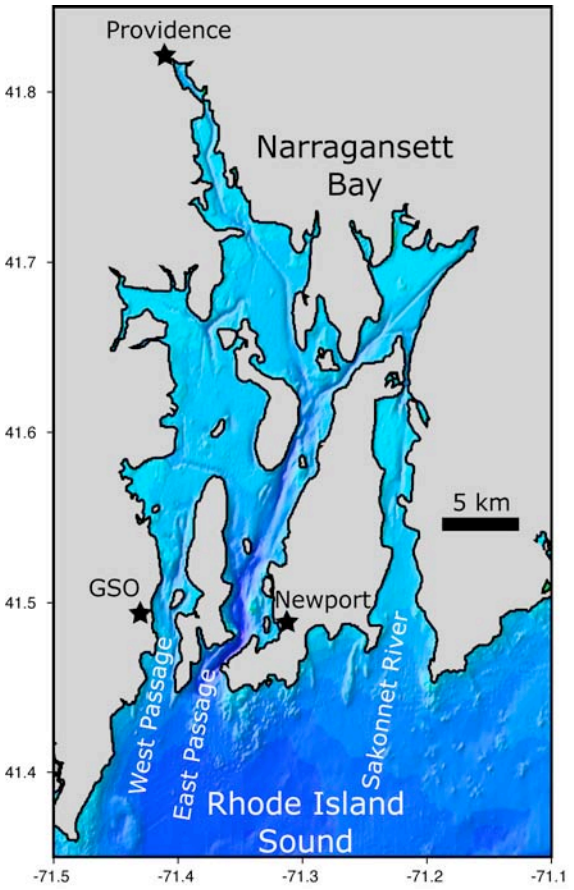

Figure 2. Map of the Narragansett Bay and the East and West Passages

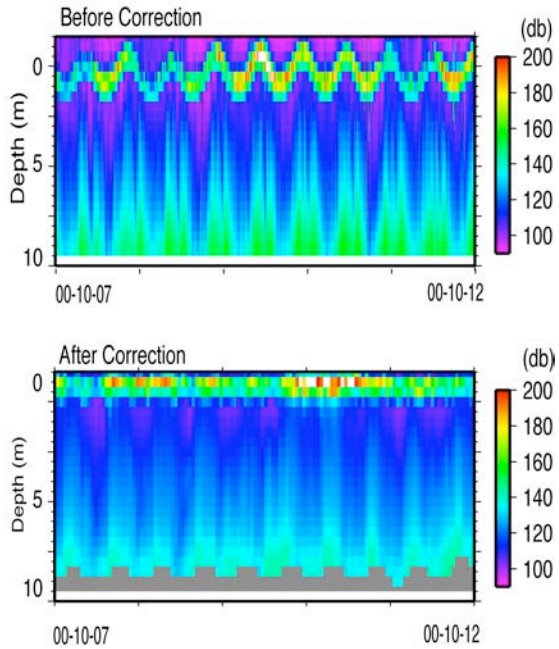

Figure 3. ADCP backscatter intensity plots before and after correcting for signal attenuation and making the sea surface the reference datum and.

Table 1. Dates of good data.

Start Date (MM/DD/YYYY)	End Date (MM/DD/YYYY)
11/24/9199	01/20/2000
02/21/2000	03/19/2000
03/22/2000	03/23/2000
03/27/2000	05/25/2000
06/03/2000	07/13/2000
07/20/2000	09/03/2000
09/30/2000	11/02/2000

measured by measuring the amplitude change in the returning signal.

Environmental data were obtained from various websites for use in this study. Total fresh water runoff data from the United States Geologic Service (USGS) website were collected at individual gaging stations (USGS, 2004). Tidal height data were obtained from the National Oceanic and Atmospheric Association (NOAA) for the Newport RI station (NOAA, 2004). Wind speed data were also obtained from the NOAA website for the Newport RI station (NOAA, 2004).

Methods

Several corrections were necessary to get ADCP backscatter data into a format for comparison with available environmental data: 1) conversion to Greenwich Mean Time (GMT), 2) correction for signal lost in transmission, and 3) removal of tide related depth variation. ADCP data were originally collected in Local Standard Time (LST). A difference of 4 hr. should have been observed. Instead a 3 hr. time discrepancy was observed while comparing plots of tide data to ADCP color-fill plots. The source of this time offset was due to an incorrectly set computer time on the data storage computer. This discrepancy was corrected by subtracting a factor of 0.125 from ADCP sample time.

ADCP backscatter intensity data were corrected for loss of signal strength in transmission (RDI 1996). Loss of signal is a function of depth and the correction was made according to the formula:

$$Ic = Io+((20\log_{10}(R+0.5)+(2)(0.5)(R+0.5) \quad (1)$$

where Ic is corrected intensity, Io is raw intensity, and R is the distance from the ADCP in meters.

The ADCP backscatter intensity data were also corrected by using tidal height from the NOAA Newport RI station. Tidal height was subtracted from bin number (depth), in order to remove a portion of the semi-diurnal tide signal. Subtracting tide height establishes the surface, not the bottom as the spatial reference for backscatter intensity. Figure 3 shows ADCP color-fill plots before and after correction.

Observations

First Order Observations

First-order observations were made by examining plots of ADCP backscatter intensity as a function of

depth and time with intensity represented by color-fill. Backscatter data from a depth of 2.5 m and 7.5 m were used to represent the upper and lower portions of the water column, respectively, and plotted as a function of time.

A seasonal variation in ADCP backscatter intensity was observed in color-fill plots of backscatter intensity and line plots of data extracted from a depth of 2.5 m and 7.5 m (Figure 4). Backscatter intensity is more pronounced within the entire water column from December, 1999 until the last week of June, 2000. From the last week of June, 2000 to the first week of July, 2000, backscatter intensity decreases drastically then levels out. Line plots show a decrease in amplitude of the long wavelength signal occurring at the same time.

Fortnightly variation in backscatter intensity was also observed in color-fill and line plots of data extracted from a depth of 2.5 m and 7.5 m. This variation can be seen consistently through the yearly record. Figure 5 shows line plots of backscatter intensity that exhibit a periodic oscillation with a 14-day period. The periodic oscillation is more prominent in the deeper part of the water column.

Daily variation in backscatter intensity was observed in color-fill and line plots of data extracted from a depth of 2.5 m and 7.5 m. This variation, seen consistently through the yearly record, can be observed as periodic increases in backscatter intensity in the lower portion of the water column, especially at inflection points in the semi-diurnal tidal cycle. A line plot of backscatter intensity shows an oscillating signal with a 12.5 hr period (Figure 6). Daily variation is also more prominent in the deeper portion of the water column, than nit is near the surface.

Episodic peaks in backscatter intensity were observed in ADCP color-fill plots and line plots of data extracted from a depth of 2.5 m and 7.5 m. Episodic, non-periodic peaks in backscatter intensity were observed as patches of hot colors near the surface, trailed vertically by warm color in the water column. Line plots of backscatter intensity show these episodic variations as anomalously high peaks, most prominently observed in data extracted from a depth of 2.5 m. It does appear, however, that in some cases the wind does affect the deeper part of the water column (Figure 7).

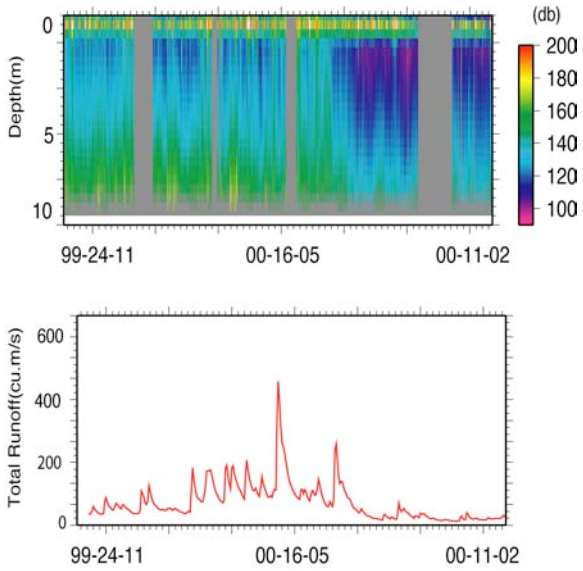

Figure 4. Color-fill plot of backscatter intensity (top) and total Narragansett Bay runoff during the period from November 24, 1999 to November 11, 2000. Note the decrease in backscatter intensity and runoff in late June.

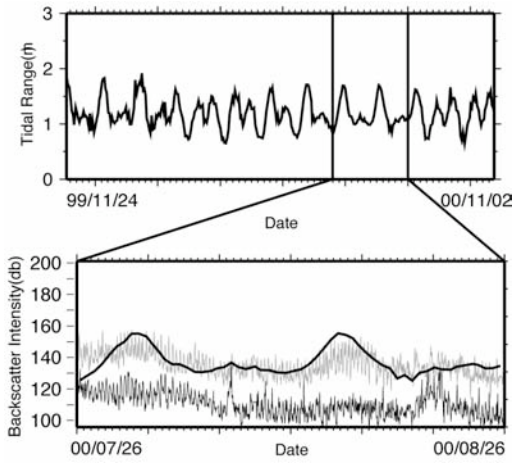

Figure 5. Line plot of tidal range (top) and line plot of 30 days of ADCP backscatter intensity on bottom with tidal range overlain (thick line). The gray and black line is ADCP data extracted from 7.5 and 2.5 m depth, respectively.

Comparisons

Comparison of ADCP backscatter plots with plots of environmental data revealed empirical correlation between fresh water runoff into the bay and seasonal variation in backscatter intensity. Figure 8 shows a sharp decrease in runoff occurring in late June, 2000 to early July, 2000, with an approximate 9-day time lag between decrease in runoff and decrease in backscatter intensity. Plotting backscatter intensity as a function of total runoff revealed correlation between fresh water runoff and backscatter intensity.

Comparison of ADCP backscatter intensity with tidal height and tidal range revealed empirical correlation between the spring-neap tidal cycle and the fortnightly variation in backscatter intensity (Figure 5). Tidal height was plotted as a function of time and compared to ADCP color-fill plots. The spring-neap cycle seemed to correlate visually with the 14-day variation in ADCP backscatter. In order to better determine whether the observed fortnightly signal was associated with the spring-neap cycle, minimumtide height was subtracted from maximum tidal height for each 24 hr. period, and plotted as a function of time. A comparison with backscatter extracted from a depth of 2.5 m and 7.5 m shows that correlation is higher with values extracted from 7.5 m than with values from 2.5 m.

Comparison of ADCP backscatter intensity with tidal height suggested an empirical correlation between the

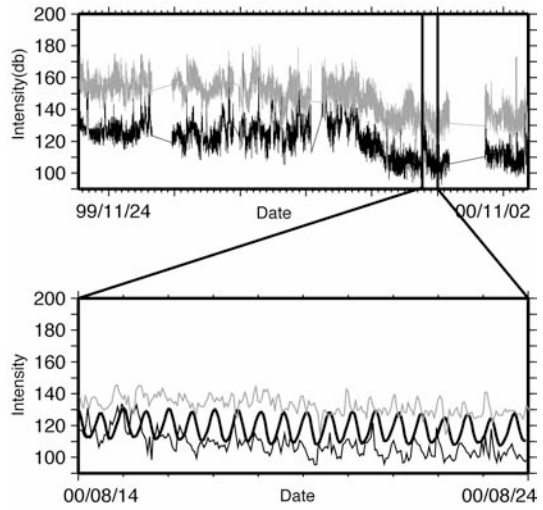

Figure 6. Line plot of ADCP back scatter intensity with inset of 10 day period. The tidal range (thick line, bottom) is overlain ADCP data extracted from 7.5 (gray line) and 2.5 m depth (black line).

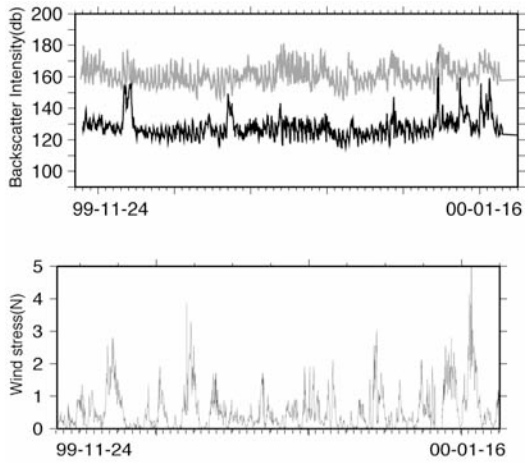

Figure 7. Plot of ADCP backscatter intensity (top) and wind stress (bottom). Peaks are more pronounced in shallow portion of water column (black linee) but is occasionally seen to affect deeper water column.

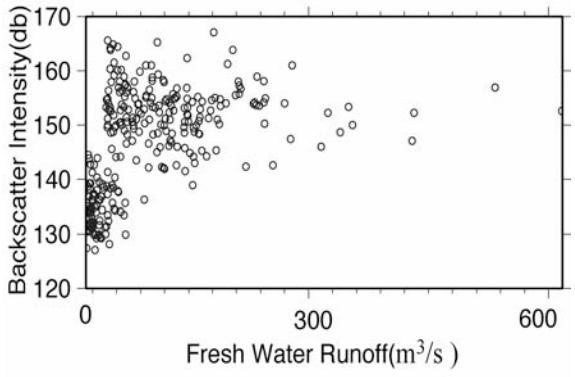

Figure 8. Plot of ADCP backscatter intensity as a function of fresh water runoff. Note that correlation is good to approximately 200 m^3/s.

semi-diurnal tidal cycle and daily variation in backscatter intensity. Tidal height was plotted as a function of time and compared to ADCP color-fill and line plots of backscatter intensity. The semi-diurnal tidal cycle exhibited strong empirical correlation with the 12.5 hr variation in backscatter intensity (Figure 6).

ADCP backscatter intensity also appeared to visually correlate with wind stress. Wind stress was plotted as a function of time and compared to ADCP color-fill plots and line plots of data extracted from 2.5 m. Wind stress was further broken into E/W and N/S components and compared to backscatter intensity. Empirical correlation between stress magnitude, not direction, and backscatter intensity was found, as well as a time lag of several hours. Figure 7 shows a comparison of wind events to ADCP backscatter intensity.

Discussion

Comparison of ADCP backscatter intensity and environmental variables suggests a direct relationship between environmental factors and temporal and spatial variations in backscatter intensity. The seasonal variation in backscatter intensity appears to be associated with sediment transported into the bay by the Blackstone, Pawtuxet and Taunton rivers. During the December, 1999 to June, 2000 period of high runoff, additional terrestrial sediment enters the water column via fresh water runoff. Figure 8 shows correlation between runoff and backscatter up to a runoff rate of approximately 200 m^3/s. Although sediment is still transported at higher rates, the water column has a maximum capacity for suspended sediment. Increased trans-evaporation during the summer-fall period is most like the source of decreased runoff.

The fortnightly variation in backscatter intensity associated with spring-neap cycles appears to be related to re-suspension of bottom sediment. Increased flux of water into the bay during spring tides causes increased velocities and re-suspension of bottom sediments. Higher tides and increased volume vertically mix sediment into the water column, causing increased backscatter intensity, this produces the periodic, intermediate wavelength signal observed in backscatter intensity throughout the year. Because the bottom of the passage is the source of sediment, backscatter is higher in the deeper part of the water column.

The daily variation in backscatter appears to be associated with semi-diurnal tidal cycles. Re-suspension takes place due to the increase in flux of water into the bay at inflection points in the tidal cycle (i.e., high water in and out). Increased velocity at flood and slack tide cause an increase in backscatter intensity on a shorter yet still consistent period, hence the shorter wavelength signal associated with semi-diurnal tide. Again, mixing from the bottom of the water column is consistent with the observed vertical gradient in backscatter intensity.

The episodic variation in backscatter appears to be associated with wind stress. As wind perturbs the water column, vertical mixing takes place. The observed time lag, of several hours, is most likely due to the

relationship between duration as well as magnitude of wind stress. The longer the surface is subject to perturbation, the larger the variation in backscatter intensity. Peaks in intensity are observed vertically in the water column as well as near the surface. The relatively shallow West Passage is sensitive to perturbation by wind stress. Most likely, an additional relationship exists between wind stress and tidal range. Figure 7 seems to exhibit empirical correlation between wind stress, rising tide and episodic peaks in backscatter intensity.

Conclusion

ADCP backscatter data exhibit a strong visual correlation with environmental variables on several time scales. Seasonal variation in ADCP backscatter intensity correlates with freshwater runoff, suggesting a relation between sediment load and ADCP backscatter intensity. Fortnightly variation appears to correlate with spring-neap tidal cycles, suggesting a relationship between re-suspension of bottom sediment and backscatter intensity. Daily variation appears to correlate with semi-diurnal tidal cycles, suggesting a relationship between velocity, re-suspension of bottom sediment and backscatter intensity. Episodic variation appears to correlate with wind stress, suggesting a relationship between vertical mixing in shallow water and backscatter intensity.

References

Kincaid, C, et. al, Spatial and temporal variability in flow at the mouth of Narragansett Bay, *J. Geophys. Res.* 108(C7), 3218 doi:10.1029.2002JC1395, 2003

Webster, J. E., Observational study on the circulation of a shallow estuarine system, West Passage Narragansett Bay, RI

National Oceanic and Atmospheric Association Co-ops Database. Online. Available at www.co-ops.nos.noaa.gov August 2004

United States Geologic Service Database. Online. Available at www.usgs.gov August 2004

R. D. Instruments, Acoustic Doppler Current Profiler, Principles of Operation, A Practical Primer, Second edition. p.31. 1996

S. Poche and R. Pockalny, Graduate School of Oceanography, University of Rhode Island, Narragansett, RI 02882.

Copyright 2004 by the Graduate School of Oceanography/University of Rhode Island, SURFO program

Determining the distribution of magnetization within the oceanic crust at Endeavor Deep

Rachelle M. Richmond[1] and Rob Pockalny

Graduate School of Oceanography, University of Rhode Island, Narragansett, Rhode Island

Abstract. Despite the importance of marine magnetic anomalies, little is known about the distribution of magnetization within the magnetic source layer. Endeavor Deep exposes relatively young and unaltered crust created at the East Pacific Rise. Our study analyzes the distribution of remanent magnetic properties as a function of lithologic unit along the south rift wall of Endeavor Deep. Variations in natural remanent magnetization, susceptibility, and median destructive field define three units, which roughly correspond with observed lithology. The upper 200 m of extrusives were likely altered by low temperature oxidation, and carry a relatively low magnetization. The underlying 300 m of extrusives carry a relatively high magnetization (2.06 A/m), and likely contributes significantly to the amplitude of the magnetic anomaly signal. The transition zone from extrusive layer 2A to intrusive layer 2B and possibly the upper portion of layer 2B carries an unexpectedly high magnetization (1.59 A/m) and likely contributes to the magnetic source layer as well. A dramatic, increase in susceptibility occurs at the top of the transition zone that has not been observed in similar studies. Further geochemical analysis is required to better understand the processes that caused the variations in remanent magnetic properties observed in this study.

Introduction

Marine magnetic anomalies are central to placing the formation of oceanic crust within the context of plate tectonics, but little is known about their source. The amplitude of magnetic anomalies measured at the sea surface depend on a number of variables, such as: the depth to oceanic basement, the age of the crust, the spacing of polarity reversals, and the distribution of magnetization intensity within the crust [*McElhnny and Larson,* 2003]. The distribution of magnetization within the oceanic crust is the least understood of these factors and is constrained by magnetic measurements from a small number of oceanic drill holes, poorly located dredge samples, and ophiolite studies.

The simplest model for the source of marine magnetic anomalies assumes a source of constant thickness and magnetization that remains unchanged after formation at a spreading center [e.g., *Cande and Kent*, 1976]. In reality, the magnetic source layer is not due to one layer of constant thickness, but is subject to thermal, chemical, and tectonic alteration that can affect the source layer differently with depth and lithologic unit [*Pariso and Johnson,* 1991; *Smith and Banerjee,* 1986]. Our study analyzes the magnetic properties of unoriented, but precisely located rock samples collected at Endeavor Deep (Fig. 1) to determine the distribution of magnetization with depth and lithologic unit, as well as the influence of weathering and the presence of lithologic boundaries on crustal remanent magnetic properties.

Previous Work

Various studies have proposed different models of the magnetic source layer. *Tivey* [1996] used vertical magnetic profiling to suggest that the strongly but variably magnetized extrusive crust contributes almost completely to the magnetic anomalies at the Blanco Scarp. *Cande and Kent* [1976] proposed a two-layer magnetic source model, to account for the 10°-15° anomalous skewness observed in magnetic anomalies. Their model corresponded to seismic layer 2A contributing 75% to the total amplitude of magnetic anomalies. Similarly, *Tivey et al.* [1998] used near bottom magnetic profiles to demonstrate that the extrusives contribute 50-75% to the magnetic anomaly at Blanco Scarp. At Hole 504B, *Pariso and Johnson* [1991] documented that the intrusive dike unit contributes 30%-45% of the total anomaly field, and *Worm et al.* [1996] used magnetic logging to determine that the extrusive and intrusive layer contribute approximately equally to the surface anomalies. *Tivey and Christeson* (1999) indicated that at Hess Deep the extrusive layer actually has a higher magnetization (~15A/m) than the extrusive layer (~12A/m).

Studies at Hole 504B provide the most comprehensive analysis of magnetic properties, and the variation of these properties with depth and lithologic unit [*Smith and Banerjee*, 1986; *Pariso and Johnson*, 1991]. In these studies, variations in magnetic properties correspond with chemical, thermal, and/or lithologic boundaries (Fig. 2). The most striking change in magnetic properties occurred within the transition zone from extrusive to intrusive rock, which coincided with a change from low to high temperature alteration. Clearly, the source of magnetic anomalies is not completely understood, nor has the vertical distribution of magnetic properties been extensively studied.

Geologic/Tectonic Setting

Endeavor Deep is located at the northeastern boundary of the Juan Fernandez microplate (Fig. 3), exposes a cross-sectional view of young (~3 m.y. old) and relatively unaltered oceanic crust created at fast spreading rates (~154 km/my, *DeMets et. al*, 1994) along the East Pacific Rise. The Juan Fernandez

[1]Now at University of California, Davis

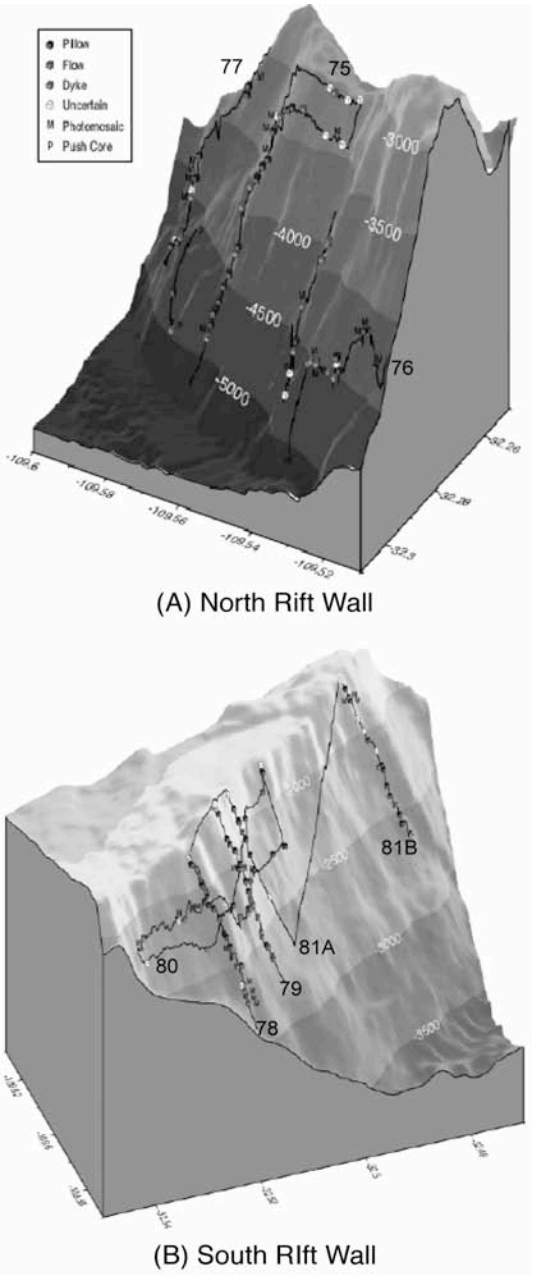

Figure 1. Location of samples for this study from: (a) the north and (b) the south rift walls of Endeavor Deep.

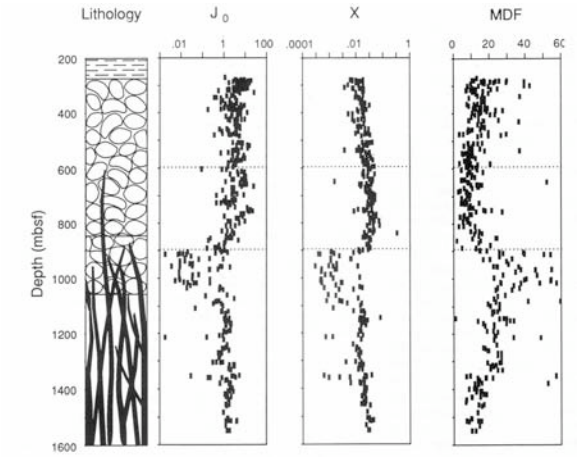

Figure 2. From *Pariso and Johnson* [1991]. Remanent magnetic properties as a function of depth and lithology at Hole 504B.

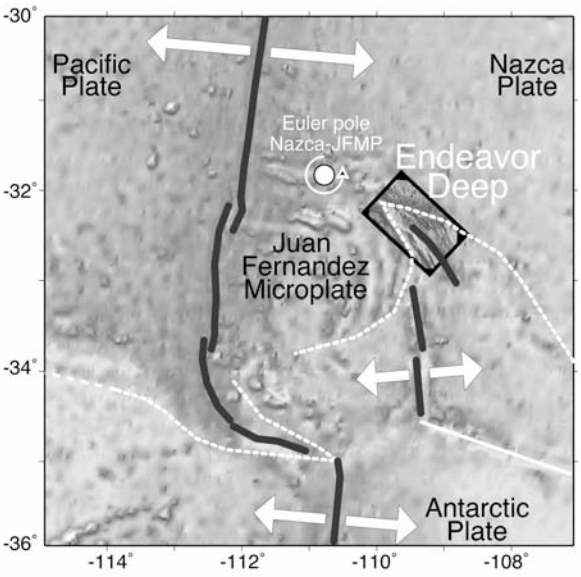

Figure 3. Location of Endeavor Deep on the Juan Fernandez microplate.

microplate, located at the triple junction of the Pacific, Nazca and Antartctic plates, is rotating clockwise due to shear coupling with the surrounding major plates [*Larson et al.,* 1992]. Endeavor Deep continues to form as the amagmatic northwest propagation of the East Ridge cuts into oceanic crust of anomaly 2A age [*Bird et al.*, 1998].

Data Collection

Sample Collection

Rock samples were collected along the north and south rift walls of Endeavor Deep by the Jason-II ROV on cruise TN165. Figure 1 shows the location of each of the 164 samples collected along the north and south rift walls of Endeavor Deep. First-order descriptions of rock type were made, and each sample was classified as a glass, pillow, flow or dyke. During the cruise, it was noted that the north wall was heavily faulted, making analysis of samples collected in this region difficult. Although some magnetic properties (magnetization and susceptibility) were measured, these values could not easily be placed within the context of lithology, either vertically or spatially. Samples were collected along the rift valley for measurements of recent volcanism, but are not discussed in this study. Thus, we focused subsequent analysis on samples collected only from the south wall of Endeavor Deep (Fig. 1b).

Remanent Magnetic Properties

For each of the rock samples collected along the north and south rift walls (Fig. 1), natural remanent magnetization (NRM) intensity and low-field susceptibility (χ_0) were measured. Following initial susceptibility and NRM intensity measurements, the samples were demagnetized using alternating field techniques. All magnetic properties were volume corrected using values found from specific gravity measurements. Magnetization values are given in A/m, field values are given in mT, and susceptibility values are given in dimensionless SI units.

Low-field magnetic susceptibility is the ratio of induced magnetization to applied magnetic field, measured as the sample is subjected to a weak alternating field (0.1mT) at high frequency (0.47 or 4.7kHz typically). Susceptibility was measured using a Bartington susceptibility bridge . Magnetic susceptibility is primarily dependent on magnetic concentration and grain size [*Moskowitz,* 1991 and *King and Hunt*, 1991], and tends to be more sensitive to the magnetically "soft" grains in a sample [*Smith and Banerjee,* 1986].

NRM intensity is the natural magnetization of the rock measured in the absence of an external magnetic field, which produces the magnetic field responsible for marine magnetic anomalies. Because the samples were unoriented, only the magnitude of the NRM was measured. Ideally, NRM is the magnetization acquired at the time of formation, but marine rocks are exposed to thermal, chemical, and tectonic alterations that can change or replace the original magnetization. NRM and the NRM demagnetization curves were measured using a cryogenic magnetometer.

Following the NRM measurements, the samples were demagnetized by a series of increasing alternating fields ranging from 20 to 85 mT peak value. The median demagnetizing field (MDF) (the alternating field peak value required to reduce the initial NRM by one half) was measured from the alternating field demagnetization curve. MDF is dependent on the magnetic stability of grains in a sample [*Moskowitz,* 1991], and is larger for samples containing a higher ratio of magnetically hard to soft material [*King and Hunt*, 1991].

Results

Remanent magnetic properties were analyzed as a function of lithologic unit for samples taken along vertical transects along the south wall of Endeavor Deep (Fig. 1b). Lithologic units are offset laterally across the south rift wall so that the lithology as a function of depth is not comparable for the three transects. *Popham* [2004] used video data taken from Jason-II dives to determine the lithologic boundaries along each transect (Fig. 4a). Extrusive layer 2A, the transitions between extrusive layer 2A and intrusive layer 2B, and a small portion of intrusive layer 2B were identified among the three transects in this manner. The top of the transition zone was used as a reference so remanent magnetic properties could be compared among the transects as a function of depth and lithology (Fig. 4b). This method is justified by the absence of intrusive samples above the transition zone for each of the three transects. Note that samples from transect 81B were not used for subsequent analysis because a transition zone was not found within this area of oceanic crust. Because extrusive samples were found at all depths below the top of the transition zone, it is difficult to determine the boundary for the dike unit based on the rock-type classification of the samples. A summary of the average remanent magnetic values is displayed in Table 1, and the magnetic properties as a function of meters above or below the transition zone are displayed in Figure 5.

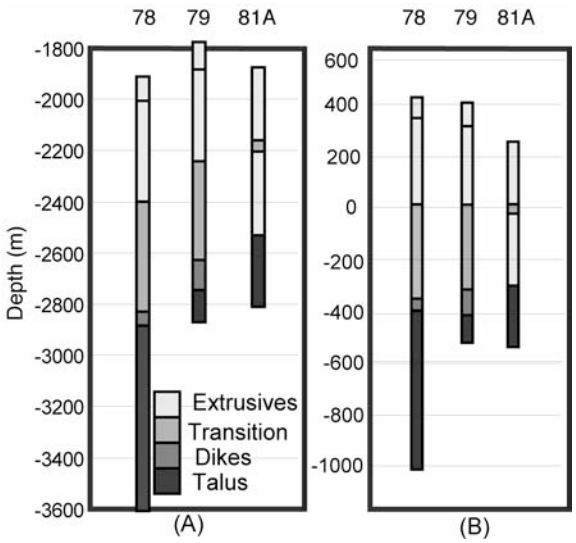

Figure 4. (a) Lithology of each of the three transects, 78, 79, and 81A respectively along the south rift wall of Endeavor Deep [from *Popham*, 2004]. (b) Each of the three transects with respect to the top of the transition zone.

The magnitude of NRM (J_N) as a function of relative depth is shown in Figure 5a. The smallest NRM intensity values occur from 500-300 m above the transition zone. In this region, the average NRM value is 0.36 A/m (standard deviation 0.43 A/m), with the

Table 1. Summary of average remanent magnetic properties for each of the three lithologic units.

Unit	J_N (A/m)	χ_o (SI)	MDF (mT)
Upper Extrusives 500-30 m	0.36 (0.42)	0.0013 (0.0011)	58.5 (16.2)
Lower Extrusives 300-0 m	2.06 (4.0)	0.0062 (0.011)	48.0 (20.8)
Transition Zone 0- -800 m	1.6 (1.8)	0.027 (0.017)	42.5 (22.1)

One standard deviation is given in ( ). J_N is natural remanent magnetization, χ_o is susceptibility, and MDF is median destructive field.

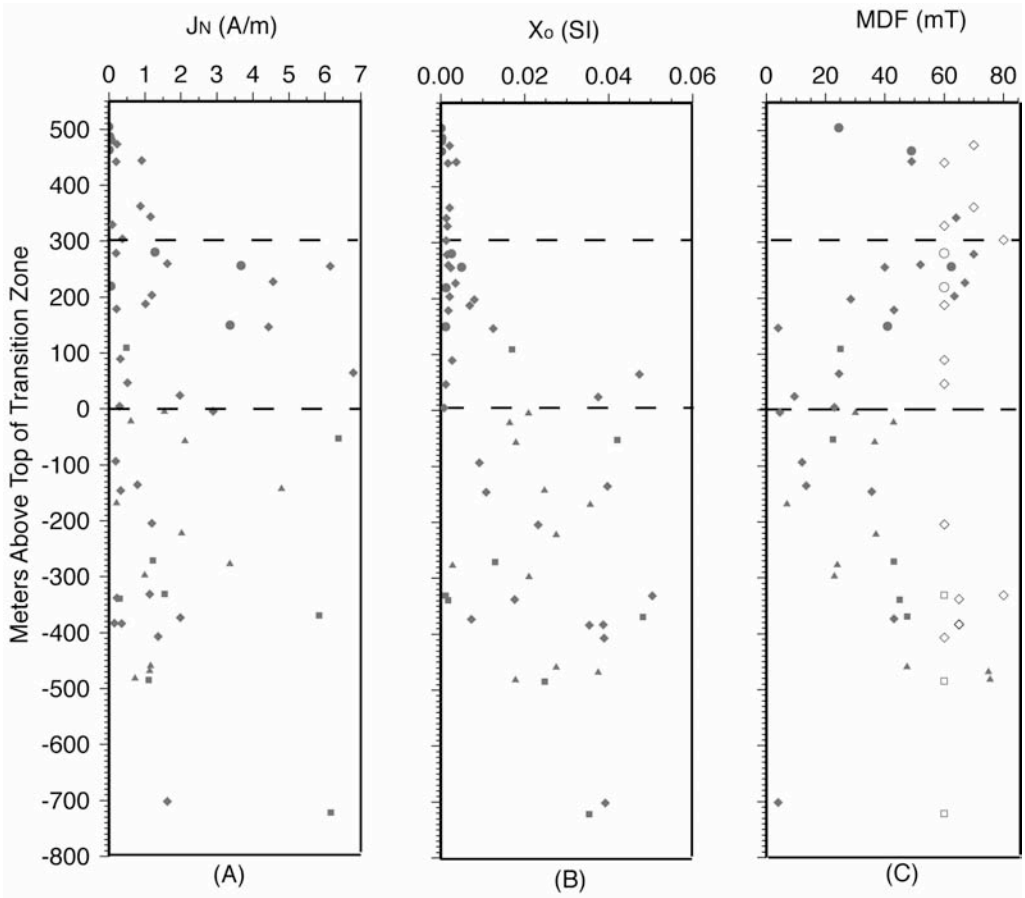

Figure 5. (a) Natural remanent magnetization, (b) susceptibility, and (c) median destructive field data are given as a function of meters above the top of the transition zone from along the south rift wall of Endeavor Deep. Dashed lines separate the three lithologic units: upper extrusives (500-300 m), lower extrusives (300-0 m), and the transition zone and possibly the upper intrusive layer (0- -800 m).

lowest magnetization occurring in glasses. NRM values increase slightly at 300m above the transition zone and have an average intensity of 2.06 A/m from 300-0 m above the transition zone with the most scatter occurring in this region (standard deviation of 3.99 A/m). Below the top of the transition zone, magnetization values (average value 1.59A/m with a standard deviation of 1.78 A/m) decrease slightly until 350 m within the transition zone, and remain relatively constant below this depth.

Susceptibility (χ_0) values are shown in Figure 5b, and similarly to NRM values, the lowest susceptibility values occur from 500-300 m above the transition zone with an average of 0.0013 SI units and a standard deviation of 0.00109 SI units. The smallest values in this region are again attributed to glass samples in the top 50 m. Below 300 m, there appears to be two trends: (1) the continuation of the low susceptibility trend from the upper region and (2) a trend increasing almost linearly toward the transition zone. In this region (300-0 m), the arithmetic mean of the susceptibility values is 0.0062 SI units and the standard deviation is 0.011 SI units. At the transition zone, susceptibility increases by almost an order of magnitude. Scatter is greatest in susceptibility within the transition zone (average 0.027SI units and standard deviation 0.017 SI units).

Results for the MDF values calculated from the NRM demagnetization curves are shown in Figure 5c. MDF values are large (average 58.5 mT, standard deviation 16.2 mT) in the upper 200 m where magnetization and susceptibility are low. From 300-0 m, as NRM intensity and susceptibility values increase toward the transition zone, MDF values decrease from ~60 mT to ~20mT (average 48.0 mT, standard deviation 20.8 mT). Below the top of the transition zone, where susceptibility is much larger than the overlying extrusive layer, MDF values are low and begin to increase again below -200 m. Scatter is higher for MDF values within the transition zone where the average value is 42.5 mT with a standard deviation of 22.1 mT.

In summary, the most striking features of the data are the obvious variations in the remanent magnetic properties (magnetization, susceptibility, and median demagnetizing field) that occur at the boundaries between three units (upper extrusives, lower extrusives, and the transition from extrusives to intrusives). In the upper 200 m of the extrusive layer (500-300 m), magnetization and susceptibility are significantly lower than the underlying crust. The glasses in this region

occur in the upper 50 m, and have the lowest measured magnetization and susceptibility values. MDF values in this region are relatively high. In the lower extrusive layer from 300 m to the top of the transition zone, magnetization increases, susceptibility continues to remain low with an apparent second trend of increasing values, and MDF values decrease. Below the top of the transition zone, magnetization remains constant but with less scatter, susceptibility values dramatically increase with more scatter, and MDF values begin increasing.

Discussion

Our magnetization data includes the entire 500 m of extrusive layer 2A, and extends through the transition between layers 2A and 2B and possibly into the upper portion of layer 2B. The major variations in remanent magnetic properties occur at two distinct boundaries. These properties have distinctly different characteristics within the following three units: (1) the upper 200 m of extrusive layer 2A, (2) the remaining 300 m of the extrusive layer up to the transition zone, and (3) the entire transition between layers 2A and 2B, possibly including the upper portion of intrusive layer 2B. From these variations we can infer the different chemical, thermal, and/or tectonic history of each of the three units.

Crustal Alteration History

The low magnetization and susceptibility as well as the high MDF values in the upper 200 m of the extrusive layer suggest that this region has likely undergone low temperature oxidation from titanomagnetite to titanomaghemite. Maghemitization occurs when Fe^{2+} diffuses from the rock and the remaining Fe^{2+} is converted to Fe^{3} under hydrothermal conditions [*Dunlop and Ozdemir*, 1997]. This process reduces the magnetic grain size which reduces the magnetization, but increases the stability of the altered rock [*Dunlop and Ozdemir*, 1997; *King*, 2004]. The relatively low susceptibility observed is indicative of the reduction in grain size in this case, and the high MDF values suggest a higher concentration of magnetically hard material (Fig. 5). Similar results for the upper extrusive layer were found at Hole 504B (Fig. 2), with the exception that magnetization values in the upper extrusive layer were higher than the underlying extrusive crust. Despite the relatively larger magnetizations, *Pariso and Johnson* [1991] suggested low temperature oxidation occurred within the upper extrusives, and the relatively lower magnetization values observed at Endeavor Deep are consistent with this process.

Low temperature oxidation appears to have occurred within the lower extrusive layer (from 300-0 m above the transition zone), but was not the dominant process. Two trends are evident at this level: (1) the same trend of low magnetization and susceptibility, and high MDF values that was apparent in the upper extrusive layer and (2) a trend of increasing magnetization and susceptibility, and decreasing MDF values with depth. The first trend is likely due to the same low temperature oxidation that occurred in the upper extrusive layer. The second trend is similar to the trend observed at Hole 504B (Fig. 2) within the lower extrusive layer [*Smith and Banerjee*, 1986 and *Pariso and Johnson*, 1991]. The decrease in MDF values suggests an increase in the amount of soft magnetic material, and the increase in susceptibility suggests either an increase in magnetic grain size or concentration [*King and Hunt*, 1991]. *Pariso and Johnson* [1991] suggested that the primary magnetic phase was low-Ti magnetite, formed when low-temperature oxidized titanomaghemite was reheated and inverted to low-Ti magnetite and ilmenite. However, it is difficult to determine if this is the same mechanism for the deeper extrusives at Endeavor Deep without mineralogy analysis.

Within the transition zone, susceptibility increases abruptly by an order of magnitude. NRM intensities are similar to the values observed above the transition zone, but decrease slightly with depth below the top of the transition zone. MDF values are similar across the transition zone, but increase slightly with depth below the top of transition zone (and possibly into the upper portion of intrusives). The remanent magnetic properties within the transition zone at Endeavor Deep (Fig. 5) are inconsistent with the transition zone at Hole 504B (Fig. 2). Magnetization and susceptibility decrease dramatically at the Hole 504B transition zone, and MDF values increase in this layer [*Smith and Banerjee*, 1986; *Pariso and Johnson*, 1991]. This abrupt change in remanent magnetic properties at the transition zone coincids with exposure to greenschist facies alteration determined by oxide petrography results [*Pariso and Johnson*, 1991]. Without geochemical analysis of the Endeavor Deep rocks, it is difficult to explain the processes that may have caused the inconsistency with Hole 504B. An increase in susceptibility reflects an increase in magnetic grain size or magnetic concentration [*King and Hunt*, 1991]. The difference between fine and large magnetic grain size is only a factor of about 2.5 [*King*, 2004], and would not account for the ten-fold increase in susceptibility that occurs at the transition zone.

At Endeavor Deep, average magnetization and susceptibility values are significantly lower, and MDF values are significantly greater overall than these same remanent magnetic properties observed at Hole 504B (excluding the anomalous trend that occurs at the Endeavor Deep transition zone). A likely explanation for this inconsistency in remanent magnetic values is that the cross-sectional crust at Endeavor Deep has been exposed to more low-temperature oxidation than Hole 504B. The surface of the rift walls at Endeavor Deep have been exposed to seawater, and are therefore more susceptible to weathering than Hole 504B. Low temperature oxidation that occurred at the ridge axis most likely affected only the upper portion of oceanic crust (layer 2A). When Endeavor Deep began rifting ~1 m.y. ago, [*Bird et al.*, 1998], the entire cross-section of oceanic crust was exposed to low-temperature alteration, perhaps at varying degrees.

Implications for Magnetic Anomaly Source Layer

At Endeavor Deep, the extrusive and intrusive layers have approximately equivalent average magnetizations (1.61 A/m and 1.59 A/m respectively). This is inconsistent with previous studies that found the extrusive layer to contribute almost completely to the magnetic source layer [Cande *and Kent*, 1976, *Tivey*, 1996, and *Tivey et al.*, 1998], but consistent with studies done at Hole 504B that found the intrusives and extrusives to contribute approximately equally to the anomaly field [*Pariso and Johnson*, 1991 and *Worm et al.*, 1996]. Surprisingly, the transition zone has high enough magnetizations to contribute significantly to the magnetic anomaly. Others have found the transition zone to have an insignificant magnetization [*Smith and Banerjee*, 1986 and *Pariso and Johnson*, 1991]. The relatively high magnetized transition zone could be specific to oceanic crust at Endeavor Deep, but this is unknown because of the small number of similar studies. At Endeavor Deep, the lower extrusives (300-0 m), transition zone and possibly the upper intrusives (0-800 m) contribute significantly to the magnetic source layer. Deeper portions of the intrusive layer and gabbros may also contribute to the magnetic source layer, but were either covered by talus or not exposed at all by the rifting at Endeavor Deep.

Conclusion

The magnetic structure of oceanic crust at Endeavor Deep varies significantly at the boundaries of three units, which roughly correspond with lithology.

(1) In the upper 200 m of the extrusive layer at Endeavor Deep appears low temperature oxidation has decreased magnetization and susceptibility, but increased MDF values. Due to the relatively low magnetization (0.36 A/m), this unit probably makes little or no contribution to the magnetic anomaly amplitude.

(2) The lower extrusive layer has undergone low-temperature oxidation as well, but to a lesser extent than the upper extrusive layer. A second process has caused a trend of increasing magnetization and susceptibility, as well as decreasing MDF values. This trend suggests an increase in magnetic grain size or composition as well as the amount of "soft" magnetic material. However the process which is responsible for this is unknown without further geochemical information. This layer has the highest relative magnetization (2.06 A/m), and probably contributes significantly to the magnetic anomaly amplitude.

(3) A significant variation in susceptibility occurs at the top of the transition zone that is inconsistent with other studies. This is most likely due to a change in magnetic composition and/or magnetic grain size. However, a change in magnetic grain size could not account for the order of magnitude variation alone. The process that caused this obvious change is not known, nor is it known if this behavior is specific to the oceanic crust exposed at Endeavor Deep. Surprisingly, the transition zone contributes significantly to the marine magnetic anomaly as well.

Acknowledgments. We thank John King, Carol Gibson, Brad Hubeny, and Chip Heil for the use of their magneetometer and helpful conversations about rock magnetics and use of magnetic equipment. For general assistance and brain-storming, we thank Roger Larson and Chris Popham. Rich Viso, Kim Carey, and Rhonda Kenny provided considerable help with the SURFO program without wich this would not be possible.

References

Bird, R. T., Naar, D. F., Larson, R. L., Searle, R. C., and Scotese, C. R., Plate tectonic reconstructions of the Juan Fernandez microplate: Transformation from internal shear to rigid rotation, *Journal of Geophysical Research*, 103, 7049-7067, 1998.

Cande, S. C. and Kent, D. V., Constraints imposed by the shape of marine magnetic anomalies on the magnetic source, *J. Geophys. Res.*, 81, 4157-4162, 1976.

DeMets, C., R. G. Gordon, D. F. Argus and S. Stein, Effect of recent revisions to the geomagnetic reversal time scale on estimates of current plate motions, *Geophys. Res. Lett.*, 21, 2191-2194, 1994.

Dunlop, D. J. and Ozdemir, O., *Rock Magnetism Fundamentals and frontiers*, edited by Edwards, D., Cambridge, 1997.

King, J. and Hunt, C. P., Appendix: Laboratory techniques and equipment for rock magnetism and paleomagnetism, in *Handbook from the Environmental Magnetism Workshop*, edited by Hunt, C. P., pp. 231-240, 1991.

Larson, R. L., Searle, R. C., Kleinrock, M. C., Schouten, H., Bird, R. T., Naar, D. F., Rusby, R. I., Hooft, E. E., and Lasthiotakis, H., Roller bearing tectonic evolution of the Juan Fernandez microplate, *Nature*, 356, 571-576, 1992.

McElhinny, M. W. and Larson, R. L., Jurassic dipole low defined from land and sea data, *Eos, Transactions, Amer. Geophys. Union*, 84, 362-366, 2003.

Moskowitz, B. M., Hitchhiker's guide to magnetism, in *Handbook from the Environmental Magnetism Workshop*, edited by Hunt, C. P., pp. 1-40, 1991.

Pariso, J. E., and Johnson, H. P., Alteration processes at Deep Sea Drilling Project/Ocean Drilling Program Hole 504B at the Costa Rica Rift: Implicaations for magnetization of oceanic crust, *J. Geophys. Res.*, 9611703-11722, 1991.

Smith, G. M. and Banerjee, S. K., Magnetic structure of the upper kilometer of the marine crust at Deep Sea Drilling Project Hole 504B, Eastern Pacific Ocean, *J. Geophs. Res.*, 10337-10354, 1986.

Tivey, M. A., Vertical magnetic structure of ocean crust determined from near-bottom magnetic field measurements, *J. Geophys. Res.*, 101, 20275-20296, 1996.

Tivey, M. A. and Christeson, G. *Hig- resolution magnetic imaging of extrusive and intrusive crust at Hess Deep and a comparison with Juan de Fuca and Hole 504B results*, AGU, vol. 80, no. 46, F985, 1999.

Tivey, M. A., et al.., Direct measurement of magnetic reversal polarity boundaries in a cross-section of oceanic crust, *Geophys. Res. Let.*, 27, 3631-3634, 1998.

Worm, H. U., Bohm, V., and Bosum, W., Implications for the sources of marine magnetic anomalies derived from magnetic logging in Holes 504B and 896A, *Proceedings of the Ocean Drilling Program. Scientific Results*, 148, 331-338, 1996.

Rachelle M. Richmond and Rob Pockalny, Graduate School of Oceanography, Univeristy of Rhode Island, Narragansett, RI 02882. (rmrichmond@ucdavis.edu, robp@gso.uri.edu)

Copyright 2004 by the Graduate School of Oceanography/University of Rhode Island, SURFO program

Cortisol regulation in larval summer flounder, (*Paralichthys dentatus*)

Xaymara Serrano[1], Philip Veillette and Jennifer Specker
Graduate School of Oceanography, University of Rhode Island

Abstract. Early development of flatfishes such as the summer flounder (*Paralichthys dentatus*) is dictated by two regulatory mechanisms: the nervous and the endocrine system. The concentration of hormones in the body is generally regulated by feedback mechanisms that allow response to the physiological needs. Perhaps one of the most known neuroendocrine system relationships is the *hypothalmic-pituitary-interrenal* (HPI) axis. The hypothalamus secretes CRH, which stimulates the pituitary to secrete ACTH, which in turn stimulates the interrenal to secrete CORTISOL. This axis is believed to prepare summer flounder larva for metamorphosis, in which CORT peaks at 4~5 weeks and Thyroid hormone (T4) peaks at 7 weeks after hatching. Nonetheless, it is still unknown when regulation of the HPI axis begin to occur. This process is believed to be involved with the completion of yolk sac absorption and eye pigmentation. To determine when does negative feedback inhibition of the HPI axis begins we will study the different developmental stages. CORTISOL has been implicated as having important roles in the brain (inhibitory signal of the HPI axis), the liver (sugar release) and the epithelium. We will examine how CORT levels change when we treat fishes with *RU-486* (synthetic blocker of CORT receptor, which stimulates the axis to produce more hormones) and *Dexamethasone* (synthetic CORT, which imitates its inhibitory effects). These processes will enable us to precisely measure the whole-body amounts of CORT in the fishes using the *Radioimmunoassay* (RIA) method. This method is based on the reaction between an antibody and an antigen (CORT) whose concentration has to be quantified. To examine the presence of CRH and ACTH in the body we will use the *Immunohistochemistry* (ABC method). Data collected from these experiments will allow us to answer our question. If the axis is being regulaled (negative feedback operational) we will expect to have higher levels of CORT when treating the fishes with *RU-486*, while we will expect to have lower levels of CORT with *Dexamethasone*. When treating with both hormones (RU and DEX) we will expect to have no net effect (CORT levels will remain low). We will expect this same result if the axis is not being regulated.

Introduction

Cortisol is a steroid hormone produced by the adrenal –or interrenal- gland with important functions in growth, regulation of energy metabolism, appetite and as a mediator of the stress system (which is thought to be essential for cell homeostasis). The actions exerted by cortisol are mediated by its glucocorticoid receptors (GRs) which regulate gene expression (De Kloet, 2004). In fishes, cortisol acts as a sea adapting hormone, being especially important for their survival during the early developmental stages.

Recent studies, particularly in stress response, have revealed that in teleost fishes exists bidirectional communication between the endocrine and neurological systems via hormones. The *hypothalmic-pituitary-interrenal* (HPI) axis is perhaps one of the most understood neuroendocrine system relationships. The activation of this axis is a nearly universal reaction of teleosts to stressors, and consists of a hormone cascade that culminates in the release of cortisol from the interrenal cells (Stratholt *et al*. 1997). Cortisol, end product of the HPI activation, exerts a negative feedback action on CRH and ACTH secretion from the hypothalamus (Bernier and Peter, 2001) and it is the major coticosteroid among teleosts (Stratholt *et al*., 1997). The HPI axis is believed to prepare summer flounder larva (*Paralichthys dentatus*), a marine teleost, for metamorphosis. This process of metamorphosis is defined by pigmentation, eye migration, development of the jaw apparatus and digestive system (Martinez and Bolker, 2003). In this species, the main focus has been placed on metamorphosis, but yet to little is known about what happens in the early larval stages.

The aim of this study is to determine when does negative feedback inhibition of the HPI axis begins. We will study the different developmental stages and we will examine how cortisol levels change when we treat fishes with *RU*-486, synthetic blocker of cortisol receptor, which stimulates the production of CRH and ACTH and Dexamethasone, which mimics the negative feedback effects of cortisol in the secretion of CRH and ACTH by interacting with specific corticosteroids receptors in the brain, the hypothalamus and the pituitary (Pottinger and Carrick, 2000).

Materials and Methods

Fish maintenance

Summer flounder larvae were acquired from the Aquarium Building at the University of Rhode Island Bay Campus. Fishes were maintained in seawater (30ppt) at a constant temperature ranging from 19-20^{o}C in a holding tank until the time of experiments trails. One-week-old larvae were fed on rotifers while three

1Now at University of Puerto Rico, Río Piedras

weeks old were feed on *Artemia nauplii*. At the time of experiments, fishes were transferred to four 18-gallon tanks for treatments.

Experimental design and sampling

Larvae were administered four different treatments at the pre-metamorphic (pre MET). An approximate of 3,000 fishes were used per each treatment at 1 day after hatching (1 DAH) and one week after hatching with an average weight of 0.5mg. At three weeks, an approximate number of 350 larvae were used per each treatment with an average of 2.5mg. The four treatments administered were: (1) Control treatment – dimethylsulfoxide (DMSO) with acetic acid and phosphate buffer saline (PBS); (2) Ru 486 dissolved in DMSO (50mg/mL) diluted in acetic acid (1:10), PBS (1:100) and seawater (1:1000) for a final concentration of 0.12µM; (3) Dexamethasone dissolved in ethanol (79mg/mL) for a final concentration of 20µM; (4) Ru 486 plus Dexamethasone with same concentrations described before. Duration of experiments was four hours. After completion of treatments, larvae were removed from tank, anesthetized in MS222 (100mg/L buffered in 200mg sodium phosphate/L) and weighted. Three fishes were fixed in 10% neutral buffer formalin (NBF) per treatment, while the rest were stored in tubes at -20^{o}C.

Cortisol Radioimmunoassay (RIA)

The protocol used was based in part on *Hiroi, et al., 1997*. In brief, larvae were homogenized in 500µL of PBS and sonicated. Samples then were spiked with ~1000 cpm volume of radioactive cortisol, allowing calculation for extraction efficiencies. Samples were extracted using 1.5mL of ether and left to evaporate overnight before doing RIA. Samples then were reconstituted using 500µL of standard diluent (pH=7.4). Extraction efficiencies were calculated using 50µL of the reconstituted volume. Mean value for extraction efficiencies was 87.5%.

Following RIA protocol, samples with 200µL of reconstituted volume were added 150µL of ^{3}H labeled cortisol (tracer), 100µL of cortisol antibody at 1:100 dilution and were incubated overnight under a hood. After being incubated, samples were added 400µL of Dextran coated charcoal (DCC) to remove unbound cortisol. Centrifugation for 15 minutes at 4^{o}C allowed separation of charcoal from the sample. Finally, 500µL were removed from samples and added 5mL of scintillation fluid. Cpm's obtained for each sample from the scintillation counter were compared in a standard curve of known cortisol concentrations. Data colleted was analyzed using statistics.

Immunohistochemistry (ICC)

Samples that had been fixed in NBF were dehydrated using different percents of alcohols. Tissue was embedded in paraffin and cut into thin pieces of 6µm on the microtome. Paraffin sections were placed on poly-L-lysine coated slides and dried overnight before proceeding with the ICC. Sections then were deparaffinized, hydrated and incubated in 0.3% H_2O_2 for 30 minutes. To localize CRH in the brain we used the following procedure:

Results

Cortisol RIA

Average values of cortisol whole-body concentrations were obtained from the scintillation counter after the RIA process. Treatments administered at one day post-hatch larvae resulted in mean cortisol levels of 0.323 ± 0.037 ng/g (control), 0.077 ± 0.030 ng/g (Ru 486), 0.121 ± 0.035 ng/g (Dex) and 0.118 ± 0.037 ng/g (Ru + Dex) (Figure 1). Treatments administered at one week post-hatch larvae resulted in mean cortisol levels of 0.101 ± 0.059 ng/g (control), 0.054 ± 0.013 ng/g (Ru 486), 0.040 ± 0.010 ng/g (Dex) and 0.057 ± 0.012 ng/g (Ru + Dex) (Figure 2). Last treatments administered upon completion of the experiment were at three weeks old larvae and resulted in mean cortisol levels of 0.285 ± 0.029 ng/g (control), 1.954 ± 0.066 ng/g (Ru 486), 0.026 ± 0.006 ng/g (Dex) and 0.042 ± 0.008 ng/g (Ru + Dex) (Figure 3). Cortisol levels in the control treatments decrease from 0.32 ng/g in one day-old larvae to 0.10 ng/g at one week old and increase in three weeks old-larvae to 0.28 ng/g.

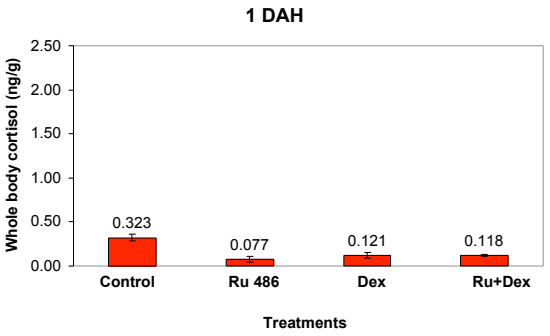

Figure 1. Average whole body cortisol concentration in larval summer flounder at one day post-hatch exposed to Ru 486, Dexamethasone and both.

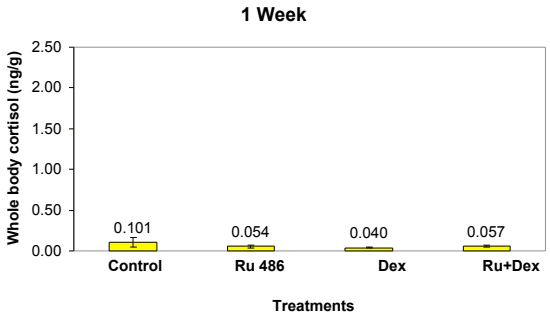

Figure 2. Average whole body cortisol concentration in larval summer flounder at one week post-hatch exposed to Ru 486, Dexamethasone and both.

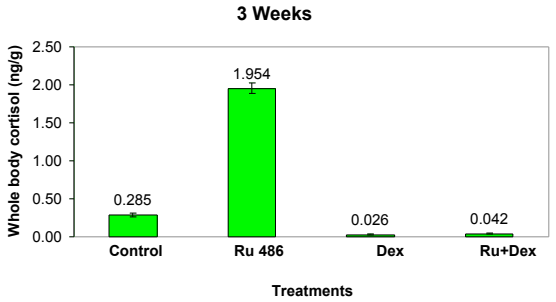

Figure 3. Average whole body cortisol concentration in larval summer flounder at three weeks post-hatch exposed to Ru 486, Dexamethasone and both.

Discussion

The most important finding of this study is that negative feedback inhibition of the HPI axis in summer flounder begins somewhere in between one week and three weeks after hatching. We found cortisol levels higher than expected at one day after hatching, but similar levels for the other treatments: Ru 486, Dex and both. This may be explained by the fact that maternal origin hormones stored in the yolk sac have not yet being entirely consumed. By one week, we found similar levels in all the treatments, including the control. Interestingly, by three weeks we found the HPI axis completely functional and regulated. Ru 486 caused an increase in cortisol levels, while Dex caused a decrease in cortisol levels, as predicted. In the treatment where we added both treatments we expected levels similar to the control, but the lower levels obtained may suggest that Dex may be exerting a stronger effect upon the axis.

Marine fish species are very different, therefore, activation and regulation of the HPI axis could occur at different times depending in factors such as the hatching time, development of the egg prior to hatching and the yolk sac. Studies in Japanese fish flounder larvae have concluded that the endocrine system becomes functional before the completion of the yolk sac absorption, when the switch from maternal (yolk) to an endogenous larval hormone source occurs (Tanaka *et al*. 1995). In yellowtail fish species, HPI axis and stress response are not functional during larval stages and do not become activated until larvae reached the juvenile stage (Sakakura *et al.,* 1997). Barry *et al*., 1994 focused in the HPI axis activation in rainbow trout, a freshwater species and found that the interrenal is capable of producing cortisol prior to hatching. Cortisol levels were found to be 0.3ng/g by hatching because cortisol of maternal origin was stored in eggs and used during early embryonic development, but increased by one week to 1.4ng/g. HPI axis was found to develop responsiveness to stress two weeks after hatching and one week prior to exogenous feeding. This stress hyporesponsive period of rainbow trout may be due to inability of most stressors to produce a CRH signal large enough to overcome the negative feedback inhibition exerted by cortisol. This period is considered to be homologous to the one that occurs in mammals, especially in rats, when stressors do not elicit increases in cortisol levels maybe because this is a critical time when steroids can have permanent effects upon development.

This lack of response to stress in rainbow trout reflected an immaturity of the higher brain, especially the hypothalamus and the pituitary. Experiments concluded that negative feedback mechanisms within the HPI axis developed three to four weeks after hatching and that the HPI axis is first functionally integrated and responsive to stress at two weeks (Barry *et al*., 1995). Similarly, in summer flounder, late activation found of the HPI axis could be due in part by an immature brain, hypothalamus and pituitary. Summer flounder larvae could be using their energy to develop all the necessary structures of the neurological and endocrine systems to then activate and fully regulate the HPI axis. If we compared the rainbow trout species and the summer flounder, these last ones have a bigger yolk sac at the time of hatching (which may explains why we found higher cortisol levels at day one) and also have different hatching time. Further work is necessary to precisely determine when cortisol regulation of the HPI axis begins and to determine if in effect, this period occurs in an homologous way in other animals.

Acknowlegements. I would really like to thank God and my family for being my motivating force each day of my life. I would like to thank also Jennifer Specker, Philip Veillette and Misty García for all the support and patience in the lab. Thanks also to Jason, Neil, Danielle, Steve, Rob Pockalny and my SURFO partners.

References

Barry, P., Malison, J., Held, J., Parrish, J., Ontogeny of the Cortisol Stress Response in Larval Rainbow Trout, *General and Comparative Endocrinology* 97, 57-65 (1994)

Barry, P., Malison, J., Ochiai, M., In VitroEffects of ACTH on Interrenal Corticosteroidogenesis during Early Larval Development in Larval Rainbow Trout, *General and Comparative Endocrinology* 99, 382-387 (1995)

Bernier, N., Peter, R., The hypothalamic-pituitary-interrenal axis and the control of food intake in teleost fish, *Comparative Biochemistry and Physiology Part B: Biochemistry and Molecular Biology* 129, 639-644 (2001)

Martinez, G., Boler, J., Embryonic andLarval Staging of Summer Flounder (*Paralichthys dentatus*), *Journal of Morphology* 255, 162-176 (2003)

Pottinger, G., Carrick, T., ACTH does notmediate divergent stress responsiveness in rainbow trout, *Comparative Biochemistry and Physiology Part A*: 129, 399-404 (2001)

Sakakura, Y., Tagawa, M., Tsukamoto, K., Whole-Body Cortisol Concentrations and Ontogeny of Aggressive Behavior in Yellowtail (*Seriola quinqueradiata*), *General and Comparative Endocrinology* 109, 286-292 (1998)

Stratholt, M., Donaldson, E., Liley, R., Stress induced elevation of plasma cortisol in adult female coho salmon (Oncorhynchus kisutch), is reflected in egg cortisol content, but does not appear to affect early development, *Aquaculture* 158, 141-153 (1997)

Tanaka, M., Tanangonan, J., Tagawa, M., de Jesus, E., Nishida, H., Isaka, M., Kimura, R., Hirano, T., Development of the pituitary, thyroid and interrenal glands and applications of endocrinology to the improved rearing of marine fish larvae, *Aquaculture* 135, 111-126 (1995)

Inside a submersible chemical analyzer: pressure vs. flow and signal spreading characteristics of the individual components

Lori A. Schultz[1], and Al Hanson

Graduate School of Oceanography, University of Rhode Island, Narragansett, Rhode Island

Abstract. Submersible chemical analyzers in use at the University of Rhode Island's Graduate School of Oceanography adapt a continuous flow technology that incorporates both the preparation of a sample, adding and mixing the reagents into the water and then the testing of the water using optical detection as the sample passes through an analytical channel of the instrument. Optimization of the channel design would allow for faster reaction times, increased accuracy and expansion possibilities. A test bench has been designed to study the pressure versus flow characteristics and the signal spreading effects each component contributes to both the channel it operates in and the effects on the analyzer as a whole.

Introduction

A Submersible Chemical Analyzer is the logical next step in the evolving, "need results faster" world in which we live. The development of Flow Injection Analysis (FIA) technology came about to standardize and automate the tedious and time-consuming job of chemical analysis. Putting the technology to work in a body of water, be it ocean or pond, has allowed scientists to see changes and trends in a manner not possible with the individual sample taking that had been done up until this point.

As the demand for these analyzers increase, so does the requested array of available chemical compounds to be tested for. Due to the complex testing requirements for some compounds, the ability to put many of these channels in a piece of equipment is reliant on the size and compatibility of the parts. It becomes critical for each piece of the instrument to work in careful precision with each other. One faulty or poorly designed piece placed in one channel affects the flow in the channels connected to it, in turn directly affecting the analysis capability of the instrument

The components incorporated into the current design of the submersible analyzer work well for the chemicals being tested for today. The need to expand the capability of the instrument requires optimization of the current design. This will allow for faster, more accurate measurements and the ability to expand the array of compounds tested for in one instrument.

This paper is not designed to discover any new concepts about FIA. Its purpose is to classify individual pieces of equipment used to make up the submersible in such a manner as to provide insight to the designers on possible problem areas. It is possible, and even probable that technology has advanced to a point that better suited components may be readily available.

Experiment and Data

Setup

A bench was designed and built to test both the pressure/flow characterisitics and the signal response time of a single analytical channel. These two characterisitics were chosen both for the relative ease in testing and the potentially critical information that could be found.

The bench for the pressure/flow analysis consists of a variable voltage sample pump, a 0-15 psi digital pressure gage, an analog flow meter, a DC power source, a terminal board on the bench itself (wired to the the fixed voltage side of the power source) and the necessary tubing and connectors (See figures 1 and 2). All of this was mounted to a piece of fiberglass to provide an inert base. The component being tested was placed at the end of the bench with a 50 cm piece of tubing available for waste. The placement of the connectors and tubing were adjusted to accommodate the size and electrical needs of all parts being tested so that the bench set up remained the same for all components. Figure 1 is a computer design of the test bench before it was built. The actual bench resembled this design closely, with the exception of the tubing layout. Figure 2 is the conceptual flow diagram of the pressure/flow test set up.

The test bench was modified slightly to accommodate the set up for the signal response time. It was found that there is a direct relationship between the flow rate and the DC voltage applied to the sample pump. This allowed for the flow meter to be eliminated thus reducing any additional mixing due to methodology. Two-three way tees follow the sample pump: The first has the pressure gage attached to it, the second connects to the reagent pump that introduces the dye into the experiment. Short pieces of $1/8^{th}$ inch tubing are used at the three-way tee and at the optical detector inlet (to connect the component being tested) to further reduce the possible mixing. Separate containers were used for intake and waste with a third added for the dye.

A laptop computer with the National Instrument's LABView™ Software installed was used as a data acquisition device. A virtual instrument (VI) was designed to monitor the voltage of the pump and to control any additional equipment on the bench. Later the VI was modified to accommodate the output signal of the optical detector and to control the reagent pump

[1] Now at Austin Peay State University, Clarksville, TN

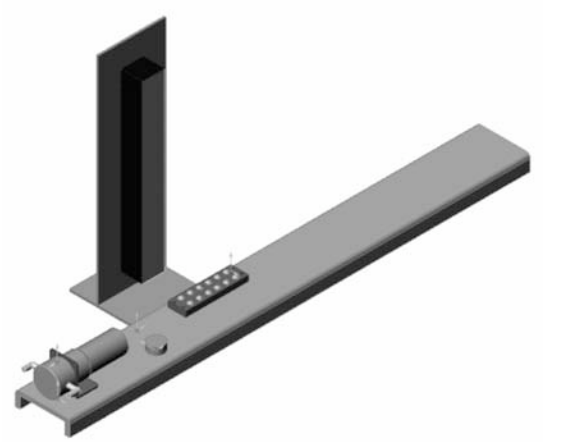

Figure 1. CAD drawing of the test bench.

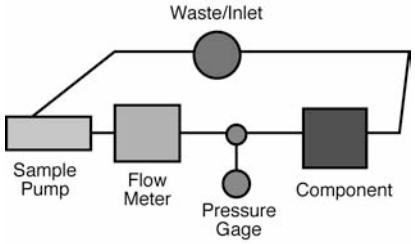

Figure 2. Flow Diagram for pressure vs. flow test.

functions. The program also writes the data from the graphs into a text file for later evaluation.

Experiment

Pressure vs. Flow Test. Water is introduced into the channel by the main pump on the bench which was controlled directly at the DC power source. It passes though the flow meter to a three-way tee, where the pressure gage gets a reading, just as the water flows into the component. To allow for recirculation of the water throughout the test, the waste line emptied into the top of the inlet container above the water line. The added height (9 inches) allowed a sufficent amount of backpressure in the test channel to force the pressure gage readings into an accurate range. A baseline test was run every day to be used later for comparison to the component readings and to ensure proper operation of the bench.

Initially the voltage supplied to the sample pump was to be used as the constant during the experiment. After a few of the components were tested, it was found that a side by side comparison of characteristics was difficult due to slight variations in the corresponding flow rate supplied by the pump. It was also pointed out that because of the differences in current instrumentation, flow rate data was the easiest to manipulate during later evaluation.

Typically the components in the instrument are subjected to approximately five and twenty milliliters per minute flow rate depending on their placement in the instrument. By choosing rates just above, in the middle, and below those rates, it was hoped that a better

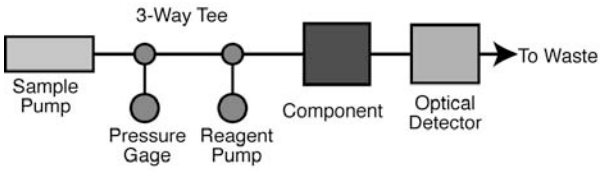

Figure 3. Flow Diagram for the Signal Response Time test.

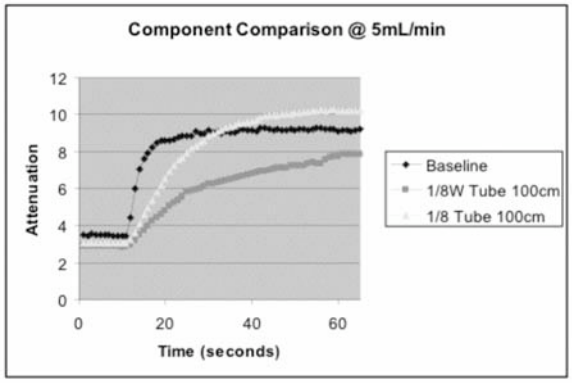

Figure 4. Signal response Time Comparison.

understanding of the characteristics of each component could be obtained.

Each component was tested three to five times, with time in between for the pressure and flow to return to their manually along with the voltage (DC) shown in the VI. This data was then logged into a spreadsheet program for analysis.

Signal Response Time Test. The design of the test bench (Figure 3), adds a reagent pump to introduce a colored dye in the flow channel right before the component being tested. The desired result for the baseline run was a square graph output (Figure 4) This would allow for a comparison of slope of the line and time of response produced by each component.

The flow rates for this test were chosen to be closely asscociated with the two most common rates used in the instruments when in the field, 5 and 20 mL/min. The red dye was pumped into the flow at 1 mL/min for increments of one to four minutes. The optical detector is designed to test at wavelength of color 540. A baseline were taken every morning for comparison value. Each component was tested a minimum of three times and the results averaged.

For both data sets, LabVIEW™ writes the information into a designated data file to be opened later by a spreadsheet program. To compare the data, the difference between the attenuation signal with no dye added and the value of the signal at the plateau is found, the high and the low points in the signal. Identifying the points on the slope that correspond with 10% and 90% of the difference provides points in which to find the time differential between occurrence. This value is then plotted against other like values from other components for comparison.

Experiment and Analysis of the Data

Pressure vs. Flow

The slope of the line generated by a pressure vs flow plot is related to the amount of pressure the component introduces into the channel of the analyzer and is found using the linear regression tool in the spread sheet program. This relationship allows for an accurate computation (within 0.1 psi) of the back pressure produced at flowrates between3 and 20 mL/min. Figure 5 shows how the graphs appeared for 2 components and the baseline tests.

The tubing was tested in the same format as the components. Three lengths, 8 cm, 50 cm, and 100 cm were chosen for comparison. Lines were made from each of the three types of tubing and used only for this test. The pressure vs. flow plots, regression lines, slope, and correlation values are found. The slope of each line is plotted against the length of line it was taken from. This forms the linear equation:

$$M = mL + b \quad (1)$$

Where *M* is the backpressure calculated at each length, *L,* the length of tubing used during the test. This value M is then inserted for the slope value in the pressure relationship.

$$P = FM \quad (2)$$

Here, *P* is the total backpressure produced in the tube and *F* is the flow rate of the fluid. The combined equation

$$P = F\,(mL + b) + \text{y-intercept} \quad (3)$$

can be used to calculate the pressure values of any length of tubing at any flow rate between 3 and 30 mL/min, where *F* stands for flow and *L* for the length of the tube. The y-intercept for the pressure equation is usually zero, but could be adjusted to the average value of intercepts of the three lengths of tubing. Figure 6 shows comparison data for some of the component tests at the 5 ml/min flow rate.

4.2 Signal Response Time

The connectors and components had results that were easily interpreted and to a certain degree expected. The amount of mixing contributed by the connectors was negligible when compared with the mixing due to the components in the channel (see figure 7).

The tubing required longer amounts of time to test, and there were variations in the results, that although not large, could be interpreted in different ways. For the longer lengths of tubing, 4 tests were performed, each adding sixty seconds to the logged time. The slopes on the 60 sec graph did not provide a discernible plateau to measure from, resulting in the data not being usable. The 120 sec through 240 sec graphs had plateaus but the maximum values would be slightly different from test to test. Logic would say that the longer the test, the higher

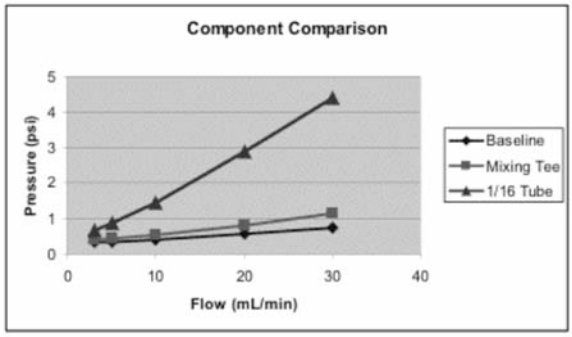

Figure 5. Pressure versus flow plots for components

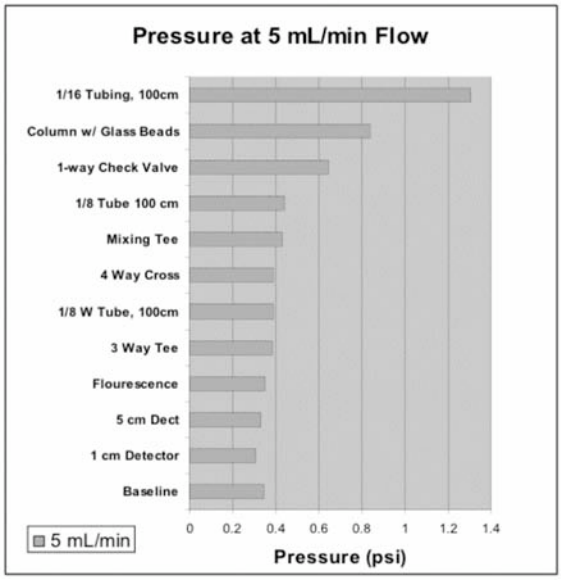

Figure 6. Pressure/Flow Comparison at 5mL/min.

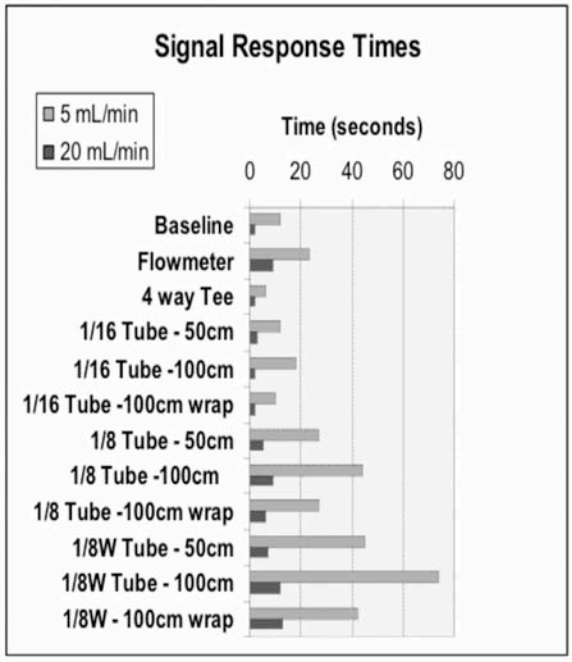

Figure 7. Signal Response Time Comparison at 5 and 20 mL/min.

the maximum value, but that was not always the case. In some cases the time differential between graphs was 10-20 seconds. In those cases, the test was redone, to rule out any experimental error.

The question was posed that a coiled piece of tubing would provide better mixing characteristics than a mostly straight piece of tubing. The tubing at the 100cm length was tested pulled straight and then again, coiled around a 3.25-inch cylinder. From the results, it appears that this true in all types of tubing tested, probably due to gravity and velocity causing turbulence in the line.

The flow rate also plays an important part in the mixing ability of the instrument. Response times are significantly shorter at the high flow rate. The downside is that the signal levels are also lower. Some tests were done at a 10 mL/min flow rate for a comparison value, but due to inconclusive data, more work in this area would need to be done.

It was intended that the sample pump be tested during this experiment. The design of the test bench was chosen to help facilitate this. However, when the pump was moved to the center of the bench where the other components were tested, the pressure readings were rendered inaccurate because of the suction through the lines caused by the pump. It was determined that the pump was overpowering the reagent pump, and although dye flow was shut off, the pump provided enough pressure in the line to pull the dye into the main flow channel. The signal data was inaccurate and could not be used. Another design for testing the mixing characteristics of the sample pump will have to be devised. Figure 7 shows a comparison of some of the components tested and their response times.

Discussion & Conclusion

The data found after testing is definitely preliminary in nature, but does provide a reference point for designers in identifying some possible problem areas. The pressure /flow relationship characteristics found for some of the components raise the question of how necessary these items are to the design of the instrument.

The flow meter used in the instrument is not accurate at the flow rates used in the instrument. This was a known shortfall of the component at the time, but it did provide feedback that there was in fact flow in the instrument, even if the measured rate was not accurate. Now, with the added knowledge of the backpressure the component provides in the instrument as well as the signal spreading it produces, a new component may be found to better fill these requirements in the instrument.

More work needs to be done in the investigation of some of the components due to the occasional erratic data produced during testing. Continued testing would rule out measurement inaccuracies and may provide a better understanding of what is actually going on. Better incorporating the LABView™ data acquisition capabilities would also narrow the error margin.

As to whether the individual backpressures are additive in nature, more work needs to done. One certain test runs, it did in fact appear that they could be, but those test specifically put components together randomly. When two or three components were lined up as how they would appear in a channel, the results were inconclusive.

One other part of the testing comes in understanding how a change made to fix a backpressure problem would effect the signal response time. On the tubing data for example, the 1/8th inch wide bore tubing contributed the lease amount of back pressure to the system, but conversely contributed some of the worst spreading /mixing characteristics. Knowing that these are only two characteristics studied for this project, the question that is raised is what other factors need to be analyzed when applying these small changes?

Other areas to continue to look into include new technology, the use of a different flow rate, and a possible replacement of the flow splitters, specifically the five-way splitter currently used in the channel design now, since accurate data could not be found during this testing setup. Initially this could indicate a problem area for the designers, and yet, more study and a slightly different test setup may show different results.

The continued desire for these instruments to become more accurate and encompass more areas of analysis will ensure the ongoing study of the optimization of these submersibles. As manufacturers design smaller, more efficient technology, the availability of better parts should increase as well. Nanotechnology may be the next step in putting these instruments into the "smaller, better, faster" bracket of development as time goes on. Only further study, and the dedication and innovation of the designers will continue to propel the submersible chemical analyzer into the mainstream of diagnostic equipment used in the future.

Acknowledgements. This project would not have been possible with out the help and guidance of all of the guys at SubChem Systems, Inc. at GSO/URI. My sincerest thanks go to Eugene Morin for his expertise with LabVIEW™, Richard Sweetman and Pete Egli for their knowledge of chemistry and the internal workings of the instruments, and Pete Obuchowski, Eric Martin, Chris Kreuter and Steve DeSilva, the Ocean Engineers for their time, sound boarding capability and vast knowledge of how things are suppose to work. Finally and most especially, Dr. Al Hanson for his time, patience and mentoring ability that allowed me to explore, investigate and learn over the twelve weeks I spent at URI.

References

Bishop, Robert H., *Learning with LabVIEW™* 6i, Prentice Hall, New Jersey, 2001.

Eggins, Brian R., *Chemical Sensors and Biosensors*, edited by David J. Ando, pp 1-66, 125-194, John Wiley & Sons, Ltd., New Jersey, 2003.

Fang, Zhaolun, *Flow Injection Separation and Preconcentration*, pp 1-44, 197-218, VCH Publishers, Inc., New York, 1993

Trojanowicz, Marek, Applications of Flow Injection Methods in routine Analysis, *Flow Injection Analysis, Instrumentation and Applications*, pp 298-418, World Scientific Publishing Co. Pte. Ltd., New Jersey, 2000.

Dr. A.K. Hanson, Graduate School of Oceanography, University of Rhode Island, Narragansett, RI 02882. (akhanson@gso.uri.edu)

A survey of ozone and balloon trajectories over Narragansett, RI

Maya Stevens,[1] and John Merrill
Graduate School of Oceanography, University of Rhode Island, Narragansett, Rhode Island

Abstract. Ozone plays an important and increasing role in the concern of global warming. The level of ozone changes through out the atmosphere, with the largest concentration being in the stratosphere and a lower concentration being in the troposphere. However, the atmosphere is a very dynamic place with air being transported through out the troposphere and the lowermost stratosphere making it hard to determine where the ozone is coming from. To study the ozone distribution and its variation, 43 ozonesondes were released, one a day from July 1st to August 12th from Narragansett, RI. The ozonesondes measure the mixing ratio of ozone with respect to height. Temperature, humidity, and pressure are measured as well. Information about the winds is gathered from a weather analysis model. Using the information about the winds, the ozonesonde is tracked. This tracking helps understand the sharp ozone gradients that are sometimes encountered by the instruments. Using ozonesonde data gathered from here and other institutions across North America allows the influence of pollution on ozone level to be measured along with the flow of pollution and ozone to be mapped.

Introduction

Atmosphere levels

There are multiple layers making up the Earth's atmosphere, the lowest of which is the troposphere. At this latitude, the troposphere extends to approximately 10 km above the Earth's surface. While the troposphere is a relatively thin layer, it still accounts for about 85% of the total mass of the Earth's atmosphere and contains virtually all atmospheric water (Holton). As altitude increases, the temperature in the troposphere decreases at a lapse rate or 6-7˚C/km. The concentration of ozone is naturally very low in the troposphere. However, through photolysis of N02 in the troposphere ozone is produced.

The tropopause is the separation point between the troposphere and the next layer, the stratosphere. The World Meteorological Organization defines the tropopause as the lower boundary of a layer where the temperature lapse rate is less than 2˚C/km for at least 2 km.

In the stratosphere, the temperature stops declining with height and starts to increase. This is also where most of the Earth's ozone is created by sunlight and the photolysis of molecular oxygen (Hobbs). Stratospheric ozone absorbs very short wavelengths from the sun, shielding most of the Earth's surface from the ultraviolet radiation. Since most of Earth's water is contained in the troposphere, the stratosphere is characteristically very dry. Due to this characteristic, stratospheric air can be traced by looking at the relative humidity of the air.

Measuring Ozone

There are two ways to measure ozone. One way would be to measure the total ozone in a column as a function of position on the globe. The Earth Probe: Total Ozone Mapping Spectrometer (TOMS) is a NASA satellite, which measures ozone as a function of position. TOMS was originally designed to orbit at 500 km and add supplemental data to the Advanced Earth Observing Satellite (ADEOS) TOMS. At a lower orbit then ADEOS TOMS, the EP TOMS would be capable of taking high-resolution measurements of ozone and other aerosol levels over cloudless parts of the Earth. These measurements would make it possible to determine how aerosol levels affect different geophysical quantities. However, when the ADEOS TOMS failed in 1997, the EP TOMS's orbit was boosted to its current altitude of 740 km. From this vantage point, the EP TOMS has a somewhat decreased resolution, but it can provide more of a global coverage. One of the important results from the EP TOMS is its imaging of ozone levels all over the world. Figure 1 illustrates the variation in ozone levels, which is often observed using the EP TOMS.

The second way to measure ozone is to measure it as a function of height (Komhyr, 1995). With this method an ozonesonde attached to a weather balloon is used. This type of measurement gives a vertical profile of the atmosphere showing how ozone, temperature and dew point vary with altitude. Routine weather balloons have only a radiosonde attached. This radiosonde transmits measurements of temperature and dew point back to the laboratory. In the case of an ozone profile, an ozonesonde must also be attached to the slightly larger

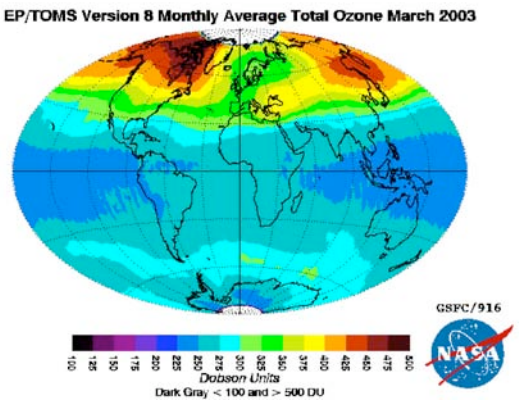

Figure 1. Images from the EP TOMS show how the total amount of ozone differs across the globe.

1California Polytechnic State University, San Luis Obispo

balloon. This method of measuring ozone can give data all the way up to 35 km. However, one of the limitations with this method of profiling is that only a small sliver of the atmosphere is measured and typically nothing is known about where the balloon travels once it is released. As shown from the TOMS, there can be very strong gradients where ozone changes significantly in small distances across the Earth. In such cases it would be very helpful to know how the ozonesonde is moving through the gradients. This is the motivation for calculating the trajectory of the balloon.

Methods

Ozonesonde Preparation

The ozonesonde is prepared in three stages according to the procedures developed by the NOAA Climate Monitoring and Diagnostics Laboratory. The first stage is done up to 5 days in advance. In the first stage of preparation, the air pump motor must be tested and broken in. To test the motor, the sonde is run on no/low ozone air for 10 minutes and then the pressure of the pump is measured along with the current of the pump to ensure the pump is working correctly. Then, the sonde runs on high ozone air for 30 minutes, which clears out the air intake tube. After that, the cathode cell is washed in the potassium iodide cathode solution. Next, the cathode is filled with 3.0 cc of solution while the anode is filled with 1.5 cc of anode solution. The sonde then runs on no/low ozone for another 10 minutes and the pump current is measured for a background ozone measurement. Next the sonde is run on 5 microamps of ozone for at least 5 minutes. Then the ozone generator is turned off and the time for the current to drop from 4 microamps to 1.5 microamps is measured. This is the response time of the sonde. Then for the last step, the sonde runs on no/low ozone air for another 10 minutes, which cleans all the ozone out of the intake tube and cathode cell. Finally the sonde is placed back in the styrofoam sonde box and stored in the dark for the next 5 days, completing the first stage of preparation.

The second stage is done the morning of the launch day. The pump is removed from the box and a fresh dose of 1.5 cc of anode solution and 3.0 cc of cathode solution is placed in the respective cells. Then, the pump runs for 10 minutes on no/low ozone air to help warm the pump up, followed by at least another 5 minutes of 5 microamps of ozone. After the 5 minutes, the pump runs on no/low ozone while the time for the current to drop from 4 microamps to 1.5 microamps is measured once again. In the second stage, the response time is usually several seconds faster than in the first stage. This is a good check to make sure the sonde is ready for use. Next, the sonde continues to run on no/low ozone air for 10 minutes to flush out the ozone. After that, a hose is placed over the exhaust for the cathode chamber, effectively connecting the exhaust to a soap bubble meter. The flow rate of the pump is measured by averaging over 5 runs the time it takes for a bubble to rise through 100 mL of volume. These times do not vary greatly over the 5 runs. This finishes the testing of the pump, however the radiosonde also needs to be set up at this time. The Viasala radiosonde, using an 18 V power supply, is connected to the ozonesonde while the ozonesonde is pumping no/low air. The radiosonde sends data via a radio signal to a receiver, a modem and a computer which then records and plots the data. The frequency used is 404 MHz. This is the end of the day of flight morning preparation.

The last stage of preparation deals with preparing the balloon and is done as close to the launch time as possible. A launch time of 2 pm local time was chosen because it is at that time which the temperature and pollution ozone are both at a maximum on a typical day. A 1200-gram weather balloon is inflated with approximately 3,000 L of helium until it can just barely lift an 1820 g weight off the floor. This is the amount of helium needed to produce enough buoyancy to cause the balloon to rise at approximately 5 m/s. At this point, the balloon is tied off and a parachute is attached to the balloon and a 120-foot pay out reel is attached to the end of the parachute. The ozonesonde is placed in the styrofoam box which is then duct taped shut and the radiosonde is taped to the outside of the box. The radiosonde battery must soak in water for 3 min to be activated. Then the sonde is placed outside for 10 min with everything running so that the instruments have a chance to acclimate to the conditions outside and produce a steady surface measurement. This waiting period also provides time to make a final check to ensure all the equipment is working correctly. After this acclimation period, the ozonesonde is attached to the end of the pay out reel. The balloon is taken outside and released as close to 2 pm as possible.

Calculating the Balloon Trajectory

To calculate the balloon trajectory, fields from the RUC (Rapid Update Cycle) model are used, providing the wind speed and direction at predetermined grid points (Benjamin et al, Bleck and Benjamin). The grid points are specific spots on a Lambert-Conformal shaped grid as shown in Figure 2.

Several layers of data are used starting at 1000 hPa and going at 25 hPa steps to 100 hPa. Using this data, several different approximations of the trajectory were used. The first approximation is that the winds vary only with pressure, but do not vary in position on any isobaric plane or in time. Using these assumptions, a first order approximation for the trajectory was obtained.

The next step then was to allow the winds to vary with position. As the balloon travels upwards, it passes each isobaric level at a different position, depending on where the wind blew it. To use the appropriate wind values for the next level, the balloon's position on the next level's grid is determined using wind from the previous level. Then the grid points immediately surrounding the balloon's position are used to calculate that level's wind, using a weighted average. However, for this approximation three separate cases that must be taken into account. The first case is if the balloon lands directly on a grid point. If this happens, then no

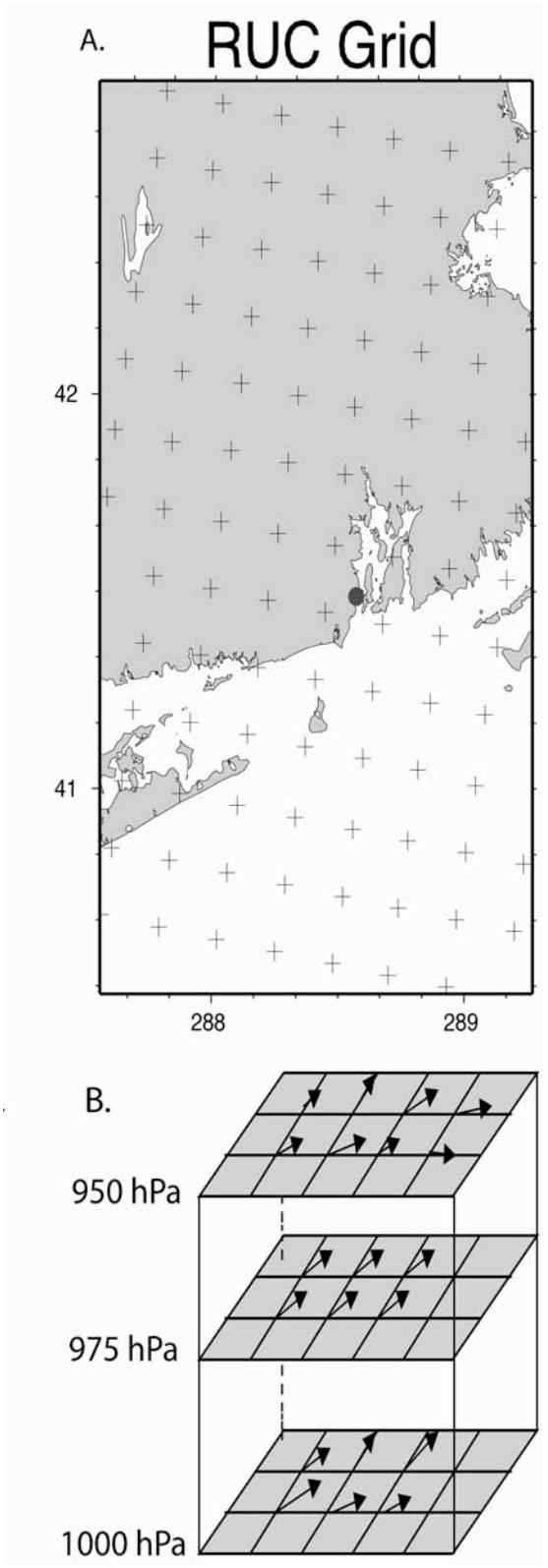

Figure 2. A) Part of the Lambert-conformal conical grid that the RUC model uses to produce wind speed and direction. B) A visualization of the layered wind data used to calculate the balloon trajectory using the assumptions that the winds vary with pressure and position.

interpolating in needed and the wind at that spot is used. The balloon landing directly on a grid line is the second case. With this case, then the weighted average only needs to be done between two grid points instead of all four grid points which is what needs to be done in case three. Since the grid shape is a Lambert-conformal, determining the surrounding grid points is more complicated then if the grid had a Cartesian shape. To determine the surrounding grid points, the equation of each zonal and each meridional grid line is determined using point-slope format. Determining which lines are just less than and just greater then the balloon's position gives the surrounding points. This is the basis for the second order approximation.

In the calculating of the trajectories any drag force on the balloon was ignored. It is safe to do this because the balloon is so large that is can be assumed to be traveling along at the same speed of the wind as the wind pushes the balloon instead of the wind producing a drag force on the balloon opposing the direction of motion.

Result/Discussion

Ozone Profiles

By having data on temperature and frost point (or relative humidity), it is possible to distinguish pollution ozone from stratospheric ozone. Since the air in the stratosphere is normally dry air, large peaks in ozone accompanied by large drops in the frost point lead to the conclusion that the ozone at that spot is from the stratosphere. The following figure shows the ozone profile taken on July 9th, 2004. The large peak in ozone at approximately 7 km is primarily stratospheric ozone because of the accompanying large drop in frost point. There is also a smaller ozone peak at 5 km, also stratospheric ozone because of the corresponding slight drop in frost point.

Typical surface ozone levels are around 40 – 70 ppbv in the summer when pollution is low. Figure 3 is a good example of normal surface ozone while Figure 4 is a good example of some surface pollution. The two examples presented here show stratospheric ozone higher in the troposphere while pollution ozone is near the surface. While it is more common to see pollution ozone near the surface and stratospheric ozone at higher altitudes, it is still possible for pollution ozone to be present higher up in the troposphere. However, the higher up in the troposphere the pollution ozone rises, it mixes with more and more natural ozone and the pollution ozone becomes harder to identify. Stratospheric ozone is generally only seen higher up in the troposphere. At sea level, stratospheric ozone hardly ever is present at the surface. However if the balloon was released from a location above sea level, it would be possible to observe stratospheric ozone at the surface.

The profile taken on Aug. 2nd is shown in Figure 4. The ozone is Figure 4 varies more with height then the ozone in Figure 3 does. In the Aug 2nd profile, stratospheric ozone can be seen at 9 km. There is also a slight peak in ozone at 1 km. However, it is not accompanied by a dip in the frost point. A high ozone

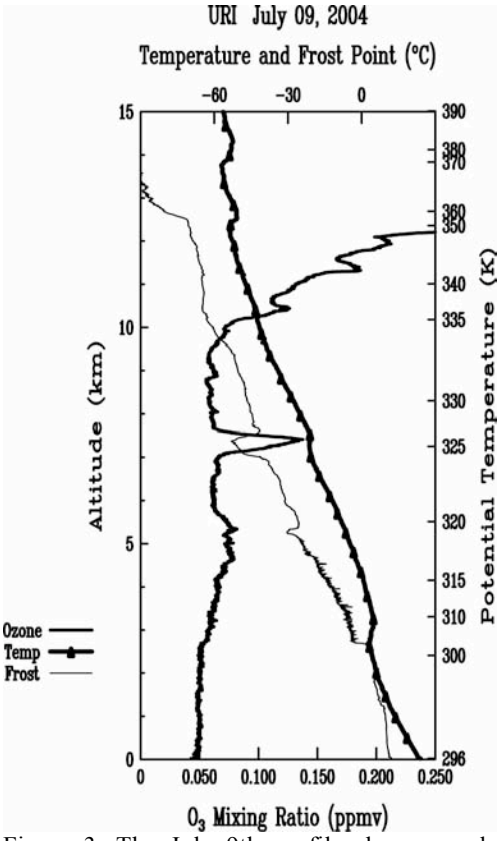

Figure 3. The July 9th profile shows regular ozone levels at the surface and stratospheric ozone at 7 km. The ozone-mixing ratio is denoted by the plain dark line and is measured in ppmv on the bottom axis, while the dark line with the triangles indicates the temperature and the lighter line is for the frost point, both measured on the top axis in oC. The altitude is given in km on the left axis.

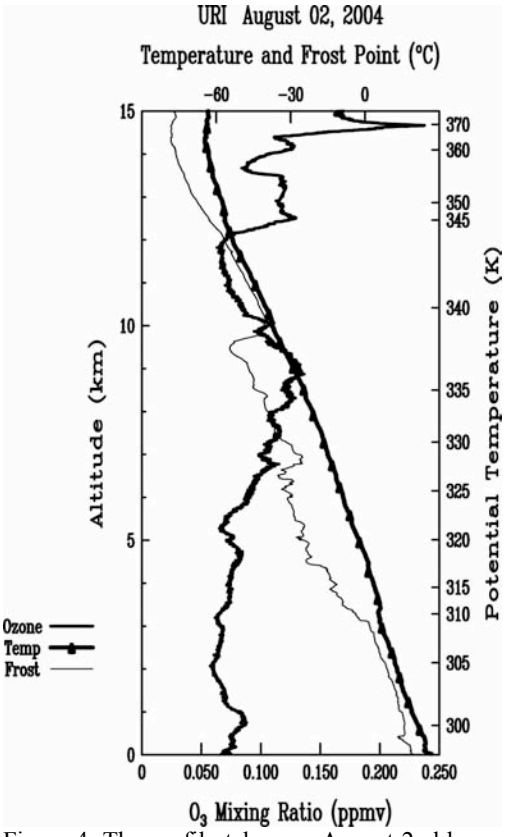

Figure 4. The profile taken on August 2nd has pollution ozone at the surface and stratospheric ozone at 9 km.

level with no dip in frost point indicates that the elevated ozone is due to pollution instead of stratospheric ozone.

Trajectories

The first approximation of the trajectory worked reasonably well considering how crude an approximation it was. For the first approximation, the wind was assumed constant at each isobaric level, making the wind a function of pressure only. As can be seen in Figure 5 the calculated trajectory agrees with the known trajectory for the first 10 km. After that however, the calculated trajectory starts to deviate significantly from the known trajectory. The reason this first approximation is so accurate in the beginning has to do with how the wind changes with position. When the change in position is small, the change in wind is negligible. However, with larger changes in distance, the wind will most likely be very different. This would lead to the breakdown of the simplifying assumption. Another reason the first approximation is more accurate in the beginning is because the wind data used is from right when the balloon was let go. By the end of the trajectory, the wind has most likely changed just cause the wind varies in time.

The second approximation of the trajectory did not work as well as expected. For the second approximation, the wind was treated as a function of pressure and position. This more closely represents what the balloon is experiencing then the first approximation. However, as Figure 6 shows, it produces a less accurate trajectory. This is puzzling and I believe that the reason the second approximation is less accurate then the first approximation comes with the fact that the second approximation was coded at the very end of the program and there was not time to find and correct all of the kinks in it.

Future Work

The second approximation of the trajectory is not working as hoped. In future work on the project, the errors in the second approximation would be found and fixed. Then, with the second approximation working, a third time-dependent approximation would be done. It takes the balloon about an hour to reach 100 hPa. By the time the balloon reaches the top of its trajectory, the winds will have changed. Using data from the launch time and from an hour later, the winds can be interpolated in time as well as in pressure and position.

With even more time, the trajectories would be calculated by using a midpoint approach. Currently, the winds are calculated at each level. To make the

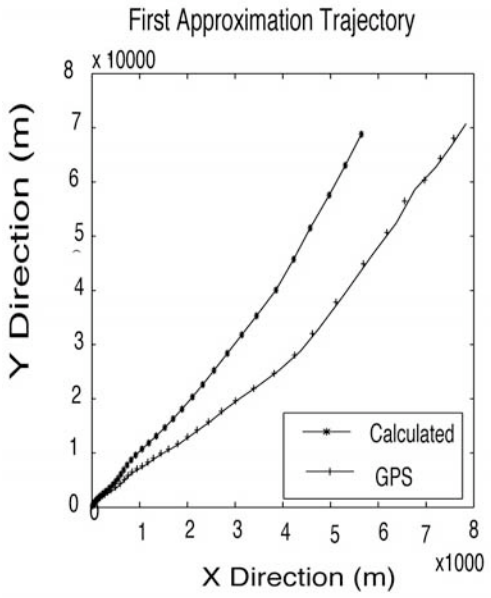

Figure 5. Trajectory of the balloon RI037 with winds from a single spot plotted along side the known trajectory of the balloon from GPS position data.

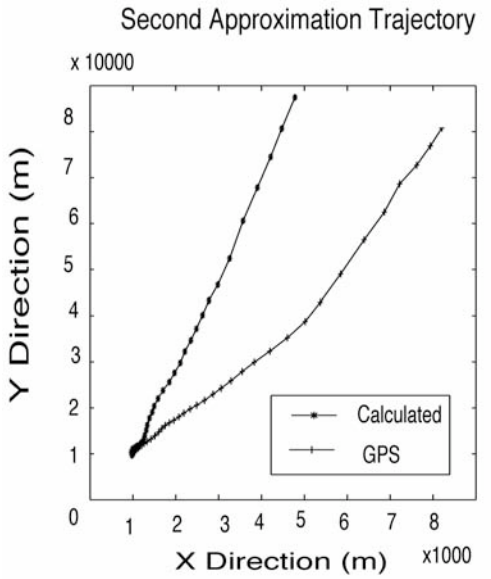

Figure 6. Trajectory of the balloon RI037 with winds varying with position as well as with pressure.

approximations even more accurate, the winds would be calculated first at the next level. Then using the winds for the second and first level, the wind for the midpoint between the levels can be calculated. Then using the winds from the midlevel, a more accurate position in the second level can be calculated and the winds from that spot can be interpolated. This should lead to an even better approximation for the trajectory.

Conclusion

There were only a few cases observed this summer where the surface ozone count was high. Even though there was low ozone at the surface, there were numerous accounts of elevated ozone in the middle and upper troposphere. To determine if this is unusual for Rhode Island, more data will need to be collected. However, it does appear to be unusual compared to other stations such as the one at Wallops Island, VA.

Acknowledgments. I would like to thank John Merrill for advising me on this project, Jay Dubious for working alongside me in the releasing of the balloons, all the other SURFOs for supporting me this summer, Rob Pockalny and Rich Viso for leading the SUFRO program and NSF for funding it.

References

Benjamin, Stanleu G.; Brundage, Kevin J.; Miller, Patricia A.; Smith, Tracy Lorraine; Grell, George A.; Dongsoo, Kim; Brown, John M.; and Schlatter, Thomas W.; The Rapid Updata Cycle at NMC. Tenth Conference on Numerical Weather Prediction, American Meteorology Society, July 1994, pp. 566-568.

Bleck, R., and S. G. Benjamin, 1993: Regional weather prediction with a model combining terrain-following and isentropic coordinates. Part 1: model description. Mon. Wea. Rev., 121, 1770-1785.

Hobbs, Peter V.Introduction to Atmospheric Chemistry. Cambridge University Press.New York, NY. 2000.

Homhyr, W. D., R. A. Barnes, G. B. Bruthers, J. A. Lathrop, and D. P. Oppeman: Electrochemical concentration cell ozonesonde performance during STOIC 1989, J. Geophysics Rev., 100, 9231-9244, 1995.

Holton, James R. An Introduction to Dynamic Meteorology. Elsever Academic Press. San Diego, CA. 2004.

M. Stevens and J. T. Merrill, Graduate School of Oceanography, University of Rhode Island, Narragansett, RI 02882. (mstevens@school.edu, jmerrill@gso.uri.edu)

Copyright 2004 by the Graduate School of Oceanography/University of Rhode Island, SURFO program